



UNIVERSITÀ DI PISA
DIPARTIMENTO DI INGEGNERIA DELL'INFORMAZIONE:
ELETTRONICA, INFORMATICA E TELECOMUNICAZIONI

TESI DI DOTTORATO

DESIGN AND FABRICATION OF MEMS ELECTROSTATIC ACTUATORS

Corso di Dottorato In Ingegneria dell'Informazione
XIX ciclo
Curriculum: Tecnologie, dispositivi e sistemi micro e nanoelettronici

Allievo:

Ing. Antonio Molfese

Tutori:

Prof. Andrea Nannini

Ing. Francesco Pieri

Abstract

Design and Fabrication of MEMS Electrostatic Actuators

by Antonio Mofese

The research presented in this thesis is focused on the design and development of MEMS (Micro Electro Mechanical System) electrostatic actuators. Different kinds of electrostatic actuators are analyzed and presented.

The study of torsional electrostatic actuator is carried out and the design of an micromirrors array for beam steering optical switching in a thick polysilicon technology is presented. The main advantage of these devices is that they are realized in a commercial surface micromachining technology (THELMA by *STMicroelectronics*) hence they are less expensive than other solutions present in literature.

For the torsional actuators, a novel semi-analytical model which allows prediction of the behaviour of the structures and takes into account the flexural deformation of the structure is presented. A very good agreement between the model, FEM simulation and experimental results has been obtained.

The possibility of using another competitive surface micromachining technology (developed at IMEC) which uses poly silicon germanium as structural layer to realize the micromirrors is also investigated. Poly Silicon Germanium has the advantage that can be integrated on top of commercial CMOS. The development of optimized (low stressed) layers of poly silicon germanium has been addressed and some test micromirrors using this technology have been designed.

Moreover an analysis of the levitation effect in electrostatic comb fingers actuators is presented. The use of this actuation for vertical or torsional motion of micromachined structures is exploited. Two different levitational mechanical resonators have been designed and fabricated in *THELMA*. Because of the high thickness of the structural layer, classic springs shows several limitation, so specifically designed suspension springs (rotated serpentines), with better performance for high thickness, have been used. A full analysis of this kind of spring and a comparison with other springs are also presented. Finally a study of the dependence of the levitation force intensity on

the geometric parameters of the actuators is performed using FEM simulations, and information about critical geometrical parameters in the design of operative levitational actuators is obtained. The devices are characterized and the obtained results are compared with FEM simulations.

Acknowledgements

First, I would like to thank my research advisors, Prof. Andrea Nannini and Ing. Francesco Pieri for drawing me into the world of MEMS. I would like to thank them for their energetic guidance, encouragement and support throughout the course of my research.

Thanks to Dr. Ann Witvrouw who allowed me to spend six months in the competitive and stimulating environment of IMEC (Interuniversity Microelectronic Center).

Thanks to *STMicroelectronics* for the fabrication of the presented devices and to CNR, Italian National Research Council for funding. A special thanks to the staff of the “Laboratorio di Tecnologie Elettroniche e Microsistemi” at the Department of Information Engineering at University of Pisa for their help. Several people have contributed to the research presented in this thesis: thanks to the staff of the Optoelectronics Group at University of Pavia for the optical measurements, Virginia Greco for collaborating with me on the micromirrors, Alessandro Campinoti for collaborating on Electrostatic Levitational Actuators, Anshu Mehta and Bert Du Bois for their help on Poly SiGe research and all the students who worked with me.

For sharing the everyday fun of graduate life, thanks to Dario Paci, Niccolò Nizza, Lucanos Strambini, Fabrizio D’angelo and Pierluigi Nuzzo. A special thanks to them for the much needed coffee breaks.

My acknowledgements would not be complete without thanking my mother, my sisters and my friends for their support through the years. Moreover this thesis is also dedicated to the memory of my grandmother and my father.

Finally, a most special thank you to my girlfriend, Gabriella, for her unfailing support through the ups and downs of my graduate career. I am especially grateful for her enthusiasm that continues to make this the most enjoyable of times.

Table of Contents

1 Introduction	1
2 MEMS Devices and Electrostatic Actuators.....	3
2.1 Introduction	3
2.2 MEMS	4
2.3 Microfabrications for MEMS.....	6
2.3.1 Bulk micromachining of silicon.....	7
2.3.2 Surface micromachining of silicon	9
2.3.3 Wafer bonding for MEMS	11
2.3.4 LIGA process	12
2.3.5 Three-dimensional microfabrications	13
2.4 Electromechanical Transducers.....	13
2.4.1 Electrostatic actuators	16
2.4.1.1 Parallel plate actuators	17
2.4.1.2 Electrostatic comb drive.....	20
2.4.2 Piezoelectric transducers	22
2.4.3 Electromagnetic transducers	24
2.4.4 Electrothermal actuators.....	27
2.4.5 Other Transducers	28
2.4.6 Comparison of electromechanical actuation schemes	29
2.5 Microsensing for MEMS.....	30
2.5.1 Capacitive sensing.....	30
2.5.2 Piezoresistive sensing.....	31
2.5.3 Piezoelectric sensing	32
2.5.4 Other sensing systems	32
2.6 Applications of MEMS electrostatic actuators: Micromirrors	33
2.6.1 Digital Light Processing.....	33
2.6.2 Maskless Lithography	35
2.6.3 Optical Switching.....	36
2.6.4 Examples of micromirrors for Optical Switching	40
2.6.4.1 Surface-Micromachined Mirrors.....	40
2.6.4.2 Bulk Micromachined mirrors	41
2.6.4.3 Drawbacks	43

3 Surface Micromachining: Polysilicon and Polysilicon germanium	44
3.1 Thick PolySilicon Technology	44
3.1.1 THELMA by STMicroelectronics	44
3.2 Poly Silicon Germanium as structural material.....	46
3.3 Determination of stress profile and optimization of stress gradient in PECVD poly-SiGe films	48
3.3.1 Measurements principles and fitting model	48
3.3.1.1 Yang's method	49
3.3.1.2 Van Der Donck's method.....	51
3.3.1.3 Furtch's method	52
3.3.1.4 Proposed method	53
3.3.2 Experimental details.....	55
3.3.3 Results and discussion.....	56
 4 Micromirrors for Optical Switching: Models and Fabrications	63
4.1 Torsional electrostatic actuators.....	65
4.2 Pull-in Voltage	66
4.3 Torsional Elastic constants of the hinges	68
4.4 Dynamic characterization: small-signal equivalent circuit	72
4.5 Design Flow of the micromirrors arrays	76
4.5.1 Firt test pattern: Not movable micromirrors	77
4.5.2 Final test Pattern: description of the designed array ..	77
4.6 Modal Analysis by FEM simulations.....	81
4.7 Reduced-Order Modelling of the bending of an array of torsional micromirrors.....	82
4.7.1 Computational approach	82
4.7.2 Results and Discussion.....	84
4.8 Design of an driving circuit for micromirrors.....	87
4.9 Experimental Results.....	89
4.9.1 Preliminary Static measurements	89
4.9.2 Resonant mode measurements	90
4.10 Test structures on Poly Silicon Germanium technology by IMEC	92
4.10.1 Structures A.....	93
4.10.2 Structures B	98
4.10.3 Structures C	101

5 MEMS Flexure Design.....	102
5.1 Introduction	102
5.2 Modeling and method of analysis	105
5.3 Analytical expressions for the spring constants	107
5.4 FEM simulations	112
5.3.1 Description	112
5.5 Results	112
5.6 Conclusions	116
5.A: Unit-load method.....	116
5.B: Calculation of the spring constants.....	117
5.B.1. Torsional spring constant $K_{\theta x}$	117
5.B.2. Spring constant K_x	118
5.B.3. Spring constant $K_{\delta y}$ for the classic serpentine springs with guided end	119
5.B.4. Spring constant $K_{\delta x}^C$ for the classic serpentine spring ..	120
5.B.5. Spring constant $K_{\delta y}$ for the rotated serpentine spring	121
5.B.6. Spring constant $K_{\delta x}$ for the rotated serpentine spring	123
6 Electrostatic Levitational Actuators.....	125
6.1 Introduction	125
6.2 Fabricated Devices	126
6.3 Theoretical Analysis.....	126
6.4 Measurements methods	130
6.4.1 The problem of the parasitic capacitance	130
6.4.1.1 EAM modulation.....	133
6.4.2 The second harmonic method	136
6.5 Measurements.....	139
6.6 FEM simulations	142
7 Conclusions	145
Bibliography	147

Chapter 1

Introduction

In the last two decades, great strides in the development of high precision lithography and microfabrication techniques for the manufacture of high speed and low noise electronic circuitry have created a new branch of research that uses these fabrication tools to manufacture a new class of micro-scale devices. This area of research, MicroElectroMechanical systems (MEMS), creates mechanical devices that are controlled by various actuation mechanisms including electrostatic, magnetic and acoustic, for use in a variety of applications. MEMS devices offer the advantage of compactness, lithographic precision, high speed, low power consumption and ready integration with standard circuitry.

There are numerous MEMS devices that have been successfully used in diverse areas of engineering and science. Inkjet printer heads, micropumps, projection display arrays, and airbag accelerometers are just a few examples, where MEMS devices have replaced more conventional devices in their class for fractions of the cost.

Electrostatic actuation, which is impractical at normal size scales because of the large voltages involved, became competitive with other actuation methods at the MEMS scale. For this reason, electrostatic actuators are one of the most important subjects in MEMS research, and also the main focus of this thesis.

In **Chapter 2** an overview of the state of art of all kinds of MEMS technologies is presented and the difference between surface and bulk micromachining is addressed. Then comparison between the different MEMS actuators is presented and, after the explanation of the advantages of electrostatic actuators, some examples of one of the most interesting applications are listed: the micromirrors.

The micromirrors are the most widely used optical element with the ability to mechanically steer incident optical beams over a large range of deflection angles relatively fast. Typical applications include beam steering of optical signals within an optical cross-connect (OXC) switch in telecommunication network and scanning optical beams for

high resolution micro displays. The small size of these micromirrors makes them suitable as individual elements in large scale mirror array assemblies for the manipulation of incident optical beams to create a desired far-field pattern. Unfortunately most of the presented micromirrors are not cost effective for the complicated process flow used to realize them.

In **Chapter 3** two single thick structural layer technologies are presented. The former is polysilicon based (THELMA by *STMicroelectronics*) and is a commercial process used mainly for inertial sensors. The latter is Poly Silicon Germanium based (by IMEC) and has the advantage that can be integrated on top of commercial CMOS. Both are surface micromachining, allow the realization of several MEMS structures and are used in this thesis.

In **Chapter 4** the design, fabrication and measurements of MEMS micromirrors for optical switching is presented. Innovative models which allows prototyping and prediction of the behaviour of the micromirrors and, in general, of the torsional actuators are described.

The micromirrors are realized in THELMA technology so they have the great advantage of being cost effective as this process is already industrialized for other applications. Moreover the design of micromirrors in Poly Silicon Germanium is also presented, as the possibility of the integration directly on top of standard CMOS is a further improvements.

In **Chapter 5** an interesting analysis of MEMS flexure design is presented. Elastic components are another important elements of MEMS so an effort is made to derive analytic models: expressions are given for spring constants of two kinds of serpentine geometries. One of the geometries is also an innovation in MEMS design.

In **Chapter 6** an in-depth study and models of the electrostatic levitation effect in comb finger actuators is presented. Moreover the possibility of using this parasitic phenomenon as actuation is exploited and resonators using it are presented.

In the final chapter, we form conclusions about the designed and fabricated devices and the presented models. We then outline a path for future research in modelling, simulations and realization of surface micromachined electrostatic actuators.

Chapter 2

MEMS Devices and Electrostatic Actuators

2.1 Introduction

Microelectromechanical systems (MEMS) are small integrated devices or systems that combine electrical and mechanical components. They range in size from the sub micrometer (or sub micron) level to the millimeter level, and there can be any number, from a few to millions, in a particular system. MEMS extend the fabrication techniques developed for the integrated circuit industry to add mechanical elements such as beams, gears, diaphragms, and springs to integrated systems

MEMS are a new frontier in miniaturization. MEMS researchers have taken technology traditionally restricted to the manufacture of electronic integrated circuits and developed methods to make machines on a chip. Not only is MEMS technology able to produce devices that operate on the scale of 100 micron diameter gears and micron-thick hinges, but the machines can be interfaced with electronic drives, control mechanism and other MEMS on the same chip. This implementation gives a new meaning to the phrase “integrated circuit”.

The electronics and mechanical aspects of MEMS are well known, being part of the acronym. However, MEMS can also include magnetic, thermal, fluidic and electromagnetic mechanism. The general terms *Microsystems* can be used, but we will continue to employ MEMS for its brevity and because of widespread acceptance. In keeping with common usage, we take the term MEMS to include micromachined structures, even if they do not have moving parts.

Examples of MEMS device applications include inkjet-printer cartridges, accelerometers, miniature robots, microengines, locks, inertial sensors, microtransmissions, micromirrors, micro actuators, optical scanners, fluid pumps, transducers, and chemical, pressure and

flow sensors. New applications are emerging as the existing technology is applied to the miniaturization and integration of conventional devices.

These systems can sense, control, and activate mechanical processes on the micro scale, and function individually or in arrays to generate effects on the macro scale. The micro fabrication technology enables fabrication of large arrays of devices, which individually perform simple tasks, but in combination can accomplish complicated functions.

MEMS are not about any one application or device, nor are they defined by a single fabrication process or limited to a few materials. They are a fabrication approach that conveys the advantages of miniaturization, multiple components, and microelectronics to the design and construction of integrated electromechanical systems. MEMS are not only about miniaturization of mechanical systems; they are also a new paradigm for designing mechanical devices and systems

During the past decade, several new fabrication techniques have evolved which helped popularize microelectromechanical systems (MEMS), and numerous novel devices have been reported in diverse areas of engineering and science.

MEMS can be divided into two classes: MEMS actuators and MEMS sensors. The first one is a kind of moving mechanism activated by an electrical signal like micromotor. Micro sensors are currently available for a large number of applications. Historically, owing to their ease of fabrication, these were the earliest microsystems. Another reason for the actuators not becoming popular is that the amount of energy generated by such tiny systems does not cause much impact in the associated systems. The electromotive force used to move the structures on the wafer surface is typically electrostatic attraction, although magnetic, thermal or even gas-based microactuator structures have been developed.

2.2 MEMS

The term MEMS refers to a collection of microsensors and actuators which can sense its environment and have the ability to react to changes in that environment with the use of a microcircuit control. They include, in addition to the conventional microelectronics packaging, structures for command signals into micro electromechanical structures for desired sensing and actuating

functions. The system also may need micropower supply, micro relay and microsignal processing units. Microcomponents make the system faster, more reliable, cheaper and capable of incorporating more complex functions.

In the beginning of the 1990s, MEMS emerged with the aid of the development of integrated circuit (IC) fabrication processes, where sensors, actuators and control functions are co-fabricated in silicon. Since then, remarkable research progresses have been achieved in MEMS under strong capital promotions from both government and industry. In addition to the commercialization of some less-integrated MEMS devices, such as microaccelerometers, inkjet printer heads, micro mirrors for projection, etc., the concepts and feasibility of more complex MEMS devices have been proposed and demonstrated for the applications in such varied fields as microfluidics, aerospace, biomedicine, chemical analysis, wireless communications, data storage, display, optics, etc.[1-2].

Some branches of MEMS, such as micro-opto-electromechanical systems (MOEMS), micro total analysis systems (μ TAS), etc., have attracted a great deal of research interest since their potential application market. As of the end of the 1990s, most MEMS devices with various sensing or actuating mechanisms were fabricated using silicon bulk micromachining, surface micromachining and LIGA¹ processes [3-5]. Three dimensional microfabrication processes incorporating more materials were presented for MEMS recently when some specific application requirements (e.g. biomedical devices) and microactuators with higher output power were called for in MEMS [1,5-11].

Micromachining has become the fundamental technology for the fabrication of microelectromechanical devices and, in particular, miniaturized sensors and actuators. Silicon micromachining is the most mature of the micromachining technologies and it allows for the fabrication of MEMS that have dimensions in the submillimeter range. It refers to fashioning microscopic mechanical parts out of silicon substrate or on a silicon substrate, making the structures three dimensional and bringing new principles to the designers. Employing materials such as crystalline silicon, polycrystalline silicon and silicon

¹ LIGA is a German acronym, for Lithographie, Galvanoformung, Abformung (lithography, galvanofforming, moulding)

nitride, etc., a variety of mechanical microstructures including beams, diaphragms, grooves, orifices, springs, gears, suspensions and a great diversity of other complex mechanical structures has been conceived [12-16].

The integration of micromachining and microelectronics on one chip results in so-called smart sensors. In smart sensors, small sensor signals are amplified, conditioned and transformed into a standard output format. They may include microcontroller, digital signal processor, application-specific integrated circuit (ASIC), self-test, self-calibration and bus interface circuits, simplifying their use and making them more accurate and reliable.

Microsensors and actuators are fabricated using the well-known micromachining techniques in the microelectronics industry. Silicon micromachining has been a key factor for the vast progress of MEMS in the past decade. This refers to the fashioning of microscopic mechanical parts out of silicon substrates and more recently other materials. It is used to fabricate such features as clamped beams, membranes, cantilevers, grooves, orifices, springs, gears, suspensions, etc. These can be assembled to create a variety of sensors. Bulk micromachining is the commonly used method but it is being replaced by surface micromachining which offers the attractive possibility of integrating the machined device with microelectronics which can be patterned and assembled on the same wafer. Thus power supply circuitry, signal processing using ASICs can be incorporated. It is the efficiency of creating several such complete packages using existing technology that makes this an attractive approach.

2.3 Microfabrications for MEMS

Silicon micromachining has been a key factor for the vast progress of MEMS. Silicon micromachining refers to fashioning microscopic mechanical parts out of a silicon substrate or on a silicon substrate. Silicon micromachining comprises of two technologies: bulk micromachining, in which structures are etched into silicon substrate, and surface micromachining, in which the micromechanical layers are formed from layers and films deposited on the surface. Bulk micromachining and surface micromachining are the two major micromachining processes of silicon; silicon wafer bonding is usually necessary for silicon microfabrication. LIGA and three-dimensional

(3D) microfabrications have been used for high-aspect ratio and 3D microstructures fabrication for MEMS.

2.3.1 Bulk micromachining of silicon

Bulk micromachining is the most mature of the two silicon micromachining technologies. It emerged in the early 1960s and has been used since then in the fabrication of different microstructures. It is utilized in the manufacturing of the majority of commercial devices – almost all pressure sensors and silicon valves and 90% of silicon accelerometers.

The term *bulk micromachining* comes from the fact that this type of micromachining is used to realize micromechanical structures within the bulk of a single-crystal silicon wafer by selectively removing ('etching') wafer material. The microstructures fabricated using bulk micromachining may cover the thickness range from submicron to full wafer thickness (200 to 500 μm) and the lateral size range from submicron to the lateral dimensions of a full wafer.

Bulk micromachining of Si uses *wet-* and *dry-etching* techniques in conjunction with etch masks and etch stops to sculpt micromechanical devices from the Si substrate.

For etching such thick silicon substrate, anisotropic *wet* etchants such as solutions of potassium hydroxide (KOH), ethylenediamine pyrocatechol (EDP), tetramethylammonium hydroxide (TMAH) and hydrazine-water are used. These etchants have different etch rates in different crystal orientations of the silicon [15,17]. Wet etching in most case is done from the back side of the wafer while the plasma-etching is being applied to the front side.

In recent years, a vertical-walled bulk micromachining technique known as SCREAM (single-crystal reactive etching and metallization), which is a combination of anisotropic and isotropic plasma etching, is used [18]. The etch process can be made selective by the use of dopants (heavily doped regions etch slowly), or may even be halted electrochemically (e.g. etching stops upon encountering a region of different polarity in a biased p–n junction). A region at which wet etching tends to slow down or diminish is called an '*etch-stop*'. There are several ways in which an etch-stop region can be created; doping-selective etching (DSE) and bias-dependent DSE [15,17-18]

Wet etching can either be isotropic etching or anisotropic etching depending on the structure of the materials or the etchants

used. If the material is amorphous or polycrystalline, wet etching is always isotropic etching. During isotropic etching, resist is always undercut, meaning the deep etching is not practical for MEMS. Single-crystal silicon can be anisotropically etched. The etching features are determined by the etching speed, which is dependent on the crystal's orientation. The etching slows down significantly at the (111) planes of silicon, relative to other planes. With the chosen wafers with different crystal orientation, different bulk machined features can be achieved. By combining anisotropic etching with boron implantation (P+ etch-stop), and electrochemical etch-stop technique, varied silicon microstructures can be bulk machined (Figure 2.1).

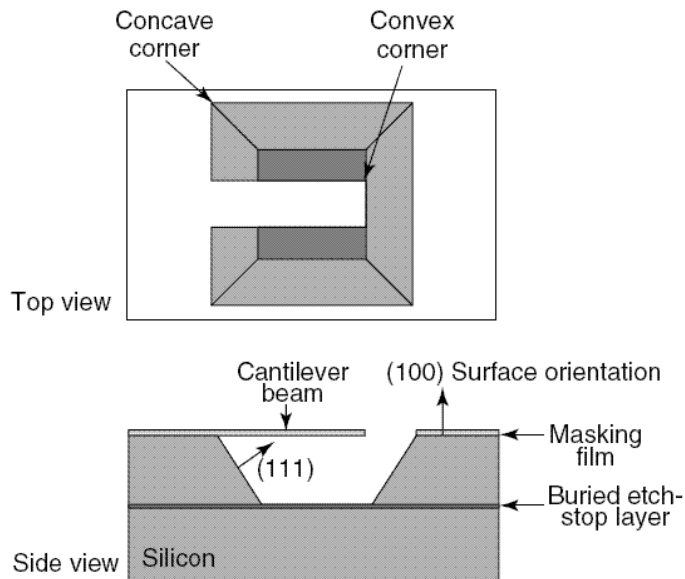


Figure 2.1: Catilever realized by anisotropic etching with buried etch-stop layer

Dry etching occurs through chemical or physical interaction between the ions in the gas and the atoms of the substrate. The most common dry etching of bulk silicon are plasma etching and reactive ion etching (RIE) etching, where the external energy in the form of RF power drives chemical reactions in low-pressure reaction chambers. A wide variety of chlorofluorocarbon gases, sulfur hexafluoride, bromine compounds and oxygen are commonly used as reactants. The anisotropic dry etching processes are widely used in MEMS because of the geometry flexibility and less chemical contamination than in wet etching sometimes. Arbitrarily oriented features can be etched

deep into silicon using anisotropic dry etching. Very deep silicon microstructures can be obtained by the deep RIE (DRIE) dry etching[12].

With bulk-micromachined silicon microstructures, the wafer-bonding technique is necessary for the assembled MEMS devices.

2.3.2 Surface micromachining of silicon

Surface micromachining enables the fabrication of complex multicomponent integrated micromechanical structures that would not be possible with traditional bulk micromachining. This technique encases specific structural parts of a device in layers of a sacrificial material during the fabrication process. The substrate wafer is used primarily as a mechanical support on which multiple alternating layers of structural and sacrificial material are deposited and patterned to realize micromechanical structures. The sacrificial material is then dissolved in a chemical etchant that does not attack the structural parts. The most widely used surface micromachining technique, polysilicon surface micromachining, uses SiO_2 as the sacrificial material and polysilicon as the structural material(Figure 2.2)

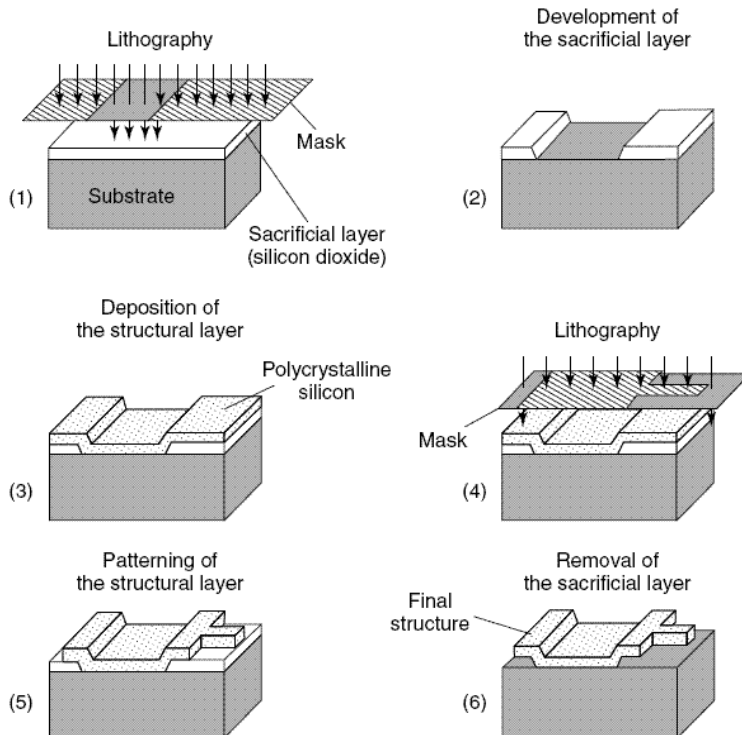


Figure 2.2 Processing steps of typical surface micromachining[21].

The dimensions of these surface micromachined structures can be several orders of magnitude smaller than bulk-micromachined structures. The prime advantage of surface-micromachined structures is their possibility to be integrated with IC components. It should be noted that as miniaturization is immensely increased by surface micromachining, the small mass structure involved may be insufficient for a number of mechanical sensing and actuation applications.

Surface micromachining requires a compatible set of structural materials, sacrificial materials and chemical etchants. The structural materials must possess the physical and chemical properties that are suitable for the desired application. In addition, they must have satisfactory mechanical properties; e.g. high yield and fracture stresses, minimal creep and fatigue and good wear resistance. The sacrificial materials must have good mechanical properties to avoid device failure during fabrication. These properties include good adhesion and low residual stresses in order to eliminate device failure by delamination and/or cracking. The etchants to remove the sacrificial materials must have excellent etch selectivity and they must be able to etch off the sacrificial materials without affecting the structural ones. In addition the etchants must have proper viscosity and surface tension characteristics.

The common IC compatible materials used in surface micromachining are [19]:

- (1) polysilicon/Silicon dioxide; low-pressure chemical vapor deposition (LPCVD) deposited polysilicon as the structural material and LPCVD deposited oxide as the sacrificial material. The oxide is readily dissolved in HF solution without the polysilicon being affected. Together with this material system, silicon nitride is often used for electrical insulation.
- (2) Polyimide/aluminium; in this case polyimide is the structural material and aluminium is the sacrificial material. Acid-based etchants are used to dissolve the aluminium sacrificial layer.
- (3) Silicon nitride/polysilicon; silicon nitride is used as the structural material, whereas polysilicon is the sacrificial material. For this material system, silicon anisotropic etchants such as KOH and EDP are used to dissolve polysilicon.

- (4) Tungsten/silicon dioxide; CVD deposited tungsten is used as the structural material with oxide as the sacrificial material. HF solution is used to remove the sacrificial oxide.

In this work *Poly-SiGe* is also presented as a material suitable as structural layer for MEMS applications. For its low processing temperature enables post-processing MEMS on top of CMOS without introducing significant changes in the existing CMOS foundry processes[20].

Surface micromachining could also be performed using dry etching methods. Plasma etching of the silicon substrate with SF_6/O_2 -based and CF_4/H_2 -based gas mixtures is advantageous since high selectivities for photoresist, silicon dioxide and aluminum masks can be achieved. In contrast, reactive ion etching of poly-Si using a chlorine/fluorine gas combination produces virtually no undercut and almost vertical etch profiles when using photoresist as a masking material. Thus, rectangular silicon patterns which are up to $30\mu\text{m}$ deep can be formed using chlorine/fluorine plasmas out of polysilicon films and the silicon wafer surface.

Silicon microstructures fabricated by surface micromachining are usually planar structures (or are two dimensional). Other techniques involving the use of thin-film structural materials released by the removal of an underlying sacrificial layer have helped to extend conventional surface micromachining into the third dimension. By connecting polysilicon plates to the substrate and to each other with hinges, 3D micromechanical structures can be assembled after release. Another approach to 3D structures used the conformal deposition of polysilicon and sacrificial oxide films to fill deep trenches previously etched in the silicon substrate.

2.3.3 Wafer bonding for MEMS

Silicon micromachining has limitations in forming complex 3D microstructures in a monolithic format; multichip structures are then proposed for advanced MEMS, where wafer-to-wafer bonding is critical in the formation [21]. The wafer bonding for MEMS can be categorized into three major types: anodic bonding, intermediate-layer assisted bonding and direct bonding.

- 1 *Anodic bonding* is also called field-assisted thermal bonding, electrostatic bonding, etc. Anodic bonding is usually established between a sodium glass and silicon for MEMS. For the anodic bonding, a cathode and an anode are attached to the glass (or

silicon with glass thin coating) and silicon wafer, respectively; voltages applied range from 200V to 1000 V. At the same time, the anode is put on a heater providing the bonding temperature around 180 to 500 °C. The advantage of anodic bonding for MEMS is that the low temperature used can ensure the metallization layer (aluminium) could withstand this temperature without degradation.

- 2 *Intermediate-layer assisted bonding.* This type of bonding for MEMS requires an intermediate layer, which can be metal, polymer, solders, glasses, etc., to fulfil the bonding between wafers [21].
- 3 *Direct bonding* is also called silicon fusion bonding, which is used for silicon–silicon bonding. Direct bonding is based on a chemical reaction between OH groups present at the surface of native silicon or grown oxides covering the wafers [19]

2.3.4 LIGA process

MEMS generally require complex microstructures that are thick and three-dimensional[22]. Therefore, many microfabrication technologies have been developed to achieve high-aspect-ratio (height-to-width) and 3D devices. The LIGA process is one of those microfabrications. LIGA is a German acronym for Lithographie, Galvanoformung, Abformung (lithography, galvanofforming, moulding). It was developed by the research Center Karlsruhe in the early 1980s in Germany using X-ray lithography for mask exposure, galvanofforming to form the metallic parts and moulding to produce microparts with plastic, metal, ceramics, or their combinations [1].

With the LIGA process, microstructures height can be up to hundreds of microns to millimeter scale, while the lateral resolution is kept at the submicron scale because of the advanced X-ray lithography. Various materials can be incorporated into the LIGA process, allowing electric, magnetic, piezoelectric, optic and insulating properties in sensors and actuators with a high-aspect ratio, which are not possible to make with the silicon-based processes. Besides, by combining the sacrificial layer technique and LIGA process, advanced MEMS with moveable microstructures can be built [23]. However, the high production cost of LIGA process due to the fact that it is not easy to access X-ray sources limits the application of LIGA. Another disadvantage of the LIGA process relies on that fact that structures fabricated using LIGA are not truly three-dimensional,

because the third dimension is always in a straight feature. As we know, complex thick 3D structures are necessary for some advanced MEMS, which means other 3D microfabrication processes need to be developed for MEMS.

2.3.5 Three-dimensional microfabrications

To fabricate 3D structures for MEMS, many novel 3D microfabrication techniques have been developed. Among them, microscale freeform fabrications are very impressive to achieve 3D MEMS devices. Most of the freeform fabrications build 3D microstructures in an additive layer-by layer fashion[6-9].

Another approach to build 3D MEMS devices is to combine the current micromachining processes, such as silicon micromachining, LIGA, precision mechanical machining, etc., or combining the new 3D microfabrication processes with the silicon micromachining and LIGA processes[24-25]. The AMANDA process is one of these combined microfabrication processes, which combines the LIGA process (or precision machining) with silicon micromachining.

It is known that 3D MEMS devices are usually with multiple layers fabricated from many different structural and functional materials, hence they are expensive and it is difficult their industrialization.

2.4 Electromechanical Transducers

Mechanical filters and their micromechanical counterparts rely on the transformation of electrical energy to a mechanical form and vice versa, through a frequency-dependent transducer, for their operation. In this section basic principles of some of these common electromechanical transducers are discussed briefly. The energy conversion schemes presented here include electrostatic (the focus of the work) piezoelectric, electromagnetic electrothermal and other transducers.

One important step in the design of these mechanical systems is to obtain their electrical equivalent circuit from their analytical model. This often involves first obtaining mechanical equivalent circuits using springs and masses, and then using the electromechanical analogies to reach the electrical equivalent circuits. Such conversions need not always be exact but would serve as an easily understood tool in their design. The use of these electrical equivalent circuits would also facilitate the use of vast resources available for modern

optimization programs for electrical circuits. A list of useful electromechanical analogies is given in Table 2.1[26].

These are known as mobility analogies. These analogies become useful when one needs to replace mechanical components with electrical components which behave similarly, forming the equivalent circuit.

Table 2.1: Electromechanical mobility analogies[26]

	Mechanical Parameter	Electrical Parmeter
Variable	Velocity, angular velocity	Voltage
Lumped network elements	Force, torque	Current
	Damping	Conductance
	Compliance	Inductance
Transmission lines	Mass, mass moment of inertia	Capacitance
	Compliance per unit length	Inductance per unit length
	Mass per unit length	Capacitance per unit length
Immitances	Characteristic mobility	Characteristic impedance
	Mobility	Impedance
	Impedance	Admittance
	Clamped point	Short circuit
	Free point	Open circuit
Source immitances	Force	Current
	Velocity	Voltage

As a simple example, the development of an electrical equivalent circuit of a mechanical transmission line component is discussed here (Johnson, 1983). The variables in such a system are force and velocity. The input and output variables of a section of a lossless transmission line can be conveniently related by

ABCD matrix form as:

$$\begin{bmatrix} \dot{x}_1 \\ F_1 \end{bmatrix} = \begin{bmatrix} \cos \beta x & jZ_0 \sin \beta x \\ \frac{j}{Z_0} \sin \beta x & \cos \beta x \end{bmatrix} \begin{bmatrix} \dot{x}_2 \\ F_2 \end{bmatrix} \quad (2.1)$$

Where

$$Z_0 = \frac{1}{A\sqrt{\rho E}} \sqrt{\frac{C_l}{M_l}} \quad (2.2)$$

$$\beta = \frac{\omega}{v_p} \quad (2.3)$$

$$v_p = \sqrt{\frac{E}{\rho}} = \frac{1}{\sqrt{C_l M_l}} \quad (2.4)$$

In these equations $j = \sqrt{-1}$, \dot{x}_1 and \dot{x}_2 are velocities, F_1 and F_2 forces at two ends of a transmission line, Z_0 , β and v_p are the characteristics impedance, propagation constant and phase velocity of the transmission line, A is the cross-sectional area of the mechanical transmission line, E its Young's modulus, and ρ the density. Quantities C_l and M_l are compliance and mass per unit length of the line, respectively. Now, looking at the electromechanical analogies in Johnson (1983), the expressions for an equivalent electrical circuit can be obtained in the same form as Equation

Table 2.2: Direct analogy of electrical and mechanical domains

Mechanical quantity	Electrical quantity
Force	Voltage
Velocity	Current
Displacement	Charge
Momentum	Magnetic flux
Mass	Inductance
Compliance	Capacitance
Viscous damping	Resistance

$$\begin{bmatrix} V_1 \\ I_1 \end{bmatrix} = \begin{bmatrix} \cos \beta x & jZ_0 \sin \beta x \\ \frac{j}{Z_0} \sin \beta x & \cos \beta x \end{bmatrix} \begin{bmatrix} V_2 \\ I_2 \end{bmatrix} \quad (2.5)$$

In Equation (2.5) V and I are the voltage and current on the transmission line (with subscripts representing its ports). The other

quantities in the matrix are also represented by equivalent electrical parameters as:

$$Z_0 = \sqrt{\frac{\mu}{\varepsilon}} = \sqrt{\frac{L_l}{C_l}} \quad (2.6)$$

$$v_p = \frac{1}{\sqrt{\mu\varepsilon}} = \frac{1}{\sqrt{L_l C_l}} \quad (2.7)$$

In Equations (2.6) and (2.7) L_l and C_l represent the inductance and capacitance per unit length of the line, and ε and μ are the permittivity and permeability of the transmission medium.

Apart from the above mobility analogy a direct analogy is also followed at times to obtain the equivalence between electrical and mechanical circuits. These result from the similarity of integrodifferential equations governing electrical and mechanical components [27]. A brief list of these analogies are presented in Table 2.2.

An understanding of the underlying operational principle is essential in obtaining the equivalent circuit of these transducers. A brief description of the operational principles of some of these common transduction mechanisms used in electromechanical systems is provided below.

2.4.1 Electrostatic actuators

Electrostatic actuation is the most common type of electromechanical energy conversion scheme in micromechanical systems. This is a typical example of an energy-storage transducer. Such transducers store energy when either mechanical or electrical work is done on them. Assuming that the device is lossless, this stored energy is conserved and later converted to the other form of energy. The structure of this type of transducer commonly consists of a capacitor arrangement, where one of the plates is movable by the application of a bias voltage. This produces displacement, a mechanical form of energy.

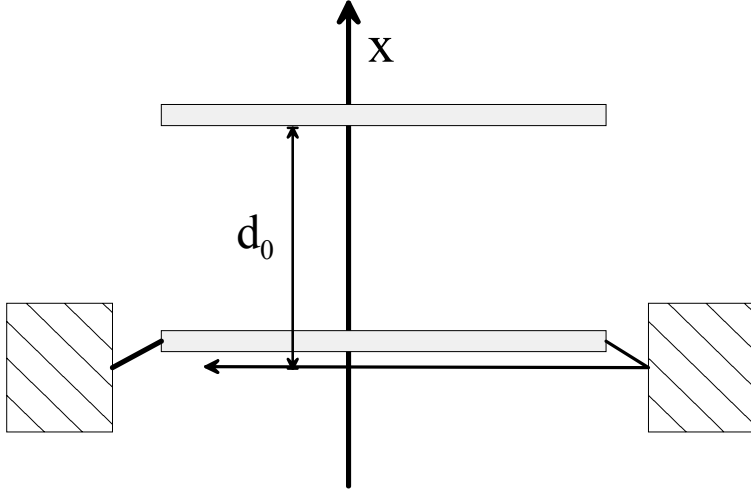


Figure 2.3 Schematic of an electrostatic transducer.

2.4.1.1 Parallel plate actuators

To derive an expression for the electromechanical coupling coefficient, let us first consider a parallel plate capacitor. In Figure 2.3, the bottom plate is fixed, and the top one is movable. The constitutive relations of this structure for voltage (V) and force (F) are given in terms of displacement (x) and charge (Q). These relations can be obtained either analytically from electrostatics, or experimentally when a complicated system with various losses has to be modeled. Assuming that there are no fringing fields, the capacitance of this configuration at rest is widely known to be:

$$C_0 = \frac{\varepsilon A}{d_0} \quad (2.8)$$

However, when a voltage is applied across this system, the top plate moves towards the other, resulting in a net gap

$$d = d_0 - x \quad (2.9)$$

The capacitance with the plates at this new position is

$$C = \frac{\varepsilon A}{d} = \frac{\varepsilon A}{d_0 - x} = \varepsilon A \left[d_0 \left(1 - \frac{x}{d_0} \right) \right]^{-1} = C_0 \left(1 - \frac{x}{d_0} \right)^{-1} \quad (2.10)$$

Since charge is conserved, the instantaneous voltage across these plates is given in terms of the charge (electrical quantity) and displacement (mechanical quantity) as:

$$V(t) = \frac{Q(t)}{C_0} \left[1 - \frac{x(t)}{d_0} \right] = \frac{Q(t)}{C_0} - \frac{Q(t)x(t)}{C_0 d_0} \quad (2.11)$$

Next we endeavour to derive the association between force with charge. The electrostatic force between the plates can be obtained from Coulomb's law. By the principle of conservation of energy, the mechanical work done in moving the plate should balance with an equal variation in electrical energy. Thus the net work done is

$$dW = dW_{\text{electrical}} + F_{\text{Coulomb}} dx \equiv 0 \quad (2.12)$$

Therefore,

$$F_{\text{Coulomb}} = -\frac{\partial W_{\text{electrical}}}{\partial x} \quad (2.13)$$

where

$$W_{\text{electrical}} = \frac{1}{2} CV^2 \quad (2.14)$$

Substituting Equations (2.9)–(2.11) in Equation (2.14), and then back in Equation (2.13), the electrostatic force becomes:

$$F_{\text{Coulomb}} = -\frac{1}{2} \frac{Q^2(t)}{C_0 d_0} \quad (2.15)$$

The nonlinearities in these electromechanical coupling equations, Equations (2.11) and (2.15), are quite apparent. Such nonlinearities are significant in the realization of microswitches. However, for applications in tunable capacitors, filters and resonators this may not be a desirable feature. However, for small variations about the rest position, these relationships can be assumed to be linear, as shown in the following simplification. Equation (2.11) for the voltage across the plates can be expressed in terms of a static charge Q_0 , and a dynamic component as:

$$V(t) = \frac{Q_0}{C_0} + \frac{Q_d}{C_0} - \frac{Q_0}{C_0 d_0} x - \frac{Q_d}{C_0 d_0} x \quad (2.16)$$

$$Q(t) = Q_0 + Q_d \quad (2.17)$$

Considering only the dynamic component of voltage, and using the assumptions $Q_d \ll Q_0$ and $x \ll d_0$, we get:

$$V_d(t) \approx \frac{Q_d}{C_0} - \frac{V_0}{d_0} x \quad (2.18)$$

This electromechanical relation is obviously linear. A similar procedure would lead to the linearization of the other electromechanical coupling equation between the force and charge as:

$$(F_{Coulomb})_d = \frac{V_0}{d_0} Q_d \quad (2.19)$$

It may, however, be reiterated that these linearized expressions are valid for a very small range of displacements around the rest position. The electrostatic coupling equations in the sinusoidal state are written in the form (Rossi, 1988):

$$\tilde{V}_{ca} = \frac{\tilde{I}}{j\omega C_0} - \frac{V_0}{j\omega d_0} \tilde{v} \quad (2.20)$$

$$\tilde{F}_{ca} = \frac{V_0}{j\omega d_0} \tilde{I} \quad (2.21)$$

The coefficient on the right-hand side of Equation (2.21) is the electrostatic coupling coefficient. This being pure imaginary number the energy conversion is purely reactive. One of the equivalent circuits used to represent an electrostatic actuator is shown in Figure 2.4. The parameters appearing there are:

$$C'_{em} = \frac{C_m}{1 - C_0 C_m \left(\frac{V_0}{d_0} \right)^2} \left(\frac{V_0 C_0}{d_0} \right)^2 \quad (2.22)$$

$$Z'_{em} = Z'_m + \frac{1}{j\omega C''_m} \quad (2.23)$$

where

$$C'_m = \frac{C_m}{1 - C_0 C_m \left(\frac{V_0}{d_0} \right)^2} \quad (2.24)$$

and C_m and Z_m are the compliance of the moving plate and its mechanical impedance, respectively.

Fabrication of micro-sized devices with an electrostatic actuation scheme is relatively easy as it is independent of the properties of material systems. Therefore an electrostatic actuation scheme is the most preferred for microactuators. In addition to the parallel plates scheme described above, comb drives are also popular in these devices.

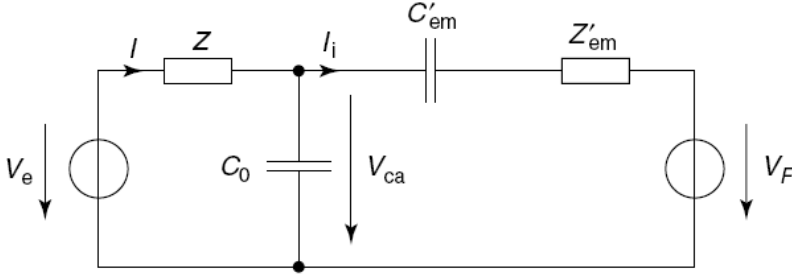


Figure 2.4: Equivalent circuit for electrostatic actuator.

2.4.1.2 Electrostatic comb drive

An electrostatically driven parallel plate actuator has a clamped-clamped beam configuration. Although this is amenable for micro fabrication, as derived previously, this configuration has nonlinear response characteristics. Hence another electrostatically actuated structure is preferred at the microscale. The layout of such a laterally driven electrostatic resonant structure is shown in Figure 2.5. Two resonator configurations are possible with this structure [28]. In the first, a two-port configuration, the structure is driven on one of the comb structures and sensed at the other, for capacitance variations. In the second configuration, both comb structures are used to drive differentially, while sensing is achieved by monitoring shift in impedance at resonance. The folded beam truss suspension has large compliance and is capable of reducing the residual strain in the structural film. In the two-port configuration, the driving force and the sensitivity of the output are both proportional to the variation of capacitance with lateral displacement $\partial C/\partial x$. The static displacement at the drive port, for an applied drive voltage v_D , is [28]:

$$x = \frac{F_x}{k_s} = \frac{1}{2k_s} v_D^2 \frac{\partial C}{\partial x} \quad (2.25)$$

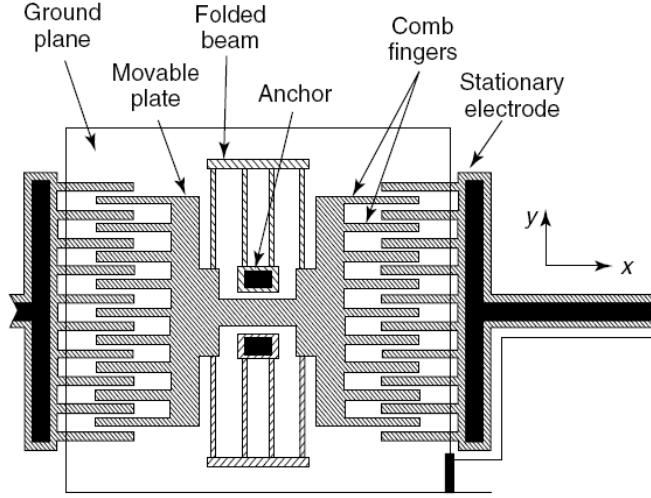


Figure 2.5: Lateral electrostatic comb actuator[28].

where F_x is the x component of the electrostatic force and k_s is the spring constant of the system.

To ensure stability, the drive voltage consists of an ac voltage of amplitude v_d superimposed on a dc bias V_p such that

$$v_D = V_p + v_d \sin \omega t \quad (2.26)$$

It may be mentioned at this point that realization of a small interelectrode gap is essential to reduce the drive voltage requirements of this actuation mechanism.

Substituting Equation (2.25) in Equation (2.26) and taking the time derivative, we get

$$\frac{\partial x}{\partial t} = \frac{1}{2k_s} \frac{\partial C}{\partial x} \frac{\partial v_D^2}{\partial t} = \frac{1}{2k_s} \frac{\partial C}{\partial x} (2V_p v_D \cos \omega t + v_D^2 \sin 2\omega t) \quad (2.27)$$

For ac voltages much smaller than the dc bias, the second harmonic term on the right-hand side can be neglected. At resonance, the magnitude is multiplied by the quality factor, to get the magnitude of the electromechanical transfer function which relates the phasor displacement X to the phasor drive voltage V_d :

$$\left| \frac{X}{V_D} \right| = \frac{V_p \omega Q}{k_s} \frac{\partial C}{\partial x} \quad (2.28)$$

This shows that since $\partial C / \partial x$ is independent of displacement x , the comb drive has a linear electromechanical transfer function between the displacement and the drive voltage. It may, however, be recalled that this analysis assumes that the amplitude of the ac component of the drive voltage is smaller than the dc bias.

The sensed current i_s at the output port is

$$i_s = V_s \frac{\partial C}{\partial x} \frac{\partial x}{\partial t} \quad (2.29)$$

where V_s is the bias voltage between the structure and the sense electrode and Q the quality factor for this structure. Substituting Equation (2.27) in Equation (2.29), the magnitude of the transconductance of the resonant structure is given by:

$$\left| \frac{I_s}{V_D} \right| = \frac{V_p V_s \omega Q}{k_s} \left(\frac{\partial C}{\partial x} \right)^2 \quad (2.30)$$

The parasitic capacitive coupling between the input and output ports is minimized

by including a grounded planar electrode, which also helps suppress excitation of undesired modes. Unfortunately this ground plane produces also a parasitic effect which will be widely analyzed on Chapter 6.

2.4.2 Piezoelectric transducers

When subjected to mechanical stress, certain anisotropic crystalline materials generate charge. This phenomenon, discovered in 1880 by Jaques and Pierre Curie, is known as piezoelectricity. This effect is widely used in ultrasonic transducers. Lead zirconate titanates (PZTs) are the most common ceramic materials used as piezoelectric transducers. These crystals contain several randomly oriented domains if no electric potential is applied during the fabrication process of the material. This results in little changes in the dipole moment of such a material when a mechanical stress is applied. However, if the material is subjected to an electric field during the cooling down process of its fabrication, these domains will be aligned in the direction of the field. When external stress is applied to such a material, the crystal lattices get distorted, causing changes in the domains and a variation in the charge distribution within the material. The converse effect of producing strain is caused when these domains change shape by the application of an electric field.

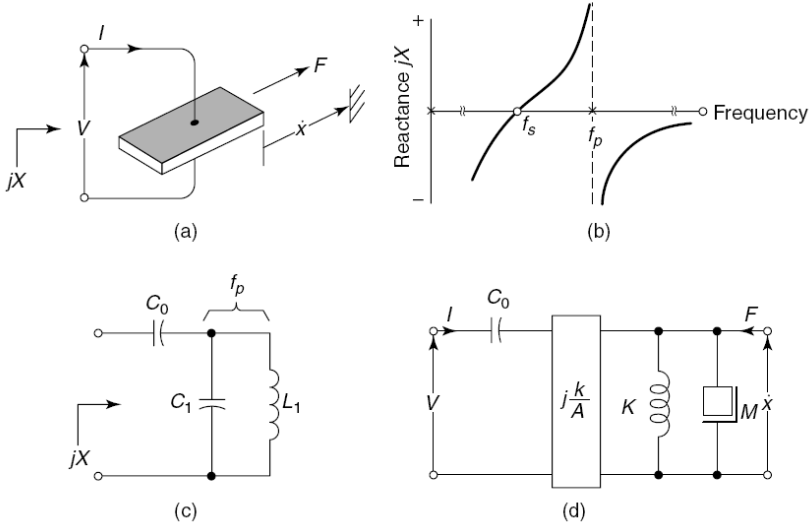


Figure 2.6 Development of equivalent circuit of a piezoelectric transducer[26]. The development of the equivalent circuit for a piezoelectric bar is illustrated in Figure 2.6[26]. The bar vibrates in the direction (with force F and velocity x) shown in the figure, by the application of an applied voltage (V). The reactance (jX) curve in (2.50)Figure 2.1(b) can be obtained by ignoring higher order modes of vibration, and the losses. One circuit configuration that results in similar reactance characteristics is shown Figure 2.6(c). The electromechanical equivalent circuit can be constructed from this, incorporates a gyrator with a resistance A and an inverter of reactance $j\kappa$ in addition to the corresponding spring constant K and mass M . The gyrator represents the nonreciprocal nature of the piezoelectric transducer. The inverter is required here since the gyrator converts the parallel resonant circuit to a series circuit [26]. The series combination of inverter and gyrator functions as a transformer with an imaginary turns ratio $j\kappa/A$. In general the piezoelectric transduction phenomenon is quadratic in nature, but may be assumed to be linear for small deformations. The electromechanical coupling can then be written as

$$Q = d_1 F \quad (2.31)$$

$$x = d_2 V \quad (2.32)$$

In these equations, d_1 and d_2 represent the piezoelectric charge modulus d in units 1 and 2, respectively. However, when both voltage and force are present, the following piezoelectric coupling equations are used:

$$Q = d_1 F + C_0 V \quad (2.33)$$

$$x = d_2 V + C_m F \quad (2.34)$$

where C_0 is the free capacitance and C_m the short-circuit compliance of the transducer. The electromechanical coupling coefficient is another important nondimensional quantity representing the performance of piezoelectric transducers. This is the ratio of mechanical work available to the electrical energy stored in the transducer [29]. The coupling coefficient depends on the type of material, mode of stress and the polarization of electric field. For a linear piezoelectric material, this is

$$\eta = \frac{d}{S\varepsilon} \quad (2.35)$$

where d is a constant for piezoelectric material, S is the elastic compliance and ε is the permittivity of the material.

PZT thin films have been developed using standard thin-film deposition techniques such as sputtering, and physical or chemical vapor deposition. Their use in sensors and actuators is inherently limited by the quality and repeatability of thin films obtained by these techniques.

2.4.3 Electromagnetic transducers

The magnetic counterpart of a moving plate capacitor is a moving coil inductor. This is yet another energy-storing transducer, the difference in this case being the forms of energy are magnetic and mechanical. A simplified sketch of such a transducer is shown in Figure 2.7. When a current i flows through the coil, the magnetic flux is ϕ . Neglecting nonidealities, such as electrical capacitance and resistance, and mechanical mass and friction, the constitutive relations for this device can be derived for the current (i) and force (F), in terms of displacement (x) and flux linkage. The conversion of energy takes place as a result of the interaction between these electrical and mechanical quantities in such a circuit.

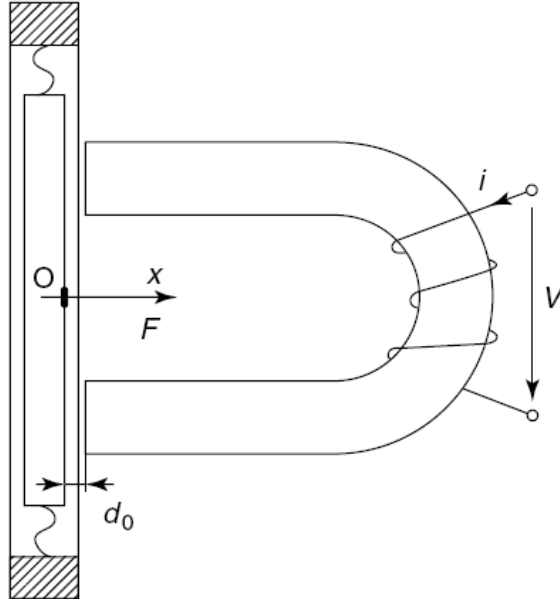


Figure 2.7 Schematic of an electromagnetic transducer.

In the transducer shown in Figure 2.7, the fixed armature has N turns of winding, and both this and the moving part are made of ferromagnetic materials. Assuming infinite permeability for the ferromagnetic parts, the reluctance is confined only to the gap between them. Considering both the gaps, the total reluctance \mathfrak{R} is approximately given by

$$\mathfrak{R} \approx \frac{2d(t)}{\mu_0 S} \quad (2.36)$$

where μ_0 is the permeability of air (medium in the gap) and S is its cross-sectional area. The reluctance at the rest position is

$$\mathfrak{R}_0 = \frac{2d_0}{\mu_0 S} \quad (2.37)$$

The position of the fixed element can, however, be expressed in terms of its rest position and the displacement as:

$$d(t) = d_0 - x(t) \quad (2.38)$$

Substituting Equations (2.37) and (2.38) into Equation (2.36), we get

$$\mathfrak{R} = \mathfrak{R}_0 \left[1 - \frac{x}{d_0} \right] \quad (2.39)$$

The inductance of the coil is expressed in terms of its reluctance as:

$$L = \frac{N^2}{\mathfrak{R}} = L_0 \left[1 - \frac{x}{d_0} \right]^{-1} \quad (2.40)$$

This may, however, be simplified for very small displacements using Taylor series expansions.

Ignoring higher-order terms, the inductance of this coil becomes

$$L \simeq L_0 \left(1 + \frac{x}{d_0} \right) \quad (2.41)$$

The voltage induced on the coil is

$$V = - \frac{d(Li)}{dt} \quad (2.42)$$

Substituting Equation (2.41) into Equation (2.42), the induced voltage is given as:

$$V \simeq -L_0 \frac{di}{dt} - L_0 i \frac{v}{d_0} \quad (2.43)$$

where v is the velocity of the moving plate. This leads to a nonlinear relationship for the electromechanical coupling. The stored magnetic energy is

$$W_m = \frac{1}{2} Li^2 = \frac{\varphi^2}{2L} \quad (2.44)$$

Assuming the principle of conservation of energy, this balances with the mechanical energy spent on the displacement. At any instant of time dt , the magnetic force used up for generating the displacement is given by

$$F_{\text{magnetic}} = \frac{\partial W_m}{\partial x} \quad (2.45)$$

As done with the electrostatic case, the nonlinearities of these expressions for electromechanical coupling can be linearized, by defining the components of the flux as:

$$\varphi = \varphi_0 + \varphi_d \quad (2.46)$$

Assuming that the dynamic component $\varphi_d \ll \varphi_0$, the relation between induced magnetic voltage and the dynamic component of current becomes [from Equation (2.43)]

$$V_d = -L_0 \frac{di_d}{dt} - L_0 I_0 \frac{v}{d_0} = -L_0 \frac{di_d}{dt} - \frac{\varphi_0}{d_0} v \quad (2.47)$$

The dynamic component of the magnetic force can be approximated as (

$$\left(F_{mag}\right)_d = \frac{\varphi_0}{d_0} i_d + \frac{\varphi_0^2}{L_0 d_0^2} x \quad (2.48)$$

Miniaturization of an electromagnetic actuator requires fabrication of magnetic thin films and current-carrying coils. Although few attempts have been made in this direction, the overall size of devices developed so far are not very small. Coupled with this is the difficulty in isolating magnetic field between adjacent devices, which makes fabrication of integrated microdevices challenging.

2.4.4 Electrothermal actuators

In electrothermal actuators, heat is applied to a bimorph beam the expansion of which is used to generate the mechanical moment required for the actuation. Large deflections and greater energy density are achievable with this scheme. But electrothermal transducers are too slow to be of any use at the frequencies of interest to us. However, for the sake of completion a brief discussion of their principles is given here. Several configurations are reported in the literature for this kind of actuator.

Several other configurations of micromachined thermal actuators are also reported in literature, for example, the difference in electrical resistance of a wide and a narrow arm in a bimorph structure (see Figure 2.8; [30]) is used to generate the necessary deflection. This difference causes variation in the heat produced and hence thermal expansion of the two arms. Based on the dimensions of the structure shown in Figure 2.8(a), an equivalent model of the cantilever can be obtained in (b). The cross sectional view of the structure is shown in Figure 2.8(c) to indicate various layers of materials. It is possible to obtain a second-order differential equation to represent its model [30]:

$$k_p \frac{d^2 T}{dx^2} + J^2 \rho = \frac{S}{h} \frac{T - T_s}{R_T} \quad (2.49)$$

where k_p is the thermal conductivity of polysilicon, T is the operating temperature, T_s is the substrate temperature, J is the current density, ρ is the resistivity of polysilicon, S is the shape factor, R_T is the thermal resistance between the polysilicon microbeam and the substrate, and h is the thickness of the beam.

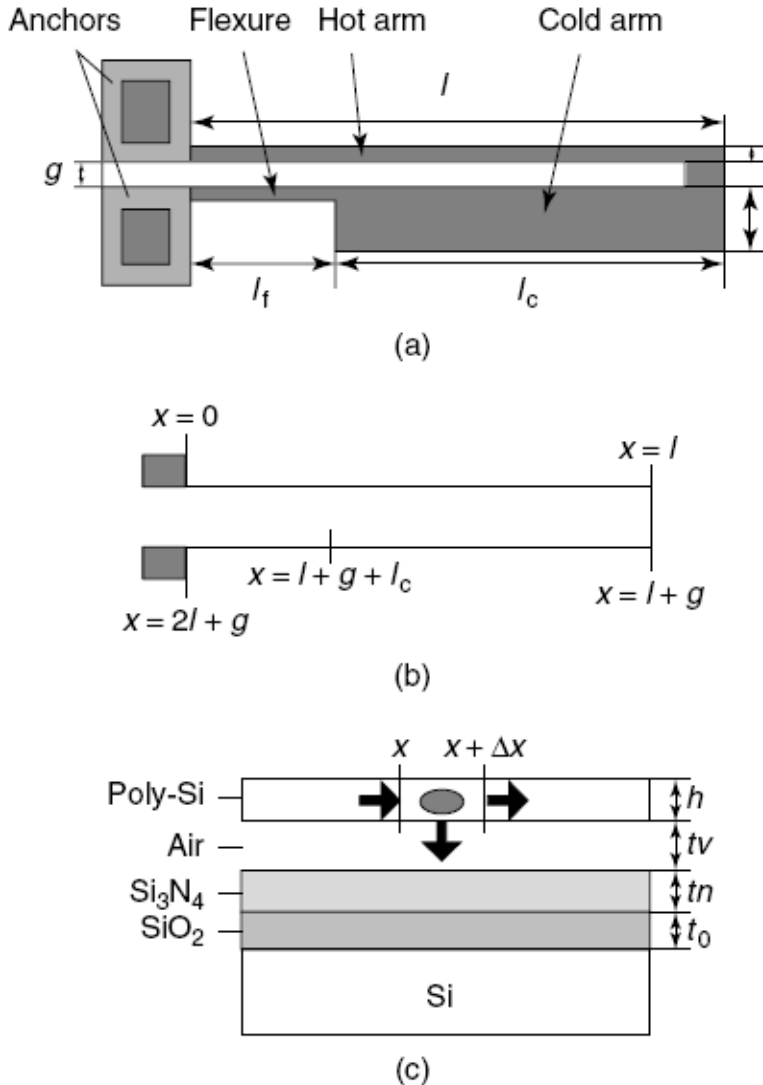


Figure 2.8 Bimorph electrothermal transducer.

2.4.5 Other Transducers

Other transducers which will not be described into details are listed.

- *Electrodynamic transducers.* This is one of the very common types of electromechanical actuation scheme. The primary component is a current-carrying moving coil such as the one commonly used in loud speakers. When a current flows through the coil it is deflected in the direction shown with a force F and velocity v .

- *Electrostrictive transducers.* Electrostriction is the phenomenon of mechanical deformation of materials due to an applied electric field. This is a fundamental phenomenon present to varying degrees in all materials, and occurs as a result of the presence of polarizable atoms and molecules. An applied electric field can distort the charge distribution within the material, resulting in modifications to bond length, bond angle or electron distribution functions, which in turn affects the macroscopic dimensions of the material. The phenomenon of electrostriction is very similar to piezoelectricity. One of the fundamental difference between the two is the closeness of transition temperature of the material to the operating temperatures. This accounts for the improved strain and hysteresis properties for electrostrictive materials.
- *Magnetostrictive transducers.* Certain ferromagnetic materials show deformation when subjected to a magnetic field. This phenomenon, commonly known as magnetostriction, is reversible and is also called the Joule and Villari effect.

2.4.6 Comparison of electromechanical actuation schemes

A brief comparison of some of the electromechanical transducers discussed above is presented in Table 1.4. Owing to its simplicity, electrostatic actuation is the most preferred, especially in microdevices. The control signal here is voltage, which is easy to manipulate in electrical circuits. However, these devices require greater environmental protection as electrostatic fields are prone to attract dust, which could affect the performance of associated CMOS circuits. Electromagnetic and electrodynamic actuators are based on Lorentz force effects. The current-carrying coil is stationary in the former case, whereas in the latter it is moving. These are ideally suited when large currents are possible, even with lower voltages. However, they are prone to problems with power dissipation, but are tolerant to dust and humidity.

Actuators based on piezoelectricity, magnetostriction and electrostriction depend on changes in strain produced by an applied electric or magnetic field in some special materials used

Most of these transduction schemes are nonlinear. That is, the transfer function between electrical (voltage or current) and mechanical (force or displacement) terms is not linear. Such nonlinearities distort the filtered signal and may cause loss of fidelity. One approach to

overcome this difficulty is to restrict the signal to very small variations about a dc bias. It is fairly reasonable to assume that the response to these small signal variations is linear.

Table 2.3: Comparison of electromechanical transducers

Actuator	Fractional stroke (%)	Maximum energy density (J cm^{-3})	Efficiency	Speed
Electrostatic	32	0.004	High	Fast
Electromagnetic	50	0.025	Low	Fast
Piezoelectric	0.2	0.035	High	Fast
Magnetostrictive	0.2	0.07	Low	Fast
Electrostrictive	4	0.032	High	Fast
Thermal	50	25.5	Low	Slow

2.5 Microsensing for MEMS

Various microsensing and microactuation mechanisms have been developed for MEMS for diverse applications. Some of the commonly used sensing and actuating principles are introduced in this section. Many microsensors based on different sensing principles for MEMS have been developed [31-32], including chemical sensors, gas sensors, optical sensors, biosensors, thermal sensors and mechanical sensors. Some of the major sensing mechanisms for mechanical microsensors are introduced in the following sections.

2.5.1 Capacitive sensing

Capacitive sensing utilizes the diaphragm-deformation-induced capacitance change to convert the information of pressure, force, etc., into electrical signals such as changes of oscillation frequency, time, charge, and voltage. The structure of a typical capacitive microsensor is shown in Figure 2.9; an electrode on the flexible diaphragm and the other one on the substrate construct the sensing capacitor. The capacitive microsensors can be used for pressure, force, acceleration, flow rate, displacement, position and orientation measurement, etc.

For capacitive microsensors, the capacitance change is not linear with respect to the diaphragm deformation, and, also, the small capacitance (generally 1 to 3 pF) requires the measurement circuit to be integrated on the chip. But the capacitive sensing was found to have potential for higher performance than piezoresistive sensing in applications requiring high sensitivity, low pressure range and high stability [32].

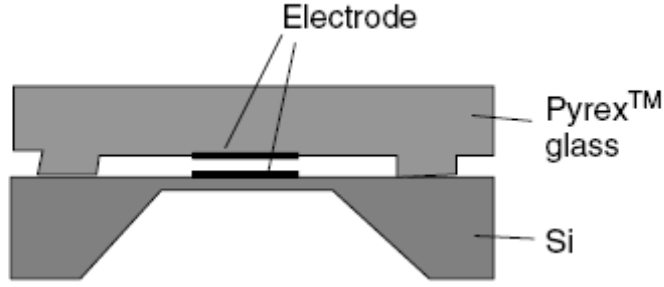


Figure 2.9: Capacitive sensing structure

2.5.2 Piezoresistive sensing

Piezoresistive sensing utilizes resistors where the resistance is varied through external pressure, to measure such physical parameters as pressure, force and flow rate or to be used as accelerometer.

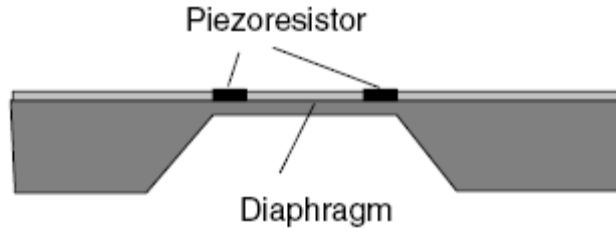


Figure 2.10: A piezoresistive sensing structure.

A typical structure for piezoresistive microsensors is shown in Figure 2.10. The resistors are usually built on a silicon diaphragm. The deflection of the diaphragm leads to the dimension change of the resistors, resulting in the resistance changing as a result of the piezoresistive effect in silicon:

$$\frac{\Delta R}{R} = (1 + 2\nu) \frac{\Delta l}{l} + \frac{\Delta \rho}{\rho} \quad (2.50)$$

where ΔR is the change of the resistance, R is the original resistance, ν is the Poisson ratio, Δl is the length change of the resistor, l is the original length of the resistor, and ρ and ρ represent the resistivity change and resistivity of the resistor, respectively. It is easily found that the resistance of the resistors used for this type of piezoresistive microsensor is proportional to the external pressure when the resistivity change is ignored, since the dimension change is proportional to the applied pressure.

2.5.3 Piezoelectric sensing

Piezoelectric sensing is based on the piezoelectric effect of piezoelectric materials. The electrical charge change is generated when a force is applied across the face of a piezoelectric film. For a piezoelectric disc of a given thickness t , the voltage (V) generated across the electrode disc when subjected to a stress (T) would be

$$V = gtT \quad (2.51)$$

where g is the piezoelectric voltage coefficient. Piezoelectric sensing is mostly used in sensors such as pressure sensors, force sensors, speedometers and accelerometers, hydrophones and microphones.

2.5.4 Other sensing systems

Other sensing systems which will not be described into details are listed.

- *Resonant sensing.* Resonant sensing is easily understood as the natural frequency of a string changing as a result of tensile force. In the developed resonant microsensor, strain caused by pressure on the diaphragm leads to the natural frequency of a resonator varying. By picking up the natural frequency variation of the resonator, the physical information that caused the strain will be sensed [33].
- *Surface acoustic wave sensors.* Surface acoustic wave (SAW) based sensors form an important part of the sensor family and in recent years have seen diverse applications ranging from gas and vapor detection to strain measurement [34]. A new breed of SAW-based actuator modelled on MEMS-based microactuators have also been recently announced [34]. Interdigital transducer (IDT) electrodes and SAW devices recently were found to be attractive sensors for various physical variables such as temperature, pressure, force, electric field, magnetic field, and chemical compounds. A SAW device usually is a piezoelectric wafer with IDT and reflectors on its surface. The IDT provides for the cornerstone of SAW technology. Its function is to convert the electrical energy into mechanical energy, and vice versa, for generating as well as detecting the SAW. The type of acoustic wave generated in a piezoelectric material depends mainly on the substrate material properties, the crystal cut and the structure of the electrodes utilized to transform the electrical energy into mechanical energy. The sensing action of such transducers involves any

influences that will alter the acoustic wave velocity and consequently the associated properties of the wave.

2.6 Applications of MEMS electrostatic actuators: Micromirrors

One of the most interesting applications of MEMS electrostatic actuators is the realization of thousands of movable reflective plates on the same chip: *micromirrors arrays*.

Micromirror arrays are spatial light modulators (SLM) that can modulate the phase or amplitude of incident light [35]. The main application areas of micromirror arrays are projection display systems[36], pattern generators in maskless lithography systems[37], optical scanners[38], printers, optical spectroscopy, aberration correction, adaptive optical systems [39] and switches and cross connectors in optical communication systems[40-41].

In the following subsections some of the most important applications of the micromirror arrays are described together with a small description of the existing devices in order to understand for what can be used the micromirrors we will analyze in this work. Large space is dedicated to the description of micromirrors for optical switching as they are the main focus of the devices designed, fabricated and measured in this work (Chapter 4)

2.6.1 Digital Light Processing

The first demonstration of a miniature ($\sim 2 \times 2$ mm) torsional mirror was by Kurt Petersen, while at *IBM* [15]. Quoting from this paper, Peterson predicts that “. . . silicon micromechanics may eventually find a practical implementation for displays (especially if silicon-driving circuitry can be integrated on the same chip, matrix addressing the two-dimensional array of mirrors-all electronically).” This statement proved to be truly prophetic, given the current success of MEMS

display products such as Texas Instruments' Digital Micromirror Device (DMD) [36] for Digital Light Processing.

Digital Light Processing (DLP) is a data projection technology from *Texas Instruments* that produces clear, readable images on screens in lit rooms. DLP is used in all ends of the projection spectrum, from data projectors that weigh only a few pounds to 60" rear-projection TVs to electronic cinema projectors for movie theaters. The technology uses a Digital Micromirror Device

(DMD), a chip with 400,000 to more than two million light switches that cancel or reflect light. Microelectromechanical mirrors, each $16\text{ }\mu\text{m}$ square, are built on top of a CMOS memory chip.

A DMD chip has on its surface several hundred thousand microscopic mirrors arranged in a rectangular array that corresponds to the pixels in the image to be displayed. The mirrors can be individually rotated plus or minus, to an on or off state. In the on state, light from the bulb is reflected onto the lens making the pixel appear bright on the screen. In the off state, the light is directed somewhere else (usually onto a heatsink), making the pixel appear dark (Figure 2.11).

The mirrors themselves are made out of aluminum and are around 16 micrometres across. Each one is mounted on a yoke which in turn is connected to two support posts by compliant torsion hinges. In this type of hinge, the axle is fixed at both ends and literally twists in the middle. Because of the small scale, hinge fatigue is not a problem and tests have shown that even 1 trillion operations does not cause noticeable damage. Two pairs of electrodes on either side of the hinge control the position of the mirror by electrostatic attraction. One pair acts on the yoke and

the other acts on the mirror directly. The majority of the time, equal bias charges are applied to both sides simultaneously. Instead of flipping to a central position as one might expect, this actually holds the mirror in its current position. This is because attraction force on the side the mirror is already tilted towards is greater, since that side is closer to the electrodes. To move the mirror, the required state is first loaded into an SRAM cell located beneath the pixel, which is also connected to the electrodes. The bias voltage is then removed, allowing the charges from the SRAM cell to prevail, moving the mirror. When the bias is restored, the mirror is once again held in position, and the next required movement can be loaded into the memory cell.

The bias system is used because it reduces the voltage levels required to address the pixels such that they can be driven directly from the SRAM cell, and also because the bias voltage can be removed at the same time for the whole chip, meaning every mirror moves at the same instant. The advantages of the latter are more accurate timing and a more filmic moving image.

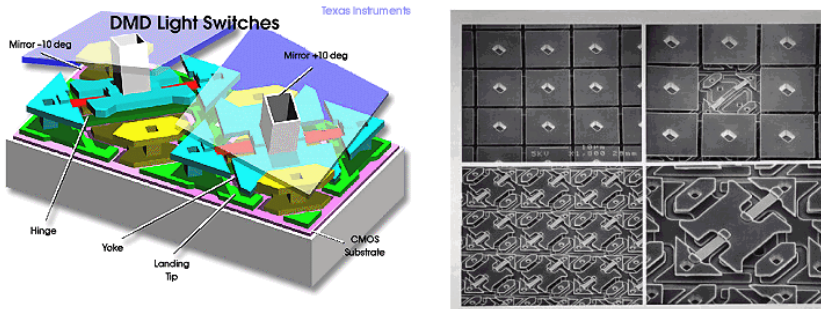


Figure 2.11: Schematic of two micromirrors. Mirrors pivot on a central post, and switching is achieved by electrostatic attraction; Scanning Electron Microscope image of 9 DMD mirrors. Top: Mirrors on posts. Bottom: Pivoting Structures.

(Source: Texas Instruments Literature)

2.6.2 Maskless Lithography

In order to reduce the cost for the realization of electronic devices the idea of maskless lithography has been investigated. Maskless lithography using a micromirror array has the merits as photomasks and mask alignment are not required. Instead of using a photomask, a simple driving circuit is used for mirror operations. The requirements of micromirrors for maskless photolithography devices include good reflectivity in the 365 nm UV region, uniform properties with respect to the driving characteristics and the optical reflectance of mirror plate, and a relative large (some degrees) deflection angle to avoid interference between reflected lights by neighboring mirrors. In this type of application, analog addressing and low hysteresis of the mirrors are very important features, whereas the fill factor of the mirrors is not as critical as for digital micromirror devices in projection display systems.

The mirror-like surface of the SLM is actually composed of thousands of tiny moveable mirrors, each with their own storage cell within the integrated circuit. As the design of the photomask is feed to the SLM, individual mirrors are either flexed or remain flat. Light reflected off the flexed mirrors is scattered — it cannot pass through and expose the photoresist on the photomask blank. Light reflected off the flat mirrors does pass through to expose the resist, creating the pattern of the photomask. The closest analogy to stepper lithography is that of a chromeless phase shifting mask, which creates dark areas by scattering light away from the surface of the quartz mask substrate. [42]

2.6.3 Optical Switching

As optical telecommunications networks become more complex, there is a need to be able to manipulate an increasingly larger number of optical signals in faster and more cost-effective ways. A large fraction of such manipulation is currently performed in an “electrical domain,” which involves converting the optical signals into electrical, performing required operations on the electrical signals, and then reconverting them into optical. However, for many of these operations, it is more cost effective to manipulate the optical signals directly in the “optical domain.” This is especially true for wavelength-division-multiplexed (WDM) transmission, where multiple optical wavelengths are used to transmit multiple independent signals through an optical fiber.

The most common and widely adopted example of such an all-optical operation is optical amplification for long-haul transmission. Optical switching is quickly becoming another case in which operating in the optical domain is more efficient.

Potential applications also include variable attenuators, gain-equalizing filters, and dispersion compensators, among others [43-45]. With constantly improving transmission systems and evergreater demand for flexibility and more effective bandwidth utilization in the WDM optical networks, there is a clear demand for cost-effective ways of switching multiple individual optical signals. The two most common switching applications are WDM add-drop multiplexers and large cross-connects.

Very often, no operation is necessary, other than redirecting the wavelength channels from multiple inputs to any of the multiple outputs. Such operation can be performed at a fraction of the cost by dealing with individual optical signals directly, in the optical, rather than electrical, domain.

For such switching solutions to be viable, they should introduce very little optical degradation, such as optical power loss (insertion loss), polarization-dependent loss (PDL), or dispersion.

The signals should be switched with high contrast and low optical crosstalk—very little optical power should be allowed to leak into undesired outputs.

Microelectromechanical systems (MEMS) technology allows the construction of microscopic equivalents of macroscopic optomechanical elements. Many micromechanical optical elements have been demonstrated, including mirrors, shutters, filters, lenses,

and polarizers. Such elements maintain the superior optical performance characteristics of their macro counterparts but are much smaller, faster, and often less expensive. Optical components and subsystems based on such individual elements constitute one portion of the optical MEMS application space, enabling improved components and subsystems.

More important, such optical MEMS can easily incorporate thousands of batch-fabricated individual elements in a single compact package, perfectly suitable for the demanding high complexity optical networking applications. These can be key enablers of high-complexity subsystems, opening a different portion of the application space by providing new functions, ones that are impossible to achieve any other way.

It is possible to construct a strictly nonblocking single-stage optical cross-connect (OXC) using MEMS tilt mirrors. Such an OXC, or photonic switch, connects any of the input signals (ports) to any of the output ports and can be arbitrarily reconfigured without disturbing any of the other connections through the switch, a basic requirement for optical networking where live traffic paths cannot be interrupted during provisioning or restoration of other paths. The number of distinct configurations connecting all inputs individually to outputs, and thus the number of different states that the system can be in, is , which qualifies it as a high-complexity system.

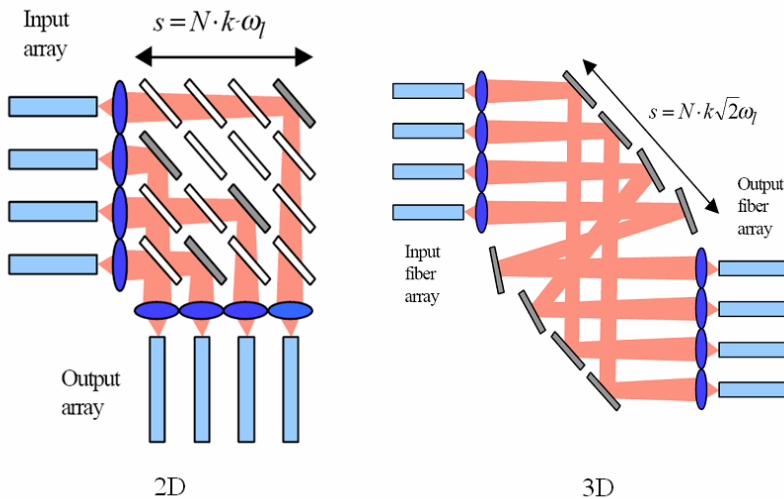


Figure 2.12: Scheme of 2D and 3D Optical Cross Connect (OXC)

When optical switching using MEMS is considered, two general approaches have been used. In one, the individual switching elements

(such as mirrors) are binary, capable of being in only two discrete states [46]. The total number of elements in such systems is equal to the number of cross-connections possible and therefore proportional to N^2 . It is commonly referred to as a “two-dimensional” (2-D) or digital architecture, since the binary mirrors and light paths are all located in one plane. In a different approach, called “three-dimensional” (3-D) or beam steering, each element is capable of being in at least distinct states, and then the total number of elements required is proportional to the number of ports [47](Figure 2.12). Here, part of the complexity is pushed down into the individual MEMS element, while the whole system is simplified.

In the 2-D architectures, the optical performance penalties (e.g., insertion loss) are often directly proportional to the number of elements acting on, or that may act upon, an individual optical signal, that is, proportional to N^2 . This penalty increases as the number of elements grows and thus limits the practical size of such fabrics to 32×32 or below. On the other hand, for 3-D, the total number of elements scales as N , and each optical signal is only going through a fixed number of elements, independent of the number of ports. Thus, the optical performance does not deteriorate when the number of ports is increased, as long as the internal complexity performance of individual MEMS elements can keep up with the increasing

This dictated the choice of the 3-D OXC architecture schematically shown in Fig. 2. In 3-D architecture, the light signals from input ports are directed onto beam-steering micromirrors on the “input” MEMS chip. Each of the micromirrors steers the beam toward a micromirror on the “output” chip associated with the required

output port. The state of the output micromirror chip is complimentary to the input chip so that the light coming from the input chip is directed toward an output port. In this architecture, micromirror elements are used to accomplish an cross-connect function.

The key requirement of such mirrors is that they be able to tilt and individually address the mirrors on the other chip (the complexity requirement). Not only does this mean more mirrors per chip, but also larger tilt angles or larger reflectors

for each individual mirror are necessary for increasing the port count. Although, in operation, the micromirrors only have to tilt to fixed angular positions to address the other chip, when N is large, it is easier to build continuously tiltable analog mirrors and set them into the desired positions by supplying the correct control signals.

Micromirrors for use in such systems have to satisfy a complex set of requirements. First, they have to be able to address the number of ports required with the light of a specified wavelength. The mirrors that can tilt in two directions are clearly advantageous in this regard. The diffraction-limited number of ports that can be independently addressed with low insertion loss and low crosstalk using such mirrors is proportional to the second power of the linear mirror size and the maximum tilt angle. Correspondingly, the main requirement is that these

mirrors must be capable of achieving and maintaining large tilt angles while, at the same time, having large reflector sizes.

It is desirable that the mirrors have high mechanical resonance frequencies for high speed and isolation from ambient vibrations, high stability and no hysteresis. The control scheme should be simple and voltages should preferably be moderate to simplify the drive electronics and decrease the number of electrical input–output to the large mirror arrays. Finally, devices should be fully manufacturable and reliable, maintaining their characteristics over long times, wide temperature range, large numbers of switching cycles, and while being tilted at high angles for prolonged periods.

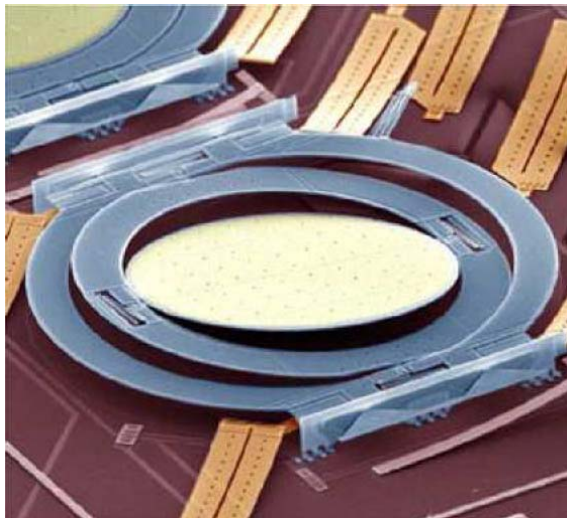


Figure 2.13: Surface-micromachined beam-steering micromirror[Lucent].

2.6.4 Examples of micromirrors for Optical Switching

2.6.4.1 Surface-Micromachined Mirrors

A representative example of surface-micromachined mirror construction is shown in a scanning electron microscope (SEM) micrograph in Figure 2.13. The basic elements are a 500 μm -diameter round reflector suspended from a fixed frame via a gimbal mount—a gimbal ring and four torsional springs, two for each axis. A gimbal ring is elastically attached to the fixed frame by a set of two spring assemblies, and is capable of rotation around a single axis. The reflector is attached to the ring by a second set of assemblies and can rotate with respect to the ring around a second orthogonal axis, thus achieving two degrees of freedom of tilt. The frame is held by the two hinged sidewalls rotated 90 out of the substrate plane and four curved assembly arms [13]. Below the device, one can partly see the electrodes and electrical interconnects fixed on the silicon nitride dielectric surface covering the Si substrate.

Neighboring mirrors located 1 mm away on each side are partly visible on the micrograph as well. The later generation of the surface-micromachined mirrors has similar basic elements, with the reflector size increased to further lower the insertion loss.

The mirror moves with respect to the gimbal ring and the frame by elastically deforming the attaching torsional springs. The springs are designed to be sufficiently stiff to enable fast mechanical switching times—below 5 ms—and to decouple the structure from gravity effects, mechanical vibrations, and low-frequency mechanical noise. Several polysilicon beams in a folded serpentine configuration form a spring. This design does not rely on very fine critical dimension (CD) control, decreasing variations and increasing the yield. It also minimizes the spring footprint and keeps the elastic stress in a deformed spring small and evenly distributed, thus ensuring high reliability. Such springs also make the whole structure strain-relieved—insensitive to possible small variations in residual and thermally induced stress of the structural polysilicon—ensuring high uniformity and thermal stability of the device. The springs of the device shown in Figure 2.13 incorporate an extra feature, a microfabricated bearing, to further stiffen the suspension in the vertical and lateral directions. This allows one to achieve a slight increase in the angular range. However, the bearings are not used in any of our more recent mirrors. The lateral and vertical translational

stiffness of these springs remains high, offering the angular range required for a 256-port cross-connect, while operating in a pure-flexure mode, without any moving parts in direct mechanical surface contact. This eliminates even the remote possibility of mechanical wear in these devices.

2.6.4.2 Bulk Micromachined mirrors

As deep reactive ion etching (DRIE) and other comparably new and more advanced Si processing technologies become more mature and available, new possibilities for building the OXC-type micromirrors open up. Such alternative fabrication processes typically contain a smaller number of steps and may be less complex and less expensive than surface micromachining.

In such approaches deep Si-etching and wafer-bonding techniques are used to enable the large-amplitude rotation. Eliminating the need for self-assembly reduces the optically dead space between the mirrors, allowing an increase in the fill factor, which can lead to an increase in the number of ports or decrease in the required tilt angle.

In addition, when a combination of bonded wafers is used, wider possibilities are opened up for the electrical interconnect design, which becomes less constrained by the mechanical moving structures. This process allows more flexibility in choosing the thickness of the single-crystal silicon layer comprising the micromirror reflector. The choices for the distance between the mirror and the electrodes are also wider. This allows a greater range of design possibilities and better optimization in the trade off between the reflector curvature, reflector size, switching speed, angular range, and actuation voltage. Finally, since electrodes and electrical interconnect wires can be done separately from the mirrors, higher wiring density can be achieved and more mirrors can be put on a single chip. This makes this process especially well suited to building larger switch fabrics.

An example is described in [47]. The device consists of a monolithic layer of SCS anodically bonded to a glass substrate with metallic electrodes.

Ground shields are patterned on the areas under the mirror to minimize actuator drift caused by substrate charging effects.

The silicon layer is bulk micromachined to define the actuator gap, mirror plate, gimbal, and suspension springs all from the same single-crystal layer. Electrical connection to the top silicon is made through a silicon-to-metal lead transfer established by overlapping some of the

glass metal to the bonding area. The monolithic construction is advantageous since it minimizes stresses in the structure (Figure 2.14). The dimensions of the mirror are generally in the 0.5–1 mm diameter range. Several types of torsional flexures have been used including straight and folded beams. Thick and narrow straight flexures have the highest ratio of vertical to angular stiffness; however they tend to be susceptible to bonding stresses as the torsional spring constant is a

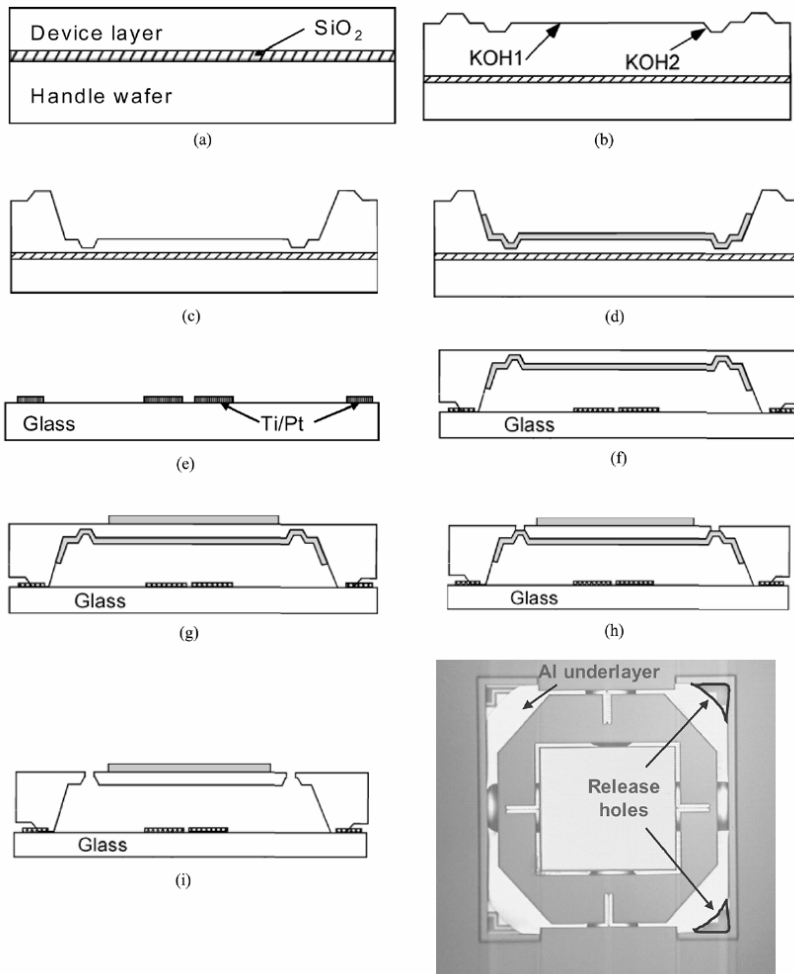


Figure 2.14: Simplified fabrication process for the bulk micromachined mirror array. (a) 4 inch SOI wafer; (b) after KOH etch 1 and 2; (c) after KOH etch 3; (d) deposit and pattern Al DRIE etch stop; (e) deposit and pattern Ti/Pt electrodes on glass; (f) anodic bond and dissolve handle wafer; (g) deposit and pattern Ti/Au mirrors; (h) etch the mirror silicon; (i) etch Al layer and release. Sem Micrograph of the device [47]

function of the tension, and their resistance to shock is limited by the small elongation necessary to reach the fracture strain. Compared to straight beam flexures, folded beam flexures have a lower stiffness ratio, but their resistance to shock is much improved as it is possible to design the folds

such that fracture strain is not reached even in the case of a hard stop at the substrate.

2.6.4.3 Drawbacks

Both described structures presents several drawbacks. The surface micromachined micromirror by Lucent is realized through a very complicated process so the possibility of this device to be competitive is quite low

On the other side the bulk micromachined mirror has less fabrication steps but it is also not cost effective expensive as it requires a SOI wafer (10 times more expensive) and a critical wafer bonding is present in the process flow.

One of the goals of this thesis is to find an alternative way to realize cost-effective surface micromachined micromirrors for optical switching. We will describe in chapter 4 a micromirrors array realized in a commercial single structural layer technology.

Chapter 3

Surface Micromachining: Polysilicon and Polysilicon germanium

In Chapter 2 it has been shown that surface micromachining represents a totally different process from bulk micromachining. Instead of forming mechanical structures in the silicon substrates, these devices are fabricated in thin films deposited on the surface.

Early surface micromachined structures used metal mechanical layers but polysilicon became dominant in the 1980s and today still represents the most important material for surface micromachining.

In this chapter we will present a thick polysilicon technology produced by *STMicronics: THELMA*. This process has been used to fabricate all the devices presented in this thesis.

Hence an alternative technology under development at *IMEC* (Interuniversity Microelectronic Center) which uses PolySilicon Germanium as structural layer is presented. Specifically is presented a study of stress gradient optimization of this layer. This challenging technology has the great advantage that the structural layer (for the low deposition temperature) can be deposited on top of CMOS.[49]

3.1 Thick PolySilicon Technology

3.1.1 THELMA by STMicronics

The thick-film epitaxial polysilicon technology, called *THELMA*, was developed in *STMicronics* for serial manufacturing of high-volume low-frequency devices (accelerometers)[50]. The availability of this technology in the industrial environment was one of the main reasons for using it for our work on electrostatic actuators. Also, the high thickness of the structural layer offers several advantages for mechanical filter design. These advantages are

- a. a strong stiffness along the vertical axis, which allows to release large-area structures without sticking occurrence;
- b. the possibility to implement capacitive transducers with large electrode surface.

The structure of a complete device fabricated in the technology is presented in Figure 3.1. The device is constituted of two polysilicon layers. One is the structural layer $15\ \mu\text{m}$ thick, the second is a buried layer ($0.45\ \mu\text{m}$ thick), used for biasing. As shown in Figure 3.1, these layers are separated by two oxide layers, and contact is possible between the structural layer and buried layer and between the structural layer and the substrate.

The manufacture of the device is done in the following way. First an oxide layer is deposited on the substrate ($2.5\ \mu\text{m}$ thick) in a uniform way, then buried polysilicon is deposited and doped ($0.45\ \mu\text{m}$ thick). A sacrificial oxide is subsequently deposited ($1.6\ \mu\text{m}$ thick). These steps are shown in Figure 3.1(a).

Then opening in the oxide layer is realized by sacrificial etching, defining future contacts to the substrate and to the buried layer (Figure 3.1(b)).

The next steps are the epitaxial growth of the structural layer polysilicon ($15\ \mu\text{m}$), its p-doping and a definition of trenches by dry anisotropic etching (Figure 3.1(c) and (d)).

The last step is a time-controlled removal of the sacrificial oxide Figure 3.1(e) and the release. Thanks to a time-controlled releasing, the removed oxide width from trench edges is $3\ \mu\text{m}$. From the releasing method, it is clear that the maximal width of a structure (or part) that can be released is $6\ \mu\text{m}$.

Trenches are realized by dry anisotropic etching. Because of the high thickness of the structural layer, only relatively large trenches can be achieved. The minimal authorized trench width defined on the mask level is $1.6\ \mu\text{m}$.

Actual trench width is increased because of overetching. The overetching width is $0.5 \pm 0.1\ \mu\text{m}$ from each side, therefore the actual minimal achievable trench width is about $2.6 \pm 0.2\ \mu\text{m}$. this value is too high to achieve an efficient capacitive transducer. The impossibility to realize narrow gap values constitutes the main disadvantage of the *THELMA* technology for micro-mechanical filter design.

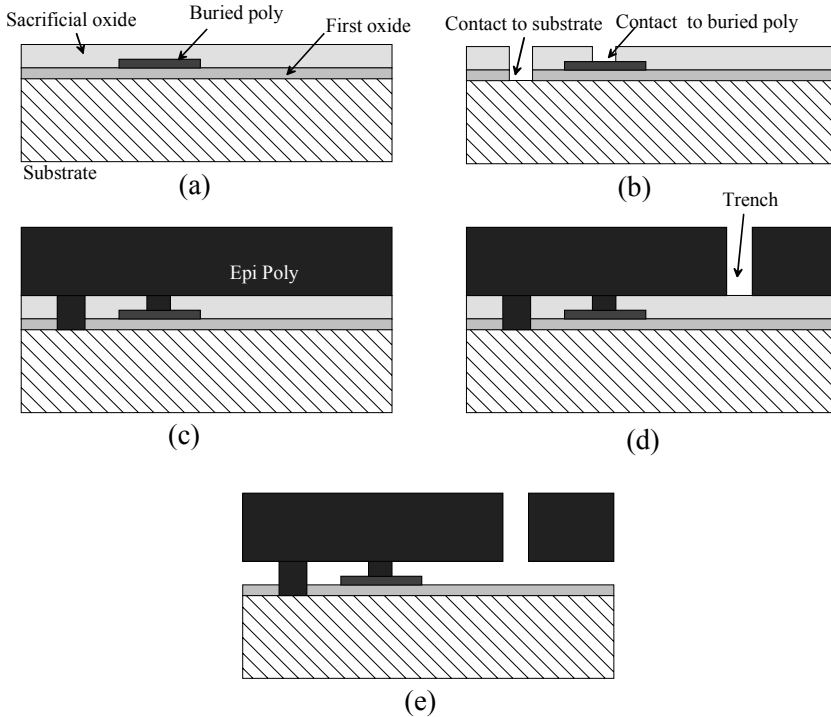


Figure 3.1: Fabrication of the device: (a) deposition of the first oxide, buried layer and sacrificial oxide; (b) definition of contacts to ground and to buried layer by sacrificial etching; (c) structural epitaxial polysilicon layer growth; (d) etching of the epitaxial layer (e) etching of sacrificial oxide.

3.2 Poly Silicon Germanium as structural material

Poly-SiGe has recently been promoted as a material suitable as structural layer for several MEMS applications [20,51-52]. This can be attributed to the fact that good electrical and mechanical properties can be obtained at much lower temperatures (down to 400 °C) [53-54] as compared to poly-silicon (above 800 °C), which has been the most widely used material for MEMS structural layers so far [15]. This low processing temperature enables post-processing MEMS on top of CMOS without introducing significant changes in the existing CMOS foundry processes. Such monolithic integration will result in much smaller system sizes and is expected to offer improved MEMS performance at the same time [20, 51-52].

Much of the low temperature poly-SiGe reported, uses the low pressure chemical vapour deposition (LPCVD) technique [55-56]. The main setback of the LPCVD method is its low deposition rate (2–30

nm/min). Growth rates can be considerably increased by the use of plasma. Plasma enhanced chemical vapour deposition (PECVD) of poly-SiGe at temperature of 520–590 °C with a growth rate of 100–200 nm/min has been described before [57]. Unlike for LPCVD, the PECVD, growth rate does not change much with the temperature [57]. However, because of the high growth rate, the PECVD layers deposited at CMOS compatible temperatures are normally amorphous [57].

The poly-SiGe films used in this work are deposited by a multilayer process that combines the use of LPCVD for low temperature crystallisation and PECVD for high growth rates [53]. The LPCVD layer serves as a crystallization seedlayer for the PECVD layer, making it possible to obtain a crystalline film with a high growth rate at a CMOS-compatible temperature. The deposition process must be optimised to obtain a low residual stress and stress gradient, since high values for these are detrimental to the device performance.

The knowledge of the stress variation across the film can help in understanding which parameters are important, so that they can be adjusted to obtain the best results.

Several ways to determine the stress profile over thickness have already been reported in the literature [58-61]. Some of these methods require complex, expensive equipment and complex data analysis. Others are simple but not very reliable as will be shown later in this article. In this work, we present a new method to obtain the stress profile. The stress gradient values measured at different thicknesses are fitted to the best possible function. A relative stress profile is deduced from this function. Finally, the stress profile is completely determined using the measured average residual stress. This method is applied to two thick poly-SiGe films with somewhat different stack-build up. The results are also compared with those from other methods described in literature. Also, based on the model, a prediction is made for the top layer thickness that would ensure a zero stress gradient for the complete film stack.

3.3 Determination of stress profile and optimization of stress gradient in PECVD poly-SiGe films

3.3.1 Measurements principles and fitting model

Large stress variations in the vertical direction can cause free-standing structures to have unfavourable out-of-plane bending. This might cause anomalous behaviour of designed structures upon release. Thus, it is extremely important to control the stress profile through the thickness of a film.

A cantilever beam exhibiting a concave shape, i.e. a bending away from the substrate, is associated with a positive stress gradient (bottom layers more compressive than top layers); and a cantilever beam bending towards the substrate, i.e. a convex beam, is associated with a negative stress gradient (bottom layers more tensile than top layers) .

The first order expression for the stress σ in a micromachined beam is given as a combination of a constant stress σ_0 (stress at zero thickness) and a linear contribution,

$$\sigma(z) = \sigma_0 + \Gamma \cdot z \quad (3.1)$$

where Γ is the linear stress gradient (figure 1).

As a result of a linear stress variation with thickness, a bending moment M is produced:

$$M = \int_A \left(\sigma(z) \cdot \left(z - \frac{T}{2} \right) \right) dA \quad (3.2)$$

$$M = \int_A \left(\sigma_0 \cdot \left(z - \frac{T}{2} \right) + \Gamma \cdot z \cdot \left(z - \frac{T}{2} \right) \right) dA = w \cdot \Gamma \cdot \int_0^T z \cdot \left(z - \frac{T}{2} \right) dz = \Gamma \cdot \frac{wT^3}{12} \quad (3.3)$$

where A is the cross-sectional area of the beam, w is the width and t is the thickness.

Throughout the article, the coordinates described in Figure 3.2 are used, except for the description of Yang's method. Sometimes t is used instead of z to discriminate between the integration variable and primitive variable.

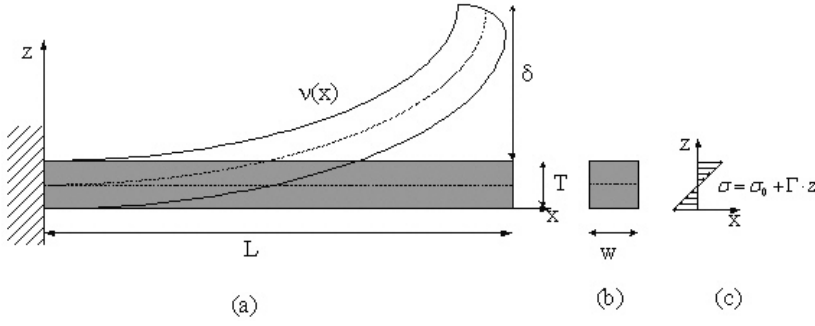


Figure 3.2: Deflection of a cantilever (a); cross section (b); linear stress profile (c).

The equation relating the deflection of the cantilever $v(x)$ and the bending moment M is [62]:

$$\frac{d^2 v(x)}{dx^2} = \frac{M}{EI} \quad (3.4)$$

where E is the Young's modulus and $I = \frac{w \cdot T^3}{12}$ is moment of inertia of the section. Solving this differential equation with the boundary conditions $x = 0 \Rightarrow v = 0$ and $x = 0 \Rightarrow \frac{dv}{dx} = 0$, the following relation is obtained:

$$v(x) = \frac{Mx^2}{2EI} = \frac{\Gamma}{12} \frac{T^3 wx^2}{2EI} = \frac{\Gamma}{2E} \cdot x^2 = a \cdot x^2 \quad (3.5)$$

After measuring the deflection $\delta = a \cdot L^2$ of the free-end (or the constant a) of a cantilever of length L , the linear stress gradient Γ can be calculated from:

$$\Gamma = E \cdot \frac{2\delta}{L^2} = 2 \cdot E \cdot a \quad (3.6)$$

To determine the exact stress profile in the layers, a differential technique can be used. Layers are thinned to different thicknesses and the linear stress gradient is measured. The problem is now reduced to rebuilding the stress profile from the stress gradient values thus obtained. A lot of methods have been proposed to achieve this [58-61]. A brief description of a few of them is given below.

3.3.1.1 Yang's method

In this method, the stress profile is assumed to be a polynomial function of Z , the coordinate perpendicular to the neutral surface

($Z=0$) of the cantilever [59] (Figure 3.3). The neutral surface is the plane in a beam under transverse pressure, at which the fibres are neither stretched nor compressed, or where the longitudinal stress is zero.

$$\sigma(Z) = \sum_{k=0}^n a_k Z^k \quad (3.7)$$

where a_k are coefficients to be determined.

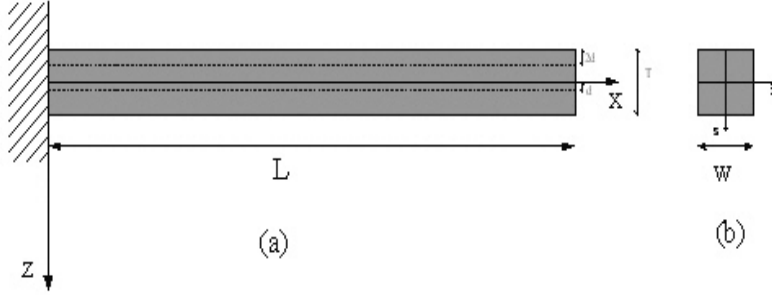


Figure 3.3: The system of reference and the parameters described in the paper of Yang [59]: cantilever (a); cross section (b).

The amount of vertical deflection of free-end of cantilevers varies with removal of its surface layers. If the surface layer is removed by $2d$, the neutral axis shifts down by d . The shifted coordinate is $z = Z + d$. The stress profile in this new coordinate is:

$$\sigma(z) = \sum_{k=0}^n a_k (z - d)^k \quad (3.8)$$

The end point deflection δ can be derived from equation (3.2), and (3.8) [59].

$$\delta = -\frac{L^2}{E} \left\{ \frac{1}{2} \cdot a_1 - t^2 d \cdot a_2 + \left(\frac{3}{2} d^2 + \frac{3}{40} t^2 \right) \cdot a_3 - \left(2d^3 + \frac{3}{10} t^2 d \right) \cdot a_4 + \right. \\ \left. + \left(\frac{5}{2} d^4 + \frac{3}{4} t^2 d^2 + \frac{3}{224} t^4 \right) \cdot a_5 - \left(3d^5 + \frac{3}{2} t^2 d^3 + \frac{9}{112} t^4 d \right) \cdot a_6 + \dots \right\}$$

Since $t = T - 2d$, where T is the original film thickness, δ is a function of d only. Knowing the end-deflections of cantilevers for different layer thicknesses, the unknown coefficients a_k (except a_0) can be obtained by curve fitting. After measuring the average stress (σ_M), the stress value at the neutral surface (a_0), can be calculated from:

$$a_0 = \sigma_M - \frac{1}{T} \int_{-T/2}^{T/2} \sum_{k=1}^n a_k Z^k dY \quad (3.9)$$

3.3.1.2 Van Der Donck's method

In another method, the stress profile was considered as a linear function between two measured thicknesses [60]. This method was applied to a 2 μm thick LPCVD poly-Si Ge layer. The value of the stress σ_1 at the thickness t_1 is given by the following relation:

$$\sigma_1 = \sigma_0 + \Gamma_1 \cdot t_1 \quad (3.10)$$

where σ_0 is the stress value at lower surface of the layer and Γ_1 is stress gradient measured at the thickness t_1 . At thickness t_2 a stress gradient Γ_2 is measured, from which a stress σ_2 can be determined by ensuring that the bending moment of the obtained stress profile is the same as that calculated from Γ_2 (Figure 3.4).

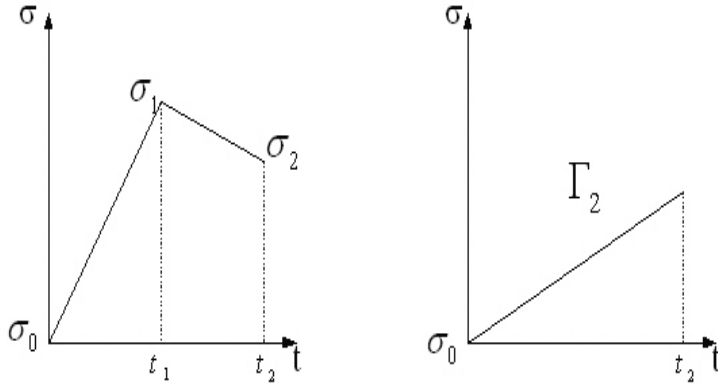


Figure 3.4: Graphical description of Van Der Donck's method [60].

Similarly, the stress at the thickness t_i with $i = 3, \dots, n$ can be deduced so that the relative profile is obtained [60]. If the mean stress value σ_M is known, σ_0 can be deduced from the following expression:

$$\sigma_0 = \sigma_M - \frac{1}{T} \cdot \int_0^T \Delta\sigma(z) \cdot dz \quad (3.11)$$

where T is the thickness of the poly-SiGe layer and $\Delta\sigma(z) = \sigma(z) - \sigma_0$ is the relative profile.

This approach gives a profile without a continuous derivative, and is most suitable when a very few data points are available.

3.3.1.3 Furtsch's method

In the method presented by M. W. Furtsch [61], it is assumed that for a given stress profile, the linear stress gradient is the slope of the least squares fitted line to the stress data points (Figure 3.5). To simplify the calculus, it is first assumed that $\sigma_0 = 0$ and $\Delta\sigma(z) = \sigma(z) - \sigma_0$ is calculated, because the stress profile is invariant to translations. It is easy to deduce $\sigma_1 = \sigma_0 + \Gamma_1 \cdot t_1 = \sigma_0 + \Delta\sigma_1$. To find the value of the stress σ_2 in t_2 , we consider that Γ_2 is the slope of the best linear fit to the data points, that is, it is the value that minimizes the following expression:

$$F(\Gamma_2) = (\Delta\sigma_1 - \Gamma_2 \cdot t_1)^2 + (\Delta\sigma_2 - \Gamma_2 \cdot t_2)^2 \quad (3.12)$$

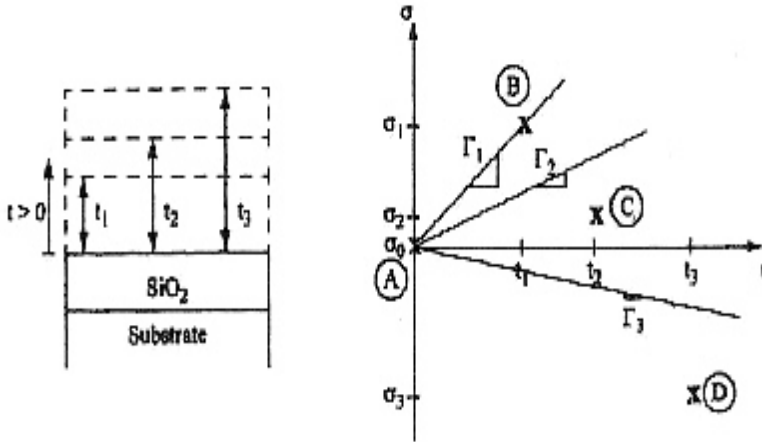


Figure 3.5: Graphical description of Furtsch's method [61].

Then we must find the value that verifies the relation $\frac{dF}{d\Gamma_2} = 0$:

$$\Gamma_2 = \frac{\Delta\sigma_1 \cdot t_1 + \Delta\sigma_2 \cdot t_2}{t_1^2 + t_2^2} \quad (3.13)$$

In this way, if we know Γ_2 , it is possible to deduce σ_2 after a simple step:

$$\Delta\sigma_2 = \frac{\Gamma_2 \cdot (t_1^2 + t_2^2) - \Delta\sigma_1 \cdot t_1}{t_2} \quad (3.14)$$

With an analogue procedure, it is possible to obtain the other values of the stress at the thickness t_i with $i = 3, \dots, n$:

$$\Delta\sigma_3 = \frac{\Gamma_3 \cdot (t_1^2 + t_2^2 + t_3^2) - \Delta\sigma_1 \cdot t_1 - \Delta\sigma_2 \cdot t_2}{t_3} \quad (3.15)$$

$$\Delta\sigma_n = \frac{\Gamma_n \cdot \left(\sum_{i=0}^n t_i^2 \right) - \sum_{i=0}^{n-1} \Delta\sigma_i \cdot t_i}{t_n}$$

In this way, the relative stress profile $\Delta\sigma(z) = \sigma(z) - \sigma_0$ can be obtained. σ_0 is again deduced from the mean stress value σ_M (equation (3.11)).

This method is just a mathematical method, not based on physical considerations or relations. It is therefore difficult to evaluate if the obtained results are correct.

3.3.1.4 Proposed method

The method proposed here differs from the methods described previously in that the other methods directly rebuild the stress profile from the stress gradient values. Whereas, in this method, first linear stress gradients at different thicknesses are measured, and then a best fit approximation of the data is done to obtain the function $\Gamma(z)$. Then the stress profile is deduced from $\Gamma(z)$. To perform this operation, an analytical relation between $\Gamma(z)$ and $\sigma(z)$ must be found. The bending moment has the following expression:

$$M(t) = \frac{\Gamma(t) \cdot w \cdot t^3}{12} = w \cdot \int_0^t \sigma(z) \cdot \left(z - \frac{t}{2} \right) \cdot dz \quad (3.16)$$

Dividing each term by w and differentiating with respect to t , the following expression is obtained:

$$\frac{1}{w} \frac{d^2 M(t)}{dt^2} = \frac{d^2}{dt^2} \left(\frac{\Gamma(t) \cdot t^3}{12} \right) = \frac{\sigma(t)}{2} + \frac{t}{2} \frac{d\sigma(t)}{dt} - \frac{\sigma(t)}{2} = \frac{t}{2} \frac{d\sigma(t)}{dt} \quad (3.17)$$

From this a differential equation relating $\sigma(t)$ and $\Gamma(t)$ can be deduced:

$$\frac{d\sigma(t)}{dt} = \frac{2}{t} \frac{d^2}{dt^2} \left(\frac{\Gamma(t) \cdot t^3}{12} \right) \quad (3.18)$$

This relation is then integrated:

$$\int_0^z \frac{d\sigma(t)}{dt} dt = \int_0^z \frac{2}{t} \frac{d^2}{dt^2} \left(\frac{\Gamma(t) \cdot t^3}{12} \right) dt \quad (3.19)$$

Thus the relative stress profile can be deduced when a good approximation of the function $\Gamma(t)$ is obtained:

$$\Delta\sigma(z) = \sigma(z) - \sigma_0 = \int_0^z \frac{2}{t} \frac{d^2}{dt^2} \left(\frac{\Gamma(t) \cdot t^3}{12} \right) \cdot dt \quad (3.20)$$

Finally it is possible to find σ_0 from the relative stress profile and residual stress using equation (3.11).

Several methods can be used to obtain a good approximation of $\Gamma(t)$. However, the function must be $C^2(0, T)$ (continuous with first and second continuous derivatives in the measurement interval). In this work we use two possible different fits for $\Gamma(t)$:

1. Polynomial: $\Gamma(t) = \sum_{k=0}^n a_k \cdot t^k$
2. Exponential: $\Gamma(t) = \sum_{i=1}^m A_i \cdot e^{b_i \cdot t}$

With the polynomial fit, the formula for the relative stress profile is as follows:

$$\begin{aligned} \Delta\sigma(z) = & a_0 \cdot z + a_1 \cdot z^2 + \frac{10}{9} \cdot a_2 \cdot z^3 + \frac{5}{4} \cdot a_3 \cdot z^4 + \\ & + \frac{7}{5} \cdot a_4 \cdot z^5 + \frac{14}{9} \cdot a_5 \cdot z^6 + \frac{12}{7} \cdot a_6 \cdot z^7 + . \end{aligned} \quad (3.21)$$

With the exponential fit, the following expression for the relative stress profile is obtained:

$$\Delta\sigma(z) = \sum_{i=1}^m A_i \cdot e^{b_i \cdot z} \cdot \left(\frac{1}{3b_i} + \frac{2}{3} z + \frac{b_i}{6} z^2 \right) - \frac{A_i}{3b_i} \quad (3.22)$$

Both methods are used and the errors are compared in order to choose the best approximation. It is also possible to use other fitting functions; the choice can be made after an analysis of the data with the objective of reducing the error.

3.3.2 Experimental details

The stress profile of a 10 μm thick poly Si-Ge layer is derived. The layer is deposited in three steps (figure 5) [52]:

1. deposition of a very thin PECVD seedlayer (94 nm) as a nucleation layer for the CVD layer;
2. deposition of a CVD layer (370 nm) to help in crystallizing the top PECVD layer;
3. deposition of a PECVD layer until 10 μm .

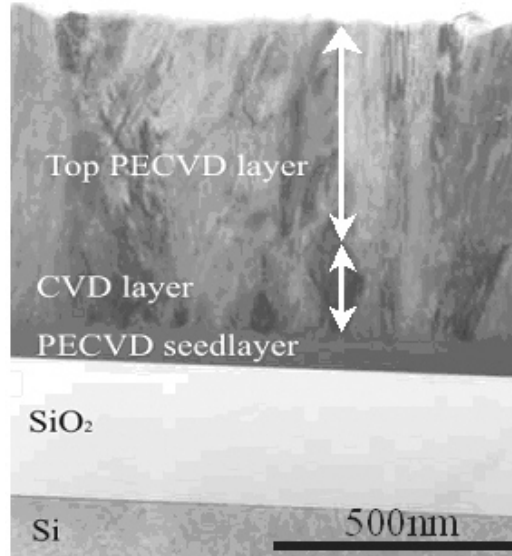


Figure 3.6: Cross section of a PECVD poly silicon germanium layer.

The whole process is done with the same mixture of silane, germane, diborane and hydrogen at a process temperature of 450°C .

The films deposited with this process have a tensile stress of 72 MPa and a positive linear stress gradient of $6.5 \text{ MPa}/\mu\text{m}$. The overall stress and stress gradient can be reduced by depositing a top compressive layer. Using a $1.6 \mu\text{m}$ thick PECVD poly-SiGe layer with a higher SiH_4 percentage in the gas mixture as the top layer results in a lower residual stress of 57 MPa and a lower linear stress gradient of $1.6 \text{ MPa}/\mu\text{m}$ [53].

As each of the described films has a concentration of Germanium between 62% and 65%, the Young's modulus is assumed to be $E=147 \text{ MPa}$ [63]. The films are deposited on the top of a 250 nm layer of

silicon dioxide, which is used as sacrificial layer and the substrate is a 6" Si <100> wafer.

A RIE-ICP (Reactive Ion Etching with Inductive Coupled Plasma) etcher with SF_6 and O_2 (Oxford Plasmalab System 100) is used to thin down the Poly-SiGe films. A very low RF power and rather low inductive power is used to avoid physical sputtering and damage during the etching process.

HF vapour etching is used to remove the silicon dioxide (sacrificial layer) and to release the structure without stiction [64].

After releasing the structures, the deflection of the cantilever is measured using both an optical microscope and a laser profilometer.

With the optical microscope the deflection of the free-end of the cantilever is measured by focusing the optical beam first on the top of the anchored structures and then on the top of the free end of the cantilever. With the laser profilometer a linear scan of the profile of the cantilever is made in order to obtain a measurement of its deflection ($v(x)$). The deflection of the cantilever is described by equation (3.4). A fit of the data with this parabolic function ($v(x) = a \cdot x^2$) was done after measuring the profile.

As the results obtained with these two methods are consistent, only the results obtained with laser profilometer are presented. When it is not possible to use laser profilometer, the measurements from the optical microscope are reported.

3.3.3 Results and discussion

To investigate whether the RF power used for thinning damages the layer and thus causes variations in the stress profile or not, a 1.5 times higher power setting than normal was tried. The layer was thinned down to 6.2 μm and with this power setting a stress gradient of 17.5 MPa/ μm was measured. This value is consistent with the values obtained with lower power (see

Table 3.1). Thus, it can be assumed that there is no variation of stress caused by atomic peening.

Table 3.1: Mean Residual Stress = 72 MPa; Thickness = 10 micrometers. Coefficient of parabolic fit a and deflection of the free end of cantilever for 1 mm long beam.

Thickness (μm)	Coefficient a ($10^{-5} \mu\text{m}^{-1}$)	Deflection δ (μm)	Γ (MPa/ μm)
10	2.26	22.6	6.6
9.5	2.85	28.5	8.4
8.4	3.38	33.8	9.9
7.6	3.79	37.9	11.1
7.2	4.24	42.4	12.5
6.6	4.49	44.9	13.2
6.5	4.7	47.0	13.8
5.45	6.46	64.6	19
5.3	7.52	75.2	22.1
4.0	11.29	112.9	33.2
3.9	11.38	113.8	33.5
1.6	46.94	469.4	138
0.95	59.1	591	174

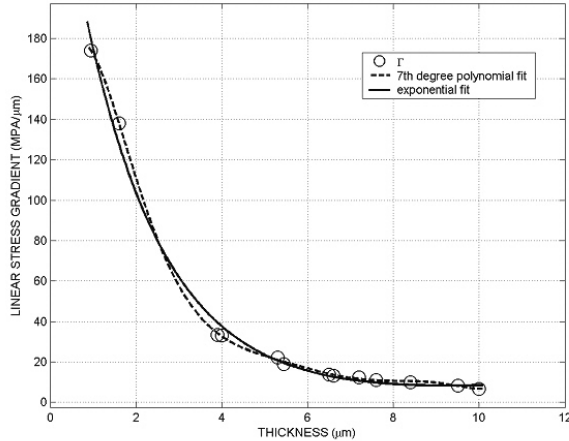


Figure 3.7: Exponential and polynomial fit of the linear stress gradient for 10 μm poly SiGe layer.

Table 3.1 shows the experimental results for the 10 μm thick layer. The values of the coefficient a of the parabolic fit for the deflection of the cantilevers, the deflection δ of the free-end of the cantilevers, and the

respective stress gradient values at different film thicknesses are reported. These stress gradient values are fitted with two different functions: a polynomial and an exponential function. The coefficients for the seven-degree polynomial fit and the exponential function are reported in Table 3.2. The fitted functions are shown in Figure 3.7.

The calculated stress profile for the 10 μm poly-SiGe (Figure 3.8) layers shows that the largest variation in stress can be found in the initial part of the film consisting of two compressive layers: the PECVD seedlayer, which is amorphous and the LPCVD layer, which is polycrystalline with V-shaped grains. This microstructure often leads to a positive stress gradient. The stress in the rest of the layer is tensile and almost constant. This tensile stress is partly caused by the difference in thermal expansion between the SiGe layer and the Si substrate. The little oscillations of the stress in this part of the layer are due to the polynomial approximation. By using the exponential fit, these oscillations can be avoided.

Table 3.2: Coefficients of polynomial and exponential fit for 10 μm thick layer.

Polynomial	Exponential
$a_0 = 116.3;$	$A_1 = 295.1;$
$a_1 = 205.9;$	$b_1 = -0.531;$
$a_2 = -219.5;$	$A_2 = 1.109;$
$a_3 = 84.74$	$b_2 = 0.1849$
$a_4 = -16.85;$	
$a_5 = 1.841;$	
$a_6 = -0.1051;$	
$a_7 = 0.002451$	

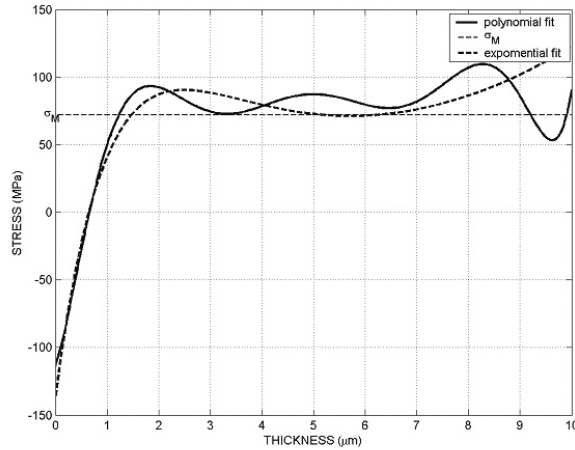


Figure 3.8: Stress profile for 10 μm layer with the polynomial and exponential fit.

A stress profile was also derived using the other methods described above (Figure 3.9), and different problems were encountered in each case. By using Yang's method, we found a problem of conditioning in the solution of the system. Van Der Donck's method does not work well with a large number of data points and gives unreasonable results. Furtch's method is only a mathematical method and doesn't take experimental results into account.

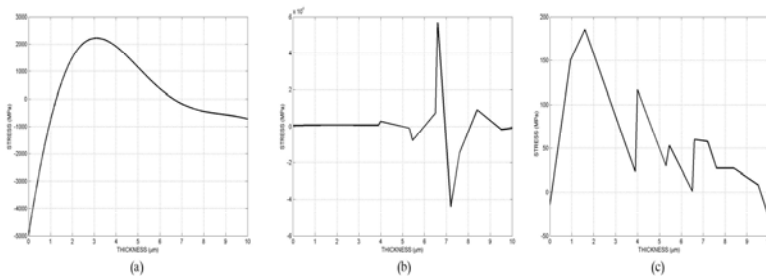


Figure 3.9: Stress profile for 10 μm layer with the other three different methods: (a) Yang, (b) Van der Donck (This profile appears initially flat because of the scale), and (c) Furtch.

The measurements of the linear stress gradient for the 11.6 μm PECVD poly-SiGe layer with Si-rich layer on top (Table 3.3) were fitted with a polynomial function of the fifth degree. Because there are

Table 3.3: Mean Residual Stress = 57 MPa; Thickness = 11.6 micrometers. Coefficient of parabolic fit a and deflection of the free end of cantilever for 1 mm long beam.

Thickness (μm)	Coefficient a ($10^{-5} \mu\text{m}^{-1}$)	Deflection δ (μm)	Γ (MPa/ μm)
11.77	0.55	5.5	1.6
11.2	1.19	11.9	3.5
10.8	1.35	13.5	4
9.9	2.48	24.8	7.3
8.6	3.66	36.6	10.75
7.8	4.65	46.5	13.7
5.2	7.8	78.0	23.2
3.7	17.66	176.6	51.9
2.6	24.8	248	72.9
1.9	46	460	135

only 10 measurement points, a fit with a higher degree polynomial leads to too much oscillations.

In order to improve the fit of the linear stress gradient for the 11.6 μm layer, the measurement points of the 11.6 μm thick film are combined with the values for the 10 μm layer. In Figure 3.10 both these fits are shown and in table 4 the coefficients are reported.

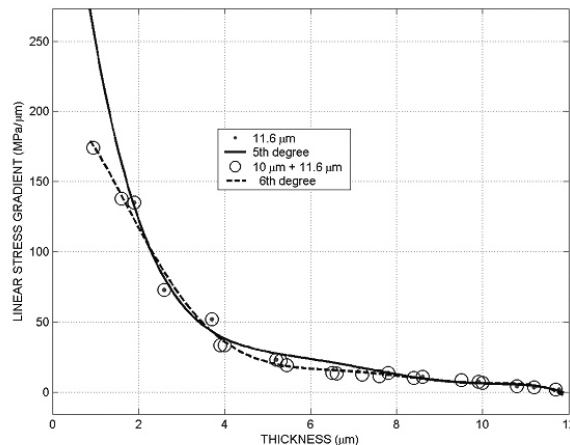


Figure 3.10: Polynomial fit of the linear stress gradient in 11.6 μm poly silicon germanium layer considering also the measurements obtained from 10 μm layer

From these two graphs it is possible to deduce the stress profiles of the 11.6 μm thick film (Figure 3.11). The top compressive

layer causes the stress to drop at the top of the film, which leads to a reduction in the linear stress gradient.

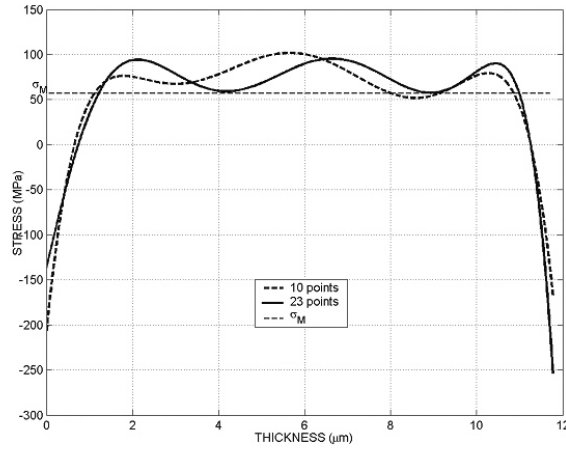


Figure 3.11: Stress profiles for 11.6 μm layer with only measurements from it

Table 3.4: Coefficient of polynomial fit for the 11.6 μm thick layer points) and with also measurements from 10 μm layer.

	11.6 μm data	10 μm + 11.6 μm data
Calculated value for the variables	$a_0=487.4$ $a_1=-312.4;$ $a_2=85.23;$ $a_3=-11.53;$ $a_4=0.7598;$ $a_5=-0.01944;$	$a_0=196.3 ;$ $a_1=14.9;$ $a_2=-52.86;$ $a_3=16.9;$ $a_4=-2.319;$ $a_5=0.1495;$ $a_6=-0.003713$

One of the objectives of this work was to try to obtain the top layer thickness value for which the linear stress gradient is equal to zero. Using the data measured (both for the 11.6 μm layer and for the 10 μm layer), a function for the linear stress gradient as a function of thickness was obtained. Using this function, the thickness of the top layer where the stress gradient equals zero can be obtained by extrapolation.

This top layer thickness value was determined for different fits. The calculated value of the thickness for a zero stress gradient lies between $11.7 \mu\text{m}$ and $11.9 \mu\text{m}$ (Figure 3.12). It is not possible to give a better approximation because this value depends on the fit used. Since this value is obtained through extrapolation, it can only be regarded as a guide for the development work and experimental verification will still be needed.

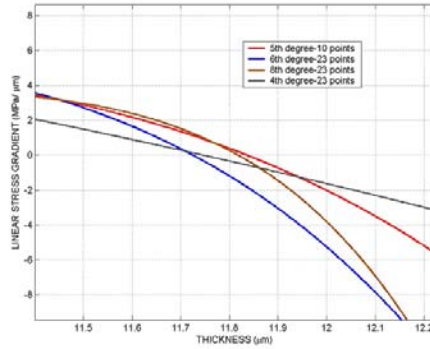


Figure 3.12: Thickness of zero stress gradient calculated with different fits.

Chapter 4

Micromirrors for Optical Switching: Models and Fabrications

Several MEMS torsional micromirrors for optical switching have been presented [65-67], most of them fabricated by using bulk micromachining, others with surface micromachining, but requiring delicate assemblage steps after releasing [66]. As it is important to balance device performance and scalability with the maturity, reliability, and manufacturability of the process, a big effort is made in the direction of avoiding these steps and some solutions, like self-assembly [68-69] have been proposed. A robust solution should also avoid multi-wafer assemblies without limiting the angular dynamics of the micromirror. This is not readily obtainable in thin-film surface micromachining technologies because of the small gaps between moving and fixed parts. In the mirror proposed in this work, this problem is overcome by substituting a single micromirror with an array of smaller phased micromirrors, a structure resembling a Venetian blind (Figure 4.1).

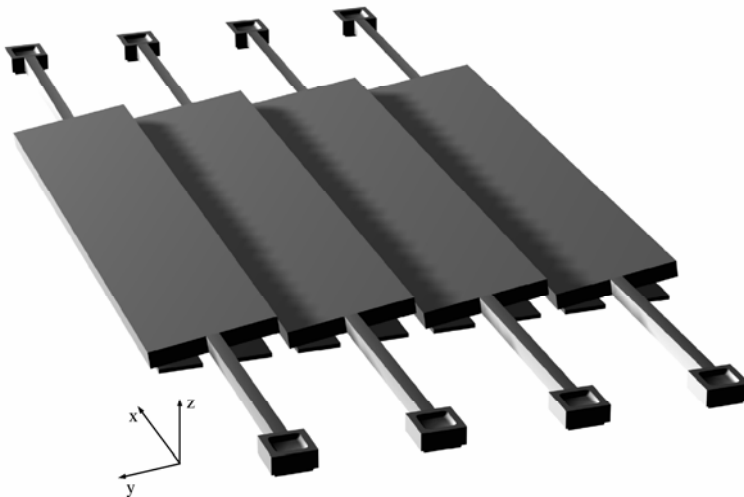


Figure 4.1: Simplified structure of the array of phased micro-mirrors and underlying actuation.

The characteristics of torsional micromirrors have been studied extensively [69-71]. Like most electromechanical Microsystems, micromirrors show an instable behaviour (the pull-in) above a critical deflection angle, when the electrostatic force/torque overcomes the mechanical force/torque and the movable plate of the micromirror snaps abruptly to the fixed electrode plate. The pull-in parameters, namely, pull-in angle, pull-in voltage, and pull-in displacement, define the maximum performances of the micromirror. The pull-in parameters are determined by the geometrical design of the micromirror and actuating electrodes. In order to design these structures, a accurate model of the expected characteristics as a function of the design parameter is necessary.

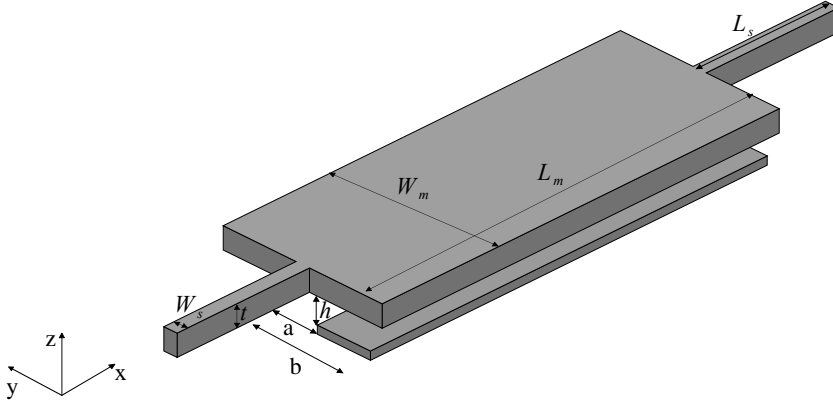


Figure 4.2: Scheme of the mirror with all geometrical parameters.

If a voltage is applied on the electrodes under the mirror, an electrostatic force is produced. The force pushes down the mirror and produces a torque, which tilts it. After a certain angle the electrostatic torque is always larger than the restoring elastic force, hence there is the pull-in.

In this chapter we will carry out a theoretical study on the electromechanical characteristics of the micromirrors. All the mirrors we will analyze have the structure described in Figure 4.2. The dimension of the mirrors are $L_m \times W_m \times t$, the hinges are $L_s \times W_s \times t$. In the first part of this chapter we will calculate the force and the torque produced by a voltage V as function of the rotation angle θ . Later, an analytical expression for the pull-in angle (and then voltage) will be deduced. Then a brief description of the torsional mechanical problem will be shown, in order to calculate the elastic torsional constant and the expected characteristics will be drawn. A small signal equivalent circuit of the micromirror will be presented.

Hence the design flow of some micromirrors arrays in THELMA technology by *STMicroelectronics* is presented. Successively the problem of the bending of the micromirror will be introduced and an original model taking into account this phenomenon will be described. Coupled electro-mechanical FEM simulation with ANSYS and COMSOL are used as validation of the presented models[72].

Four arrays have been fabricated and some measurements which confirm expected characteristic are shown.

Finally a new test die with several structures which will be fabricated by using PolySilicon Germanium technology (on top of standard CMOS) by IMEC is presented.

4.1 Torsional electrostatic actuators

Let' consider a cross section of the mirror, the origin of the coordinate system is placed in O (Figure 4.3), so the electrode on the substrate is extended by the abscissa a to b , h_0 is the initial gap between the electrode and the mirror (i.e. for rotation angle $\theta = 0$). The gap as function of the angle and of the abscissa can be expressed as $h(y, \theta) = h_0 - y \tan(\theta)$. As the rotation angles will be small, the approximate expression $\tan(\theta) \approx \theta$ will be used.

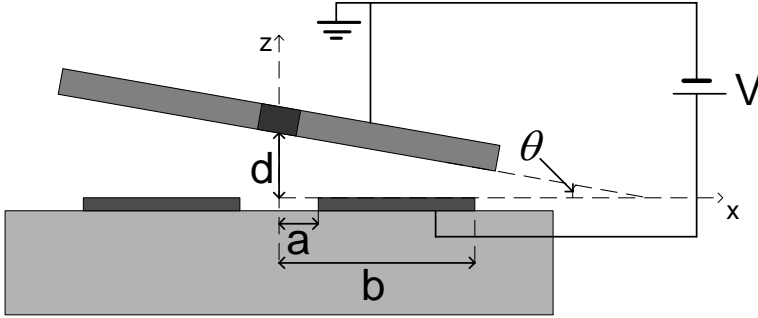


Figure 4.3: Cross section of a micromirror

An analytical expression for the capacitance between the mirror and the electrode can be deduced by supposing that it can be considered as a series of capacitors of area $L_m dy$:

$$c_m(y, \theta) = \frac{2\varepsilon_0 L_m}{h_0 - y\theta} dy \quad (4.1)$$

$$C_m(\theta) = \int_a^b c_m(y, \theta) = \frac{\varepsilon_0}{\theta} \cdot L_m \cdot \ln \left(\frac{h_0 - a \cdot \theta}{h_0 - b \cdot \theta} \right) \quad (4.2)$$

If a voltage V_0 is applied the electrostatic energy stored in this capacitor is:

$$U_E(\theta) = \frac{1}{2} \cdot C_m(\theta) \cdot V_0^2 \quad (4.3)$$

From the equation (4.3) it is possible to calculate the total torque acting on the mirror as a function of θ by using the principle of virtual works:

$$M_E(\theta) = \frac{\varepsilon_0 \cdot L_m \cdot V_0^2}{2 \cdot \theta^2} \cdot \left(\ln \left(\frac{h_0 - b \cdot \theta}{h_0 - a \cdot \theta} \right) + \frac{h_0}{h_0 - b \cdot \theta} - \frac{h_0}{h_0 - a \cdot \theta} \right) \quad (4.4)$$

As regard the electrostatic force for unit of x-length, it can be calculated from eq. (4.1) by considering that $z = h(y)$:

$$f_E(y, \theta) = \frac{1}{2} \frac{dc_m}{dz} V_0^2 = \frac{\varepsilon_0 L_m V_0^2}{(h_0 - y\theta)^2} \quad (4.5)$$

From eq. (4.5), the total force acting on the mirror is deduced:

$$F_E(\theta) = \int_a^b f_E(y, \theta) dy = \frac{\varepsilon_0 \cdot L_m \cdot V_0^2}{2 \cdot \theta} \cdot \left(\frac{1}{d - b \cdot \theta} - \frac{1}{d - a \cdot \theta} \right) \quad (4.6)$$

If we want to find a voltage-angle relation, by defining K_θ the total torsional elastic constant, the following equilibrium relation is written for the mirror:

$$M_E(\theta) = K_\theta \theta \quad (4.7)$$

By substituting M_E with the formula in (4.4) and solving for V_0 , the following expression is deduced:

$$V_0(\theta) = \sqrt{\frac{2K_\theta \theta^3}{\varepsilon_0 L_m \left(\ln \left(\frac{h_0 - b \cdot \theta}{h_0 - a \cdot \theta} \right) + \frac{b \cdot \theta}{h_0 - b \cdot \theta} - \frac{a \cdot \theta}{h_0 - a \cdot \theta} \right)}} \quad (4.8)$$

4.2 Pull-in Voltage

A very important parameter in the realization of electrostatic actuated micromirrors is the pull-in voltage, and it should be useful to find an analytical expression for it. In this section we will deduce the pull-in voltage for the specific case of micromirrors described in this work. It is important to consider that the results cannot be generalized because this parameter strongly depends on the size and on the position of the electrodes.

The mirror is long L_m , hence the maximum rotation angle is given by the expression:

$$\theta_{max} = \arcsin\left(\frac{2h_0}{W_m}\right) \approx \frac{2h_0}{W_m} \quad (4.9)$$

The equation (4.4) can be rewritten by introducing the parameter θ_{max} and defining the parameters $\alpha=2a/W_m$ and $\beta=2b/W_m$:

$$M_E(\theta) = \frac{\varepsilon_0 W_m^2 L_m \cdot V_0^2}{4h_0^2 (\theta/\theta_{max})^2} \cdot \left(\ln\left(\frac{1-\beta(\theta/\theta_{max})}{1-\alpha(\theta/\theta_{max})}\right) + \frac{1}{1-\beta(\theta/\theta_{max})} - \frac{1}{h_0-\alpha(\theta/\theta_{max})} \right) \quad (4.10)$$

Introducing $\theta_N=\theta/\theta_{max}$ and supposing $\alpha \approx 0$:

$$M_E(\theta_N) = \frac{\varepsilon_0 L_m \cdot V_0^2}{2\theta_N^2 \theta_{max}^2} \cdot \left(\ln(1-\beta\theta_N) + \frac{\beta\theta_N}{1-\beta\theta_N} \right) \quad (4.11)$$

At the equilibrium the following equation is verified:

$$M_E(\theta) = K_\theta \theta = K_\theta \theta_N \theta_{max} \quad (4.12)$$

At the pull-in angle, the equality of the derivative is also valid:

$$\frac{d}{d\theta_N} M_E(\theta_{N_{PIN}}) = K_\theta \theta_{max} \quad (4.13)$$

Calculating the derivative, we obtain:

$$\frac{\varepsilon_0 L_m V_0^2}{2\theta_{max}^2 \theta_{N_{PIN}}^2} \left(2\ln(1-\beta\theta_{N_{PIN}}) + \frac{3\beta\theta_{N_{PIN}}}{1-\beta\theta_{N_{PIN}}} - \frac{\beta\theta_{N_{PIN}}}{(1-\beta\theta_{N_{PIN}})^2} \right) = K_\theta \theta_{max} \quad (4.14)$$

Multiplying both the terms of eq. (4.12) by $\theta_{N_{PIN}}$ and substrating the result to the eq. (4.13), the following equation is obtained:

$$\frac{\varepsilon_0 L_m V_0^2}{2\theta_{max}^2 \theta_{N_{PIN}}^2} \left(3\ln(1-\beta\theta_{N_{PIN}}) + \frac{4\beta\theta_{N_{PIN}}}{1-\beta\theta_{N_{PIN}}} - \frac{\beta\theta_{N_{PIN}}}{(1-\beta\theta_{N_{PIN}})^2} \right) = 0 \quad (4.15)$$

$$3\ln(1-\beta\theta_{N_{PIN}}) + \frac{3\beta\theta_{N_{PIN}} - 4(\beta\theta_{N_{PIN}})^2}{(1-\beta\theta_{N_{PIN}})^2} = 0 \quad (4.16)$$

Numerically solving this equation, the normalized pull-in angle is deduced:

$$\beta\theta_{N_{PIN}} = 0.44042 \dots \quad (4.17)$$

Hence the pull-in angle is equal to:

$$\theta_{N_{PIN}} = 0.4404 \frac{h_0}{b} \quad (4.18)$$

From eq.(4.8), the pull-in voltage is deduced:

$$V_{PIN} = \sqrt{0.827 \left(\frac{d}{b} \right)^3 \frac{K_\theta}{\varepsilon_0 L_m}} \quad (4.19)$$

It is important to underline that the described analysis is valid if a pure torsional model (the mirror rotates without deflection in z-direction) is supposed. This hypothesis is not true in general: the electrostatic force in z-direction also causes a vertical bending of the mirror. This effect can be taken in account by considering that gap h_0 is not constant but is a function of F_E , so of the applied voltage V_0 . This means that is not possible to solve the preceding equations. Successively we will present a model which takes in account also this effect.

4.3 Torsional Elastic constants of the hinges

As it has been said in the previous section, the mirror is subtained from two torsional hinges. It is interesting to have a closed form for the elastic constant of this springs. Each of them can be schematized like a beam to which is applied a torque T_x , so the elastic torsional constant is defined as: $K_\theta = T_x/\theta$.

From the torsion beam theory, we can write the elastic line equation:

$$\frac{d^2\theta}{dx^2} = \frac{1}{GJ_0} \frac{dT_x}{dx} \quad (4.20)$$

J_0 is a constant depending on the section of the beam. For rectangular beam with $t > w$:

$$J_0 = \frac{1}{3} t \cdot W_s^3 \left[1 - 192 \frac{W_s}{t \cdot \pi^5} \left(\sum_{n=1,3,\dots}^{\infty} \frac{1}{n^5} \tanh \left(\frac{\pi \cdot t \cdot n}{2 \cdot W_s} \right) \right) \right] \quad (4.21)$$

G is the shear modulus and it is equal to

$$G = \frac{E}{2 \cdot (1 + \nu)} \quad (4.22)$$

In this case T_x is constant in all the section of the beam, so:

$$\frac{d\theta}{dx} = \frac{T_x}{GJ_0} \quad (4.23)$$

By integrating this equation on the beam with condition $\theta_{x=0} = 0$, the following relation is obtained:

$$\theta = \frac{L_s}{GJ_0} T_x \quad (4.24)$$

Then the expression for the elastic torsional constant is:

$$k_\theta = \frac{T_x}{\theta} = \frac{GJ_0}{L_s} \quad (4.25)$$

Considering that there are two springs, the total torsional elastic constants for the considered mirror is:

$$K_\theta = 2k_\theta = 2 \frac{GJ_0}{L_s} \quad (4.26)$$

Substituting in eq. (4.19), an expression which relates angle and voltage is deduced (under the hypothesis that the bending of the mirror caused by the applied force F_E is negligible).

$$V_0(\theta) = \sqrt{\frac{4GJ_0\theta^3}{\varepsilon_0 L_s L_m \left(\ln \left(\frac{h_0 - b \cdot \theta}{h_0 - a \cdot \theta} \right) + \frac{b \cdot \theta}{h_0 - b \cdot \theta} - \frac{a \cdot \theta}{h_0 - a \cdot \theta} \right)}} \quad (4.27)$$

It is possible to make a graph of this equation by varying, for example, the length the width of the hinges (Figure 4.4)

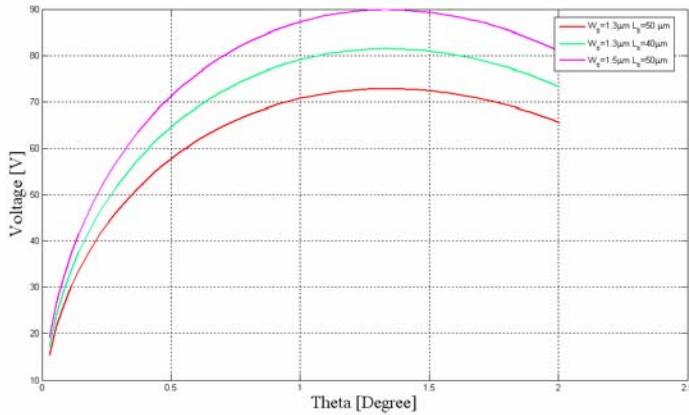


Figure 4.4: Three angle-voltage curve with different width and length of the hinges. Other parameter: $t=15\mu\text{m}$; $E=145\text{GPa}$; $\nu=0.3$; $L_m=500\mu\text{m}$; $W_m=40\mu\text{m}$; $a=2\mu\text{m}$; $b=15\mu\text{m}$; $h_0=1.6\mu\text{m}$.

At this point it should be interesting to verify the hypothesis of pure torsional model $h_0 = cost..$ If we call δ_{max} the maximum displacements of the central x-axis of the mirror of the mirror caused by F_E , to verify the hypothesis $\delta_{max} < h_0$. The mirror and the hinges are schematized as beams (Figure 4.5.a) with an applied load on the mirror. For more simplicity only an half of the mirror is considered (Figure 4.5.b).

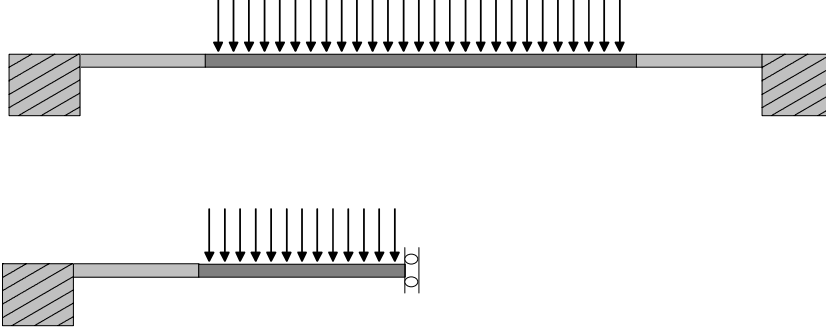


Figure 4.5: Schematization of the mirror and the hinges as beam(top); schematization of an half of the structure to simplify calculations (bottom).

The load for unit of length applied on the mirror is derived by equ. ##.

$$\sigma_E(\theta, V_0) = \frac{\varepsilon_0 V_0^2}{2\theta} \left(\frac{1}{h_0 - b \cdot \theta} - \frac{1}{h_0 - a\theta} \right) \quad (4.28)$$

The differential equation systems which has to be solved is:

$$\begin{cases} u_1^{IV}(x) = 0 \\ u_2^{IV}(x) = \frac{\sigma_E(\theta, V)}{EI_2} \end{cases} \quad (4.29)$$

The boundary conditions for this system are:

$$\begin{aligned} u_1(0) = u_1'(0) &= 0 && \text{clamp condition} \\ u_1(L_s) &= u_2(L_s) && \text{continuity of the displacement} \\ u_1'(L_s) &= u_2'(L_s) && \text{continuity of the first derivative} \\ I_1 u_1''(L_s) &= I_2 u_2''(L_s) && \text{continuity of the bending moment} \\ u_2'(L_s + L_m/2) &= 0 && \text{non rotation condition} \\ u_2'''(L_s + L_m/2) &= 0 && \text{shear moment null} \\ I_1 u_1'''(L_s) &= I_2 u_2'''(L_s) && \text{continuity of the shear moment} \end{aligned}$$

This systems can be solved, but we will not show all the mathematical steps:

$$\begin{aligned}
 u_2(x) = & -\frac{\sigma_E}{48 E I_1 I_2 (2 I_2 L_s + I_1 L_m)} \left\{ \left[-4 I_2^2 L_s^4 L_m \right. \right. \\
 & \left. - I_1^2 L_m (L_s - x)^2 (-2 L_s^2 + L_m^2 + 4 L_s x - 2 x^2) \right] \\
 & + I_1 I_2 L_s \left[4 L_s^4 + 4 L_s^3 (3 L_m - 4 x) - 2 L_m^3 x + 4 x^4 + \right. \\
 & \left. \left. 4 L_s^2 (L_m^2 - 6 L_m x + 6 x^2) + L_s (L_m^3 - 12 L_m^2 x + 12 L_s x^2 - 16 x^3) \right] \right\}
 \end{aligned}$$

(4.30)

The maximum vertical displacement is given by the value of the function $u_2(x)$ in $L_s + L_m/2$ which corresponds to the middle of the mirror.

$$\delta_z = \frac{\sigma_E L_m \left[32 I_2^2 L_s^4 + I_1 L_m^4 + 2 I_1 I_2 L_s L_m (32 L_s^2 + 16 L_s L_m + 3 L_s^2) \right]}{384 E I_1 I_2 (2 I_2 L_s + I_1 L_m)} \quad (4.31)$$

Hence by substituting the voltage obtained by relation (4.27) in (4.28), a set of curves which relates the maximum vertical displacement to the rotation angle is derived (Figure 4.6). By analyzing the obtained data, we can notice that the hypothesis $\delta_{max} \ll h_0$ is not verified for all the rotation angle. Hence the pure torsional model cannot be considered valid and the pull-in angle will be less than the calculated value in equ. (4.19) .

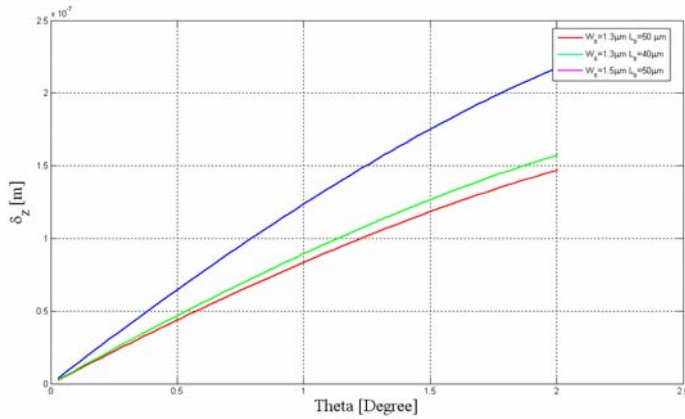


Figure 4.6: Three δ_z -voltage curve with different width and length of the hinges. Other parameter: $t=15 \mu\text{m}$; $E=145\text{GPa}$; $\nu=0.3$; $L_m=500 \mu\text{m}$; $W_m=40\mu\text{m}$; $a=2 \mu\text{m}$; $b=15\mu\text{m}$; $h_0=1.6\mu\text{m}$ which shows that the vertical displacement is not negligible.

4.4 Dynamic characterization: small-signal equivalent circuit

To deduce a small-signal equivalent circuit it is necessary to find the transfer function of the mirror, so we start from the motion equation:

$$I\ddot{\theta} + b\dot{\theta} + K\theta = \frac{1}{2} \frac{\partial C_m}{\partial \theta} V^2 \quad (4.32)$$

We suppose that the mirror is at equilibrium, that the rotation angle is θ_0 with an applied voltage V_0 and a charge $Q_0 = C_m(\theta_0) \cdot V_0$, so the following relation is verified:

$$K_0\theta_0 = \frac{1}{2} \frac{\partial C_m}{\partial \theta} \bigg|_{\theta=\theta_0} V_0^2 \quad (4.33)$$

The under analysis system is nonlinear, but we will linearize it by supposing a small variation of the voltage δV , which corresponds one of the angle $\delta\theta$ and one of the charge δQ . We want to calculate $c_m(s) = \delta Q(s)/\delta V(s)$ and to this we start from the expression of δQ :

$$Q = C_m(\theta)V \quad (4.34)$$

Then

$$\delta Q = \delta C_m V_0 + C_m(\theta_0) \delta V = \left[V_0 \frac{\delta C_m(\theta_0)}{\delta \theta} \frac{\delta \theta}{\delta V} + C_m(\theta_0) \right] \delta V \quad (4.35)$$

The expression of $\delta\theta/\delta V$ in the relation (4.35) is unknown. We can deduce it from (4.32).

$$I\delta\ddot{\theta} + b\delta\dot{\theta} + K_\theta(\delta\theta + \theta_0) = \frac{1}{2} \frac{\partial C_m}{\partial \theta} \bigg|_{\theta=\theta_0+\delta\theta} (V_0 + \delta V)^2 \quad (4.36)$$

As we want to linearize, we change the right term of (4.36) in:

$$\frac{1}{2} \frac{\partial C_m}{\partial \theta} \bigg|_{\theta=\theta_0} (V_0 + \delta V)^2 + \frac{1}{2} \frac{\partial^2 C_m}{\partial \theta^2} \bigg|_{\theta=\theta_0} \delta\theta (V_0 + \delta V)^2 \quad (4.37)$$

After expanding the two terms and neglecting the elements depending on δV^2 , we obtain:

$$\frac{1}{2} \frac{\partial C_m}{\partial \theta} \bigg|_{\theta=\theta_0} V_0^2 + \frac{\partial C_m}{\partial \theta} \bigg|_{\theta=\theta_0} V_0 \delta V + \frac{1}{2} \frac{\partial^2 C_m}{\partial \theta^2} \bigg|_{\theta=\theta_0} V_0^2 \delta\theta + \frac{\partial^2 C_m}{\partial \theta^2} \bigg|_{\theta=\theta_0} V_0 \delta V \delta\theta \quad (4.38)$$

By neglecting the last term with respect the second last and by verifying that the first term is equal to $K_0\theta_0$, the equation (4.36) becomes:

$$I\delta\ddot{\theta} + b\delta\dot{\theta} + \left[K_{\theta} - \frac{1}{2} \frac{\partial^2 C_m}{\partial \theta^2} \right]_{\theta=\theta_0} V_0^2 \delta\theta = \frac{\partial C_m}{\partial \theta} \bigg|_{\theta=\theta_0+\delta\theta} V_0 \delta V \quad (4.39)$$

Passing from the time domain to the the domain of the complex variable s by Laplace-transform:

$$\frac{\delta\theta(s)}{\delta V} = \frac{\partial C_m}{\partial \theta} \bigg|_{\theta=\theta_0} \frac{V_0}{Is^2 + bs + k - \frac{1}{2} \frac{\partial^2 C_m}{\partial \theta^2} \bigg|_{\theta=\theta_0} V_0^2} \quad (4.40)$$

At this point it is possible to write the expression for the small-signal transfer capacitance by combining (4.35) and (4.40):

$$c_m(s) = \frac{\delta Q(s)}{\delta V} = V_0 \frac{\partial C_m}{\partial \theta} \bigg|_{\theta=\theta_0} \frac{\delta\theta(s)}{\delta V} + C_m(\theta_0) \quad (4.41)$$

After carried out all the calculation, the following expressions is deduced:

$$c_m(s) = C_m(\theta_0) \frac{Is^2 + bs + K_{\theta} - \frac{1}{2} \frac{\partial^2 C_m}{\partial \theta^2} \bigg|_{\theta=\theta_0} V_0^2 + \frac{V_0^2}{C_m(\theta_0)} \left(\frac{\partial C_m}{\partial \theta} \bigg|_{\theta=\theta_0} \right)^2}{Is^2 + bs + K_{\theta} - \frac{1}{2} \frac{\partial^2 C_m}{\partial \theta^2} \bigg|_{\theta=\theta_0} V_0^2} \quad (4.42)$$

In the expression (4.42) we can use the equilibrium relation

$$K_{\theta} \theta_0 = \frac{1}{2} \frac{\partial C_m}{\partial \theta} \bigg|_{\theta=\theta_0} V_0^2$$

$$c_m(s) = C_m(\theta_0) \frac{Is^2 + bs + K_{\theta} \left[1 - \frac{\theta_0}{\frac{\partial C_m}{\partial \theta} \bigg|_{\theta=\theta_0}} \frac{\partial^2 C_m}{\partial \theta^2} \bigg|_{\theta=\theta_0} + \frac{2\theta_0}{C_m(\theta_0)} \frac{\partial C_m}{\partial \theta} \bigg|_{\theta=\theta_0} \right]}{Is^2 + bs + K_{\theta} \left[1 - \frac{\theta_0}{\frac{\partial C_m}{\partial \theta} \bigg|_{\theta=\theta_0}} \frac{\partial^2 C_m}{\partial \theta^2} \bigg|_{\theta=\theta_0} \right]} \quad (4.43)$$

Finally we can write (4.43) in Bode's form:

$$c_m(s) = C_m(\theta_0) \frac{s^2 + \frac{\omega_m}{Q_s}s + \omega_m^2 \left[1 - \frac{\theta_0}{\frac{\partial C_m}{\partial \theta} \Big|_{\theta=\theta_0}} \frac{\partial^2 C_m}{\partial \theta^2} \Big|_{\theta=\theta_0} + \frac{2\theta_0}{C_m(\theta_0)} \frac{\partial C_m}{\partial \theta} \Big|_{\theta=\theta_0} \right]}{s^2 + \frac{\omega_m}{Q_s}s + \omega_m^2 \left[1 - \frac{\theta_0}{\frac{\partial C_m}{\partial \theta} \Big|_{\theta=\theta_0}} \frac{\partial^2 C_m}{\partial \theta^2} \Big|_{\theta=\theta_0} \right]}$$

(4.44)

where $\omega_m = \sqrt{\frac{K_\theta}{I}}$, I is the pulsation of mechanical resonance and

$Q_s = \frac{\sqrt{K_\theta I}}{b}$ the quality factor. Probably from experiments we will measure the impedance of the mirror at different frequency, then from eq. (4.44) we deduce the following expression for it (by passing in the Fourier domain):

$$G(j\omega) = C_m(\theta_0) j\omega \frac{-\omega^2 + \frac{\omega_m}{Q_s}j\omega + \omega_m^2 \left[1 - \frac{\theta_0}{\frac{\partial C_m}{\partial \theta} \Big|_{\theta=\theta_0}} \frac{\partial^2 C_m}{\partial \theta^2} \Big|_{\theta=\theta_0} + \frac{2\theta_0}{C_m(\theta_0)} \frac{\partial C_m}{\partial \theta} \Big|_{\theta=\theta_0} \right]}{-\omega^2 + \frac{\omega_m}{Q_s}j\omega + \omega_m^2 \left[1 - \frac{\theta_0}{\frac{\partial C_m}{\partial \theta} \Big|_{\theta=\theta_0}} \frac{\partial^2 C_m}{\partial \theta^2} \Big|_{\theta=\theta_0} \right]}$$

(4.45)

In the equivalent circuit, we must included a parasitic capacitance in parallel to the mirror. This capacitance will always be present and will change the frequency response of the mirrors. In the equation (4.45) it has to be added to $C_m(\theta)$.

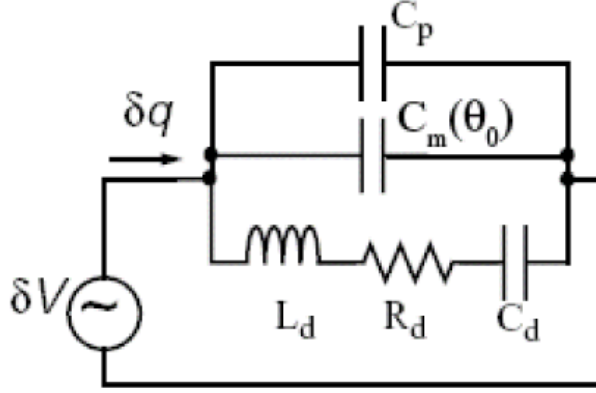


Figure 4.7: Small signal Equivalent circuit

$$Y_m(j\omega) = (C_m(\theta_0) + C_p)j\omega \frac{-\omega^2 + \frac{\omega_m}{Q_s}j\omega + \omega_m^2 \left[1 - \frac{\theta_0}{\frac{\partial C_m}{\partial \theta} \Big|_{\theta=\theta_0}} \frac{\partial^2 C_m}{\partial \theta^2} \Big|_{\theta=\theta_0} + \frac{2\theta_0}{C_m(\theta_0)} \frac{\partial C_m}{\partial \theta} \Big|_{\theta=\theta_0} \right]}{-\omega^2 + \frac{\omega_m}{Q_s}j\omega + \omega_m^2 \left[1 - \frac{\theta_0}{\frac{\partial C_m}{\partial \theta} \Big|_{\theta=\theta_0}} \frac{\partial^2 C_m}{\partial \theta^2} \Big|_{\theta=\theta_0} \right]} \quad (4.46)$$

From eq.(4.46) a small-signal equivalent circuit can be deduced (Figure 4.7), with the following components:

$$L_d = \frac{I}{2K_\theta \frac{\partial C_m}{\partial \theta} \Big|_{\theta=\theta_0} C_m(\theta_0)} \quad (4.47)$$

$$C_d = \frac{2\theta_0 C_m(\theta_0) \left(\frac{\partial C_m}{\partial \theta} \Big|_{\theta=\theta_0} \right)^2}{\frac{\partial C_m}{\partial \theta} \Big|_{\theta=\theta_0} - \frac{\partial^2 C_m}{\partial \theta^2} \Big|_{\theta=\theta_0} \theta_0} \quad (4.48)$$

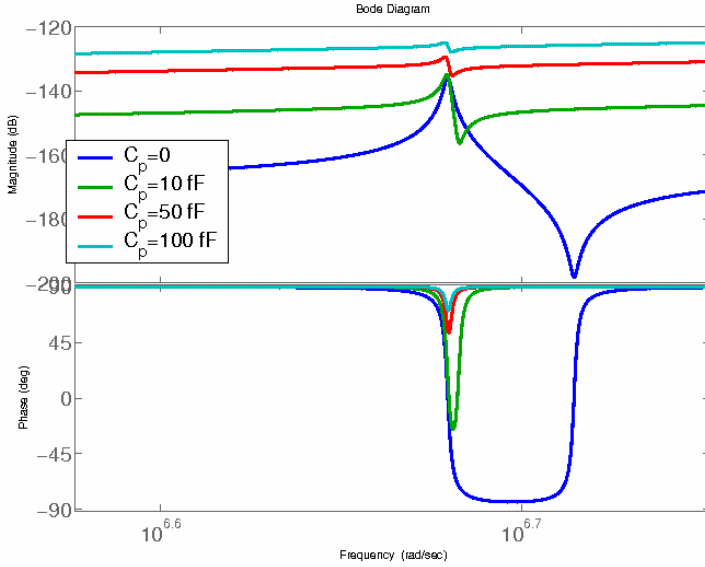


Figure 4.8: Examples of bode diagrams of a micromirrors with different parasitic capacitance.

$$R_d = \frac{2b\theta_0}{C_m(\theta_0)} \left. \frac{\partial C_m}{\partial \theta} \right|_{\theta=\theta_0} \quad (4.49)$$

If the parasitic capacitance is too high, in some cases it will be not possible to have measurements of the device. This problem can be verified in Figure 4.8 where the Bode diagrams of the admittance of a mirror at a given rotation angle with different parasitic capacitances are drawn.

The value of the parasitic capacitance also depends on the setup used to measure, hence it is difficult to predict a value for it.

4.5 Design Flow of the micromirrors arrays

In this subsection the complete design flow followed to realize arrays of micromirrors for optical switching in THELMA technology is presented. It has been constituted by two steps:

1. A preliminary test chip with some test structures to verify the optical performances of the micromirrors have been designed
2. Final test pattern where four arrays of micromirrors have been designed.

4.5.1 First test pattern: Not movable micromirrors

A preliminary test pattern with test structures has been designed and fabricated by using *THELMA* technology by *STMicroelectronics*.

This die contains 9 “venetian blind” micromirrors of size $400 \times 400 \mu\text{m}$, different for width of the single element of the micromirror, number of elements and holes density.

These micromirrors have not been released because holes density in some cases was very low so conventional sacrificial oxide etching did not allow complete oxide removal. On the top of some micromirrors, gold or aluminium have been deposited.

The Optoelectronic Group at University of Pavia have measured these structures. On the micromirrors without metallization, optical measurements by using HeNe laser emitting at $\lambda = 633 \text{ nm}$ have been carried out. By using a digital camera the diffraction patterns have been obtained with 45° degree tilt angle.

Moreover reflectivity measurements have been carried out. On the metallized structures a DFB laser emitting at $\lambda = 1550 \text{ nm}$ (typical for optical communications) have been used

Similar value of reflectivity have been found for both kinds of metallization, hence aluminium have been chosen as reflecting layer because of its easy deposition and better adhesion to silicon.

The comparison between diffraction patterns obtained by this not movable structures show that an high holes density produces larger scattering of the optical power, so larger loss.

Moreover larger elements of the *venetian blind* produce closer diffraction orders, hence the optical power commutation from one order to the next one requires smaller tilt angle.

4.5.2 Final test Pattern: description of the designed array

Long longitudinal holes in the mirror are required for proper release of the moving parts (**Errore. L'origine riferimento non è stata trovata.**). This can be done without excessive degradation of the optical characteristics. The Venetian blind is constituted by a variable number of micromirrors depending on the size, each suspended by two torsional springs. The springs are $50 \mu\text{m}$ long; the full micromirror arrays are about $490 \mu\text{m} \times 490 \mu\text{m}$ in size.

The main problem which has been already identified of using *THELMA* technology is constituted by the low full/empty ratio of the elements which constitutes the venetian blind, due to the rule on the maximum width of the poly which can be released.

To improve this aspect, an increase of sacrificial oxide etching time has been requested: the value of $10\ \mu\text{m}$ is reached.

It has been verified that the size of the electrode of poly1 is relevant on the micromirrors angular dynamics. This width should be low so values of $10\text{--}15\ \mu\text{m}$ are required. This is in contrast with the process rule which prescribe a minimum width of $40\ \mu\text{m}$ in order to avoid etching of the oxide under the electrode, fabricated in the first polysilicon layer and used for actuation. Hence their width was chosen non-uniform as a compromise between angular dynamics (which is reduced by pull-in for wider electrodes and technological constraints which required a specific minimum width(Figure 4.9)).

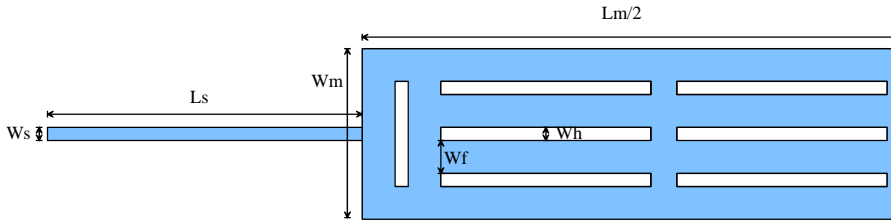


Figure 4.9: Scheme of an half of micromirror with longitudinal etch holes.

On the basis of the preceding considerations a die with 4 micromirrors arrays has been designed (Figure 4.11):

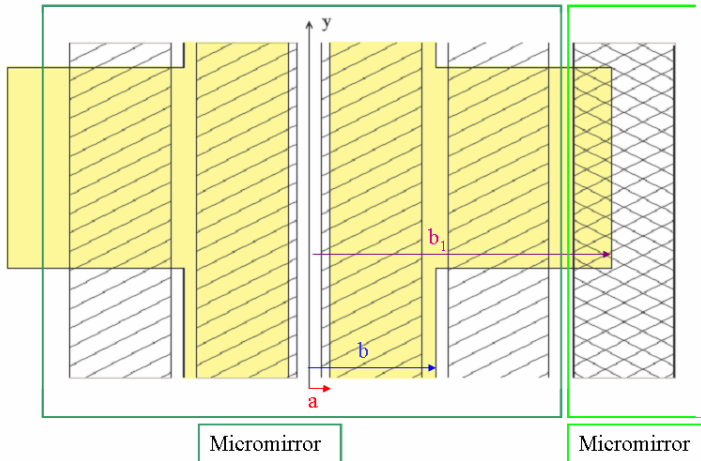


Figure 4.10: Particular of the underlying electrodes.

- A. Array constituted by micromirrors with $Wf=8\ \mu\text{m}$ and holes width $Wh=2\ \mu\text{m}$.

- B. Array constituted by micromirrors with $Wf = 10 \mu m$ and holes width $Wh = 2 \mu m$.
- C. Array constituted by micromirrors with $Wf = 10 \mu m$ and holes width $Wh = 3 \mu m$.
- D. Array constituted by micromirrors with $Wf = 12 \mu m$ and holes width $Wh = 3 \mu m$.

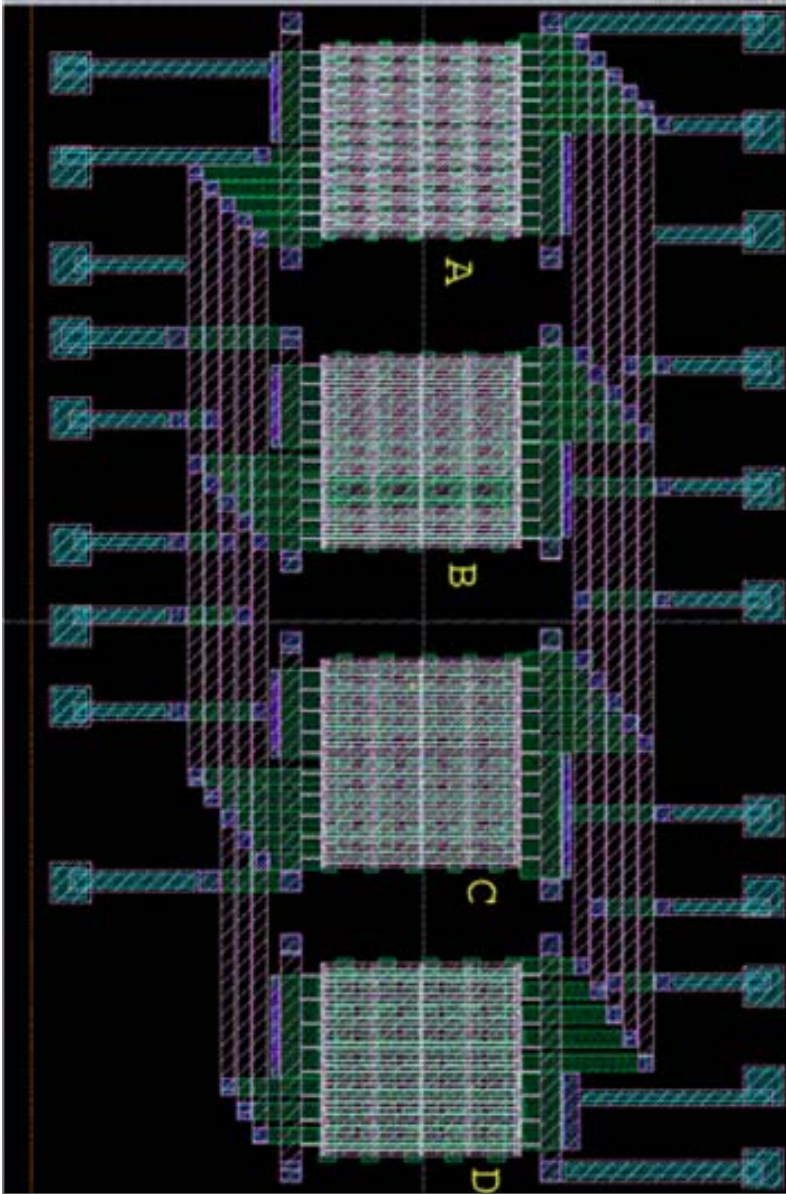
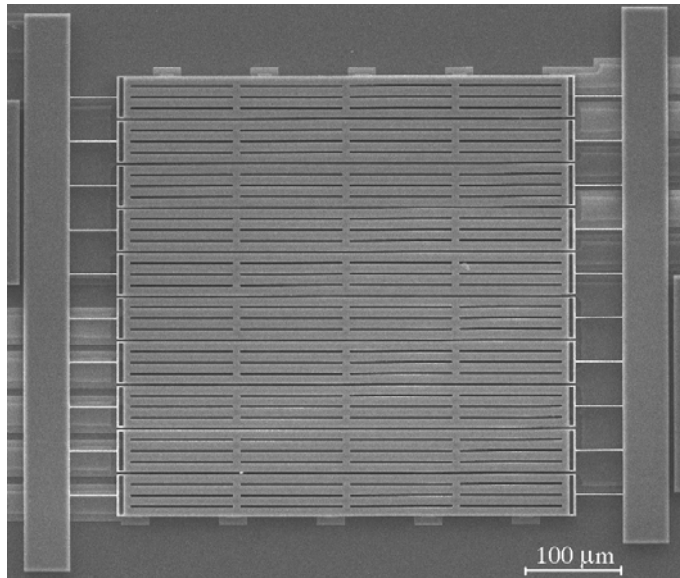


Figure 4.11: Layout of the final die containing 4 venetian blind micromirrors.

Table 4.1: Geometrical and electromechanical characteristic of the designed micromirrors.

	Micromirrors			
Parameter	A	B	C	D
L_s [μm]	50	50	50	50
W_s [μm]	1.3	1.3	1.3	1.3
L_m [μm]	490	490	490	490
W_m [μm]	38	46	49	57
a [μm]	2	2	2	2
b [μm]	12	12	12	12
b_1 [μm]				
W_f (μm)	8	10	10	12
W_h [μm]	2	2	3	3
θ pull-in [degree]	2	1.77	1.72	1.45
V pull-in [V]	73	63	58.7	50
F_1 (KHz)	59.7	53.2	53	48.2
F_2 (KHz)	94.5	71.5	66.5	52.8
F_3 (KHz)	115.3	102.7	101.8	92.5
F_4 (KHz)	187.1	180.3	179.7	173.3

**Figure 4.12: SEM Micrograph of designed micromirrors**

4.6 Modal Analysis by FEM simulations

In general to better understand the dynamic behavior of the micromirrors, it is important to know which is the mechanical resonance frequencies of them. We performed a FEM modal analysis by using COMSOL[®] of the micromirrors and the results that we obtained are listed in the Table 3.1, while the the shapes of the this first six resonance modes of the micromirrors are plotted in Figure 4.27.

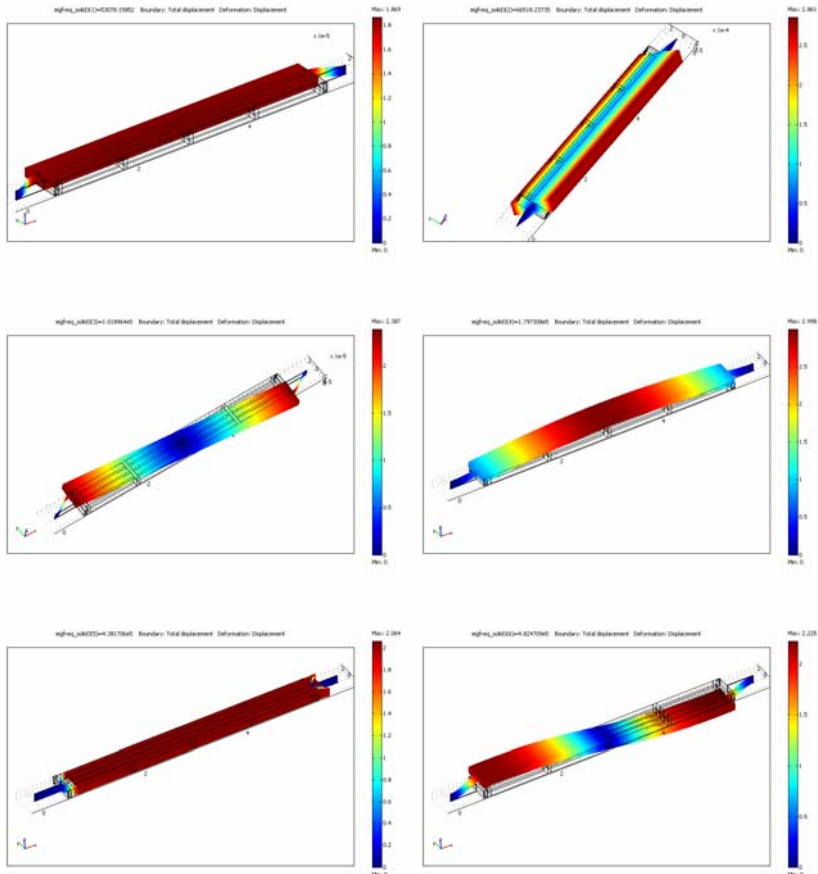


Figure 4.13: First six Mode Shapes of the micromirrors.

4.7 Reduced-Order Modelling of the bending of an array of torsional micromirrors

FEM Full coupled-field analysis of such structures is CPU-intensive and limited by convergence problems. Analytical prediction of the voltage/tilt relationship for such structures is therefore of great aid to the designer. Common simplifying assumptions to make the problem tractable are supposing a rigid vertical translation [69-71] or neglecting vertical present here a self-consistent, computationally fast approach to the problem, which also takes into account the vertical deflection and bending of the mirror strip, allowing the calculation of its deformed shape. The obtained results are then compared with FEM simulations.

Finally the applicability of the method to micromirrors of different size is exploited.

4.7.1 Computational approach

If a voltage V is applied between the mirror and one of the underlying electrodes, the distributed electrostatic force yields a torque which rotates the mirror, but also produces a deformation as the structure bends under the load. For ease of description, we suppose here a constant width electrode (Figure 4.14), even if the actual computation was performed with the variable width geometry. Let x be the coordinate along the mirror (Figure 4.14), $w(x)$ the electrostatic force per unit length and $u_z(x)$ the vertical displacement of the central axis of the mirror. The capacitance c_m per unit length between the mirror and the electrode can be written by using a parallel-plate approximation, and is a function of the tilt angle θ and of z .

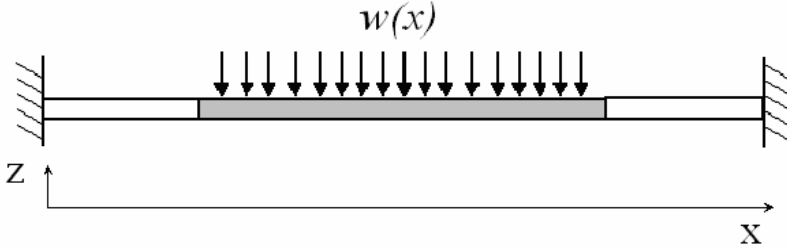


Figure 4.14: Transversal section of a micromirror

Our approach is based on the hypothesis that, for small bending, the distributed load $w(x)$ can be considered equivalent to a uniform load w_{eq} . This is clearly much less stringent than supposing a uniform u_z .

Elementary beam theory gives a closed expression (a polynomial in x) for $u_z(x; w_{eq})$ under a uniform load. Hence, a closed expression for the capacitance $c_m(\theta, z(w_{eq}))$ exists.

To compute the angle-voltage curve the following algorithm is used:

1. Choose rotation angle θ
2. At the first step impose $w_{eq,0}=0$
3. At each step i , calculate $V_i(\theta)$ from the static torsional equilibrium equation:

$$\frac{V_i^2}{2} \int_{mirror} \frac{\partial c_m(\varphi, z(w))}{\partial \varphi} \bigg|_{\substack{\varphi=\theta \\ w=w_{eq,i}}} dx = k_\theta \cdot \theta \quad (4.50)$$

4. Compute the equivalent distributed load $w_{eq,i+1}$ from:

$$w_{eq,i+1} \cdot L_m = \frac{V_i^2(\theta_0)}{2} \int_{L_m} \frac{\partial c_m(\varphi, z(w))}{\partial z} \bigg|_{\substack{\varphi=\theta \\ w=w_{eq,i}}} dx \quad (4.51)$$

5. Go to step 3 until $|w_{eq,i+1}-w_{eq,i}|$ is less than the chosen tolerance.

In eq. (1) k_θ is the elastic torsional constant of the springs[73]:

$$k_\theta = 2 \frac{GJ_p}{L_s} \quad (4.52)$$

G is the shear modulus of the polysilicon, L_s is the spring length, J_p is the torsion constant of the rectangular cross-section [10]:

$$J_p = \frac{1}{3} t W_s^3 \left(1 - 192 \frac{t}{W_s \pi^5} \sum_{i=1,3,5}^{\infty} \left(\frac{1}{i^5} \tanh \left(\frac{\pi W_s i}{2t} \right) \right) \right) \quad (4.53)$$

The expression of the first derivatives of the capacitance can be analytically derived from the parallel-plate formula, giving:

$$\frac{\partial c_m(\theta, z)}{\partial \theta} \bigg| = \frac{\varepsilon_0}{\theta^2} \left(\ln \left(\frac{h-b\theta}{h-a\theta} \right) + \frac{h}{h-b\theta} - \frac{h}{h-a\theta} \right) \quad (4.54)$$

$$\frac{\partial c_m(\theta, z)}{\partial z} \bigg| = \frac{\varepsilon(b-a)}{(h-b\theta-z)(h-a\theta-z)} \quad (4.55)$$

The closed expression for $u_z(x; w_{eq})$ under a uniform load is obtained by solving the classic Euler beam equation system with the appropriate boundary conditions[73]:

$$\begin{cases} \frac{\partial^4 u_z(x)}{\partial x^4} = 0 & x \in \text{springs} \\ \frac{\partial^4 u_z(x)}{\partial x^4} = \frac{w_{eq}}{EI_2} & x \in \text{mirror} \end{cases} \quad (4.56)$$

where E is the Young's Modulus of polysilicon and I_2 is the moment of inertia of the mirror section. An implicit assumption of our mechanical model is that every section rotates rigidly around the x axis. This is certainly reasonable if the mirror width is much smaller than its length.

The algorithm returns, for each θ , the value of the voltage $V(\theta)$ and the equivalent uniform distributed load $w_{eq}(\theta)$. From these values the vertical deformation $u_z(x)$ is deduced.

4.7.2 Results and Discussion

The computed $\theta(V)$ is shown in Figure 4.15. In Figure 4.16, the maximum vertical displacement $u_{z,max}$ (in the central section of the micromirror) is also plotted (bottom). The computation of the full curves requires less than 3 seconds on a PC.

For comparison, the rigid mirror model [69-70] and a full FEM analysis have been performed, and the obtained results are shown in Figure 4.15 and in Figure 4.16 as well. The selected FEM approach (Figure 4.17) (the “essolv” ANSYS® macro) required 30 minutes or more for each point in the $\theta(V)$ curve on the same PC.

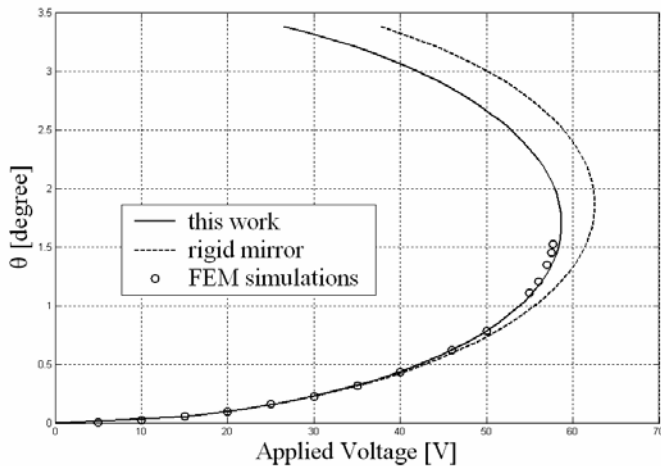


Figure 4.15: Angular rotation vs. applied voltage of one of the designed micromirrors.

The proposed approach clearly represents a large improvement with respect to the commonly reduced-order models, with a similar computational burden, but also shows a very good agreement with FEM results. This last result, however, depends on a few assumptions, which are easily verified for the studied geometry, but can fail in more general cases.

Specifically, a first important condition is that the bending of the beam is small enough to ensure that the distributed electrostatic force along the beam can be approximated with the equivalent uniform load. As the electrostatic force is a non-linear function of the distance between the beam and the fixed electrode, it is required the maximum deflection of the beam (i.e. at its center) is much smaller than the gap between it and the fixed electrode. In our case, the maximum deflection is about $0.1 \mu\text{m}$ at pull-in (see Figure 4.16), while the gap is $1.6 \mu\text{m}$, so that this condition is certainly verified.

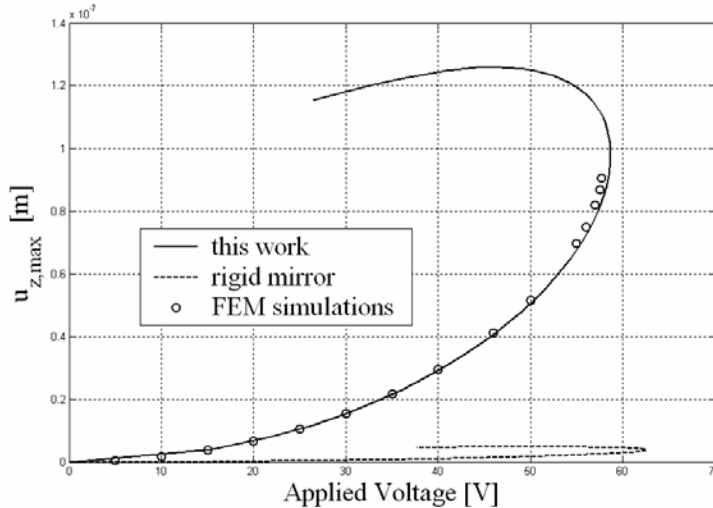


Figure 4.16: Maximum vertical displacement vs. applied voltage of one of the designed micromirrors.

A more compelling evidence that the uniform and non-uniform load can be considered equivalent is given in Figure 4.18. In the graph, the deformed shape of the central axis of the beam due to the distributed load (as calculated by ANSYS) and the same shape as computed by our method are compared. Three different deflected shapes, for 30, 40, and 50 V of bias (corresponding to rotation of 0.23, 0.44 and 0.78

degrees, respectively) are shown. The error is less than 2% in the worst case.

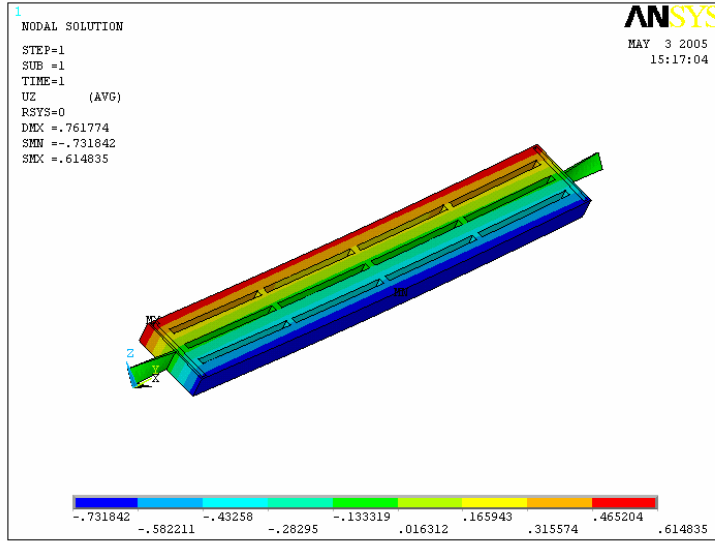


Figure 4.17: Example of the deformed shape obtained from ANSYS simulations

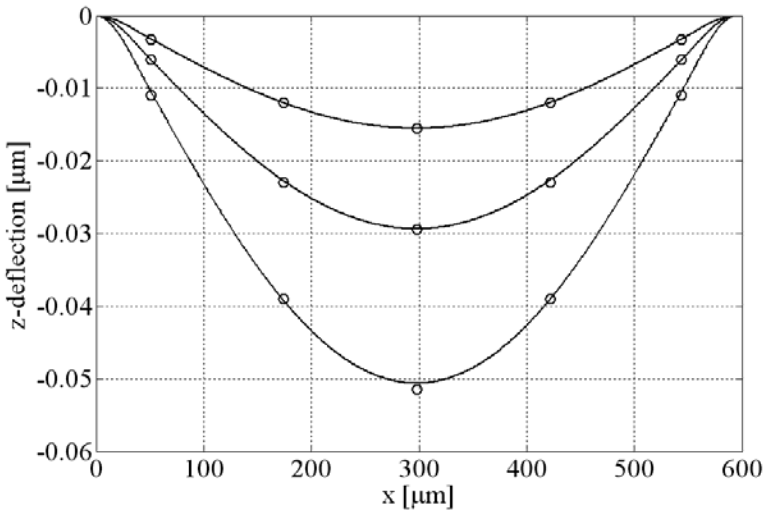


Figure 4.18: Comparison between the deformed shape of the central axis obtained from the analytical model (solid line) and from ANSYS simulations (circles).

Another already mentioned assumption is that every section of the mirror is not deformed (i.e. remains rectangular) under the applied load. In our case, the mirror is about 10 times longer than it is wide,

and thus has a much larger flexural rigidity along x than along y , so that this assumption looks reasonable.

4.8 Design of an driving circuit for micromirrors.

In order to drive the described micromirror, it is necessary the realization of a dedicated circuit. First of all, we introduce the specification which this driving circuit requires.

As we would like to study static and dynamic behaviour of the micromirrors, the output of the circuit must be composed by a constant voltage V_0 and varying signal v_{in}

From Table 4.1 we deduce that the constant voltage V_0 must be at least 70 V. In order to drive the micromirror at frequency larger than the first resonance mode, the bandwidth of the circuit should be at least 100 KHZ.

Hence these considerations produce the following specifications:

- 1) $V_0 > 70 \text{ V}$
- 2) $|v_o| < 1V$
- 3) $Bandwidth > 100KHz$
- 4) Low harmonic distortion

The schematic of the designed circuit is shown in Figure 4.19. The first stage sums the constant and varying input voltages (V_{in} and V_{ac}), then there is an amplifier stage.

On the output there is a BJT which allow to sustain high output voltage.

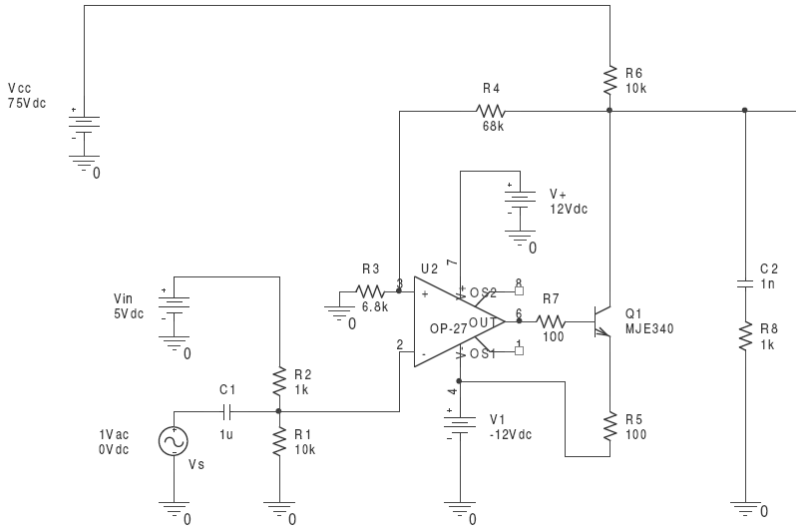


Figure 4.19: Schematic of the driving circuit for micromirror

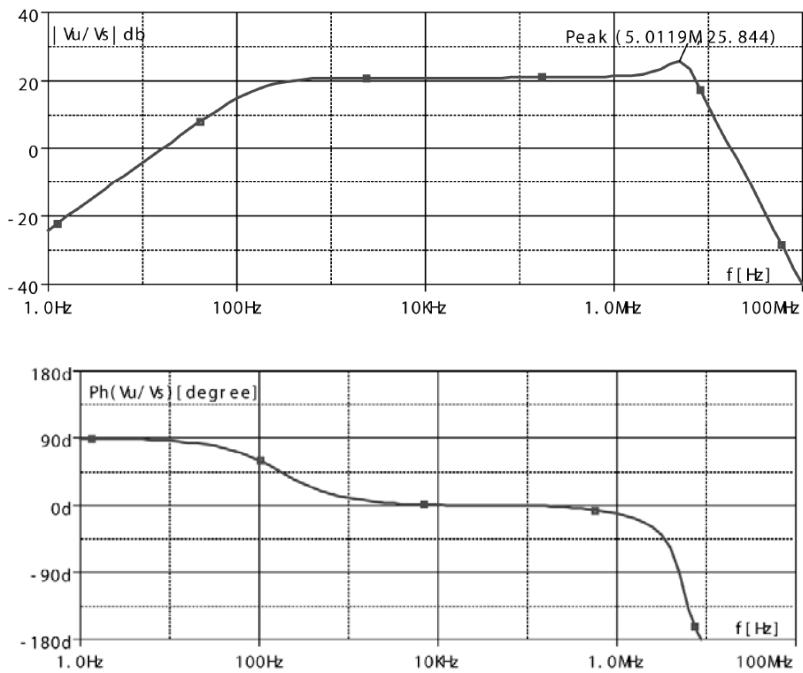


Figure 4.20: AC PSPICE simulations of the driving circuit for the micromirrors.

The total gain is 10 for the DC voltage. To make the circuit stable, on the output it is present a capacitor and resistor to compensate the circuit, to avoid oscillations.

In order to design and verify the specifications, AC PSPICE simulations have been carried out (Figure 4.20). The specifications on the bandwidth is satisfied: more than 5MHz. It is also been verified that V_o is linear till 70 V.

4.9 Experimental Results

4.9.1 Preliminary Static measurements

In order to verify the characteristic of the micromirrors, some static measurements have been carried out in the “Laboratorio Di Tecnologie e Microsistemi” at Department of Information Engineering of University of Pisa.

Using the described circuit to drive the micromirrors and the experimental setup in Figure 4.21, the curve in Figure 4.22 has been deduced for the micromirror C.

The obtained results are in good agreement with the expected behaviour.

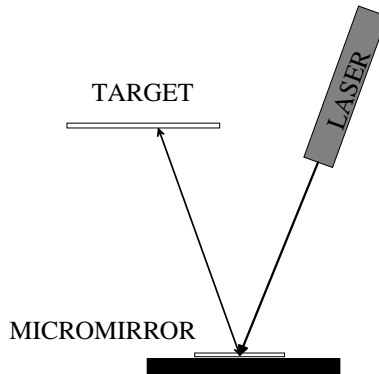


Figure 4.21: Scheme of the optical static measurements.

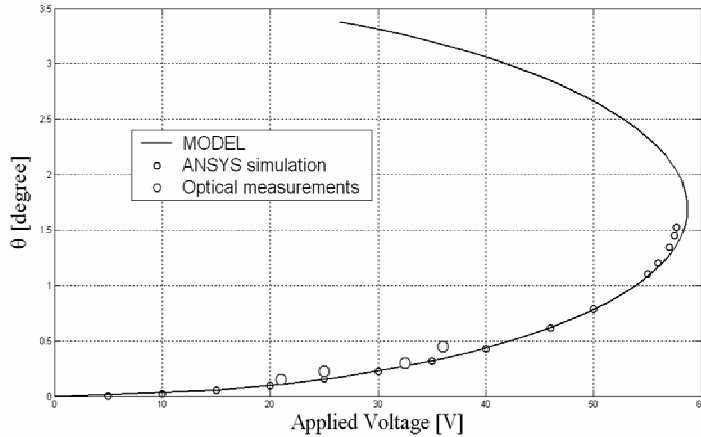


Figure 4.22: Static Optical measurements on micromirror C (Figure 4.11) compared to our model and ANSYS simulations.

4.9.2 Resonant mode measurements

The Optoelectronics Group at University of Pavia have

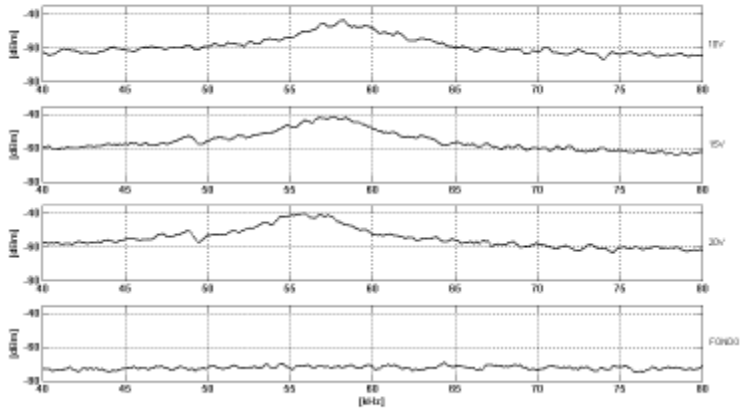
Table 4.2: Measured frequency resonances by Optoelectronic Group at University of Pavia.[75]

Micromirror	Mode	Measured [KHz]	Simulated [KHz]
A	Torsional f1	80-84	94.5
	Out of plane f4	180	187.5
B	Torsional f1	59-63	71.5
	Out of plane f4	175	180
C	Torsional f1	53-58	66.5
	Out of plane f4	171	179.7
D	Torsional f1	55	59.7
	Out of plane f3	109	115.3

developed an optical method to obtain vibration measurements by means of semiconductor laser feedback interferometry [74]. Hence they measured the described devices[75-76].

Using a setup in which the laser beam is shined orthogonally onto the device we can monitor the fundamental torsional mode and the out-of plane flexional mode, which are characterized by mass displacements with vertical components . If the optical radiation is impinging on the device at a small angle with respect to the substrate, vibrations in the horizontal plane can also be detected. The measurement can be performed using the interferometric scheme with the external optical-path in singlemode fiber or in free space. The

Torsional Mode f1



Out of plane mode f4

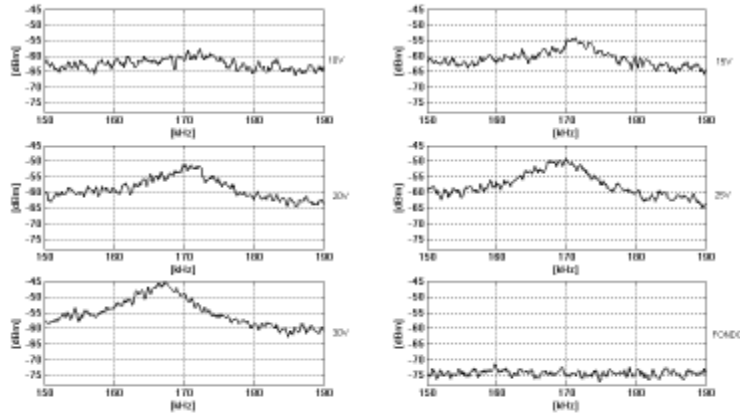


Figure 4.23: Experimental data on the spectral response of the torsional mode and the vertical flexional-mode on Micromirrors C[75]

dynamic response can be obtained by driving the device with electrical white noise superimposed to a dc voltage and by analyzing the photodetected signal with a spectrum analyzer[74].

In Table 4.4 the resonance modes measured for all the structures are reported compared to the simulated values. In Figure 4.23 the experimental data on the spectral response on micromirrors C are reported. A very good agreement has been found.

4.10 Test structures on Poly Silicon Germanium technology by IMEC

As already specified in Chapter 2, Poly-SiGe has recently been promoted as a material suitable as structural layer for several MEMS applications because of its low processing temperature, which enables post-processing on top of CMOS without introducing significant changes in the existing CMOS foundry processes.

In order to verify the possibility to realize micromirrors in Poly Si-Ge, a test chip with several test structures has been designed. Unfortunately we do not have experimental results on this test chip as it has to be fabricated.

In this subsection some of the structures designed in the layout in Figure 4.24 are briefly described. Specifically the structures in the box A, B and C will be described.

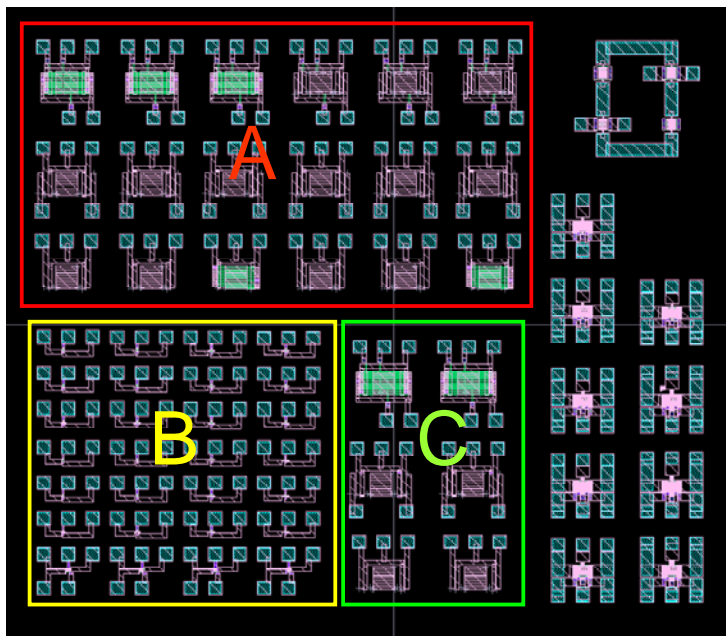


Figure 4.24: Layout of the complete die.

4.10.1 Structures A

The red box A (Figure 4.24) contains three kinds of structures which can be divided by rows: A.1x, A.2x, A.3x. These structures are characterized by the substitution of a single micromirror with an array of smaller phased micromirrors, a structure resembling a Venetian blind.

➤ **A.1x: array of micromirrors with electrodes divided in three parts**

These arrays are constituted by 10 micromirrors $200 \times 20 \mu\text{m}$, each of them can be driven by 6 electrodes, three for side (Figure 4.25). For each side, the two lateral electrodes are shorted as shown in Figure 4.26, where a cross section of a micromirror is drawn.

In previous analysis, it has been noticed that in a mirror with only two electrodes for side, by applying a voltage, the mirror rotates and there is a vertical deformation which reduces the maximum angular deflection before pull-in.

These structures have been designed with the idea of reducing the vertical deflection of the micromirrors. In fact by applying a lower voltage to the central electrode with respect to the voltage applied to the lateral electrodes, we expect that the vertical deflection of the centre of the micromirror will be lower with respect to the case where the electrode is along the whole mirror (structures A.3x).

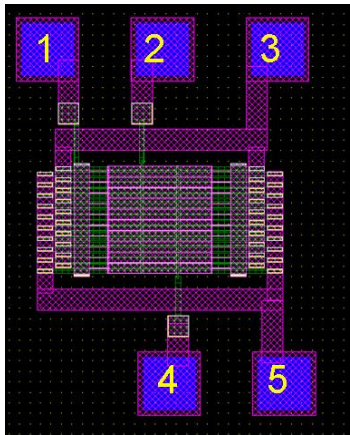


Figure 4.25: Layout of structures A.1x

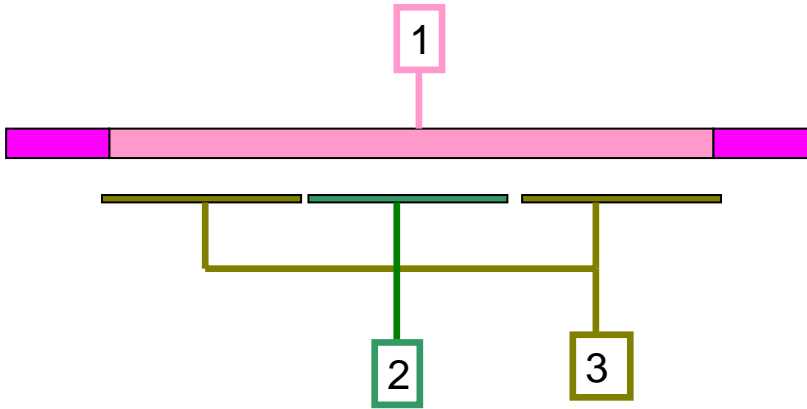


Figure 4.26: Cross section of a side of a micromirror.

This micromirror will be polarized by applying a voltage V_3 on the pad 3 and a voltage V_2 on the pad 2 while the mirror (pad 1) will be grounded. At the present we do not have a valid model to predict the behaviour of the micromirror but it will be soon available.

In Table 4.3 we report the mechanical resonance frequencies of the micromirrors of the structure A.11, while the mode shapes are reported in Figure 4.27.

Table 4.3: Mechanical resonance frequencies of micromirror A.11

Resonance frequencies	KHz
1st mode	45.619
2nd mode	92.330
3rd mode	99.894
4th mode	165
5th mode	4.76
6th mode	9.59

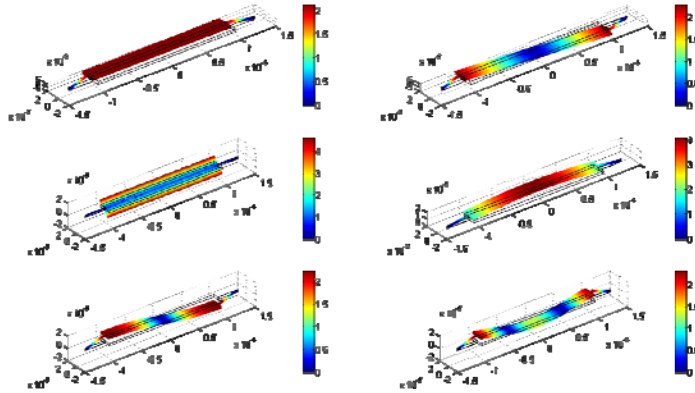


Figure 4.27: First six mode shape of a micromirror in the array A.11.

➤ **A.2x: array of micromirrors with four electrodes**

These arrays are constituted by 10 micromirrors $200 \times 20 \mu\text{m}$, each of them can be driven by 4 electrodes, two for side (Figure 4.28). In a previous analysis it has been noticed that the width of the electrodes reduces the maximum angular rotation before pull-in but also reduce the necessary voltage to reach a specified rotation.

These structures have been designed with by dividing in two the electrodes for each side of the mirrors (Figure 4.29). In this way by applying a different voltage to the more external electrode with respect to the more internal, we can obtain better performance whether in term of angular dynamic or in term of applied voltage.

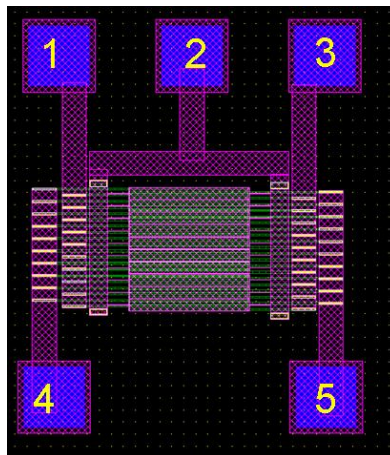


Figure 4.28: Layout of structures A.2x

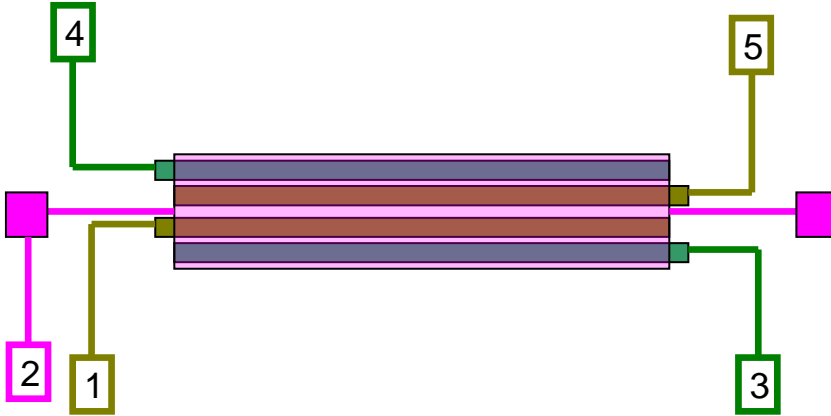


Figure 4.29: Schematic plant of a micromirror A.2x

We consider that the pad 2 is grounded and two different voltages V_1 and V_3 are applied on the pad 1 and on the pad 3 (In the same way the voltages can be applied on the pads 5 and 4). In Figure 4.30 and Figure 4.31 the expected angle versus voltage V_1 with different V_3 for the structure A.31 is plotted. Two characteristics are plotted because the thickness of the sacrificial oxide (which represent the distance between the underneath electrodes and mirror) can be $0.4\ \mu\text{m}$ or $1\ \mu\text{m}$. The mechanical resonance frequencies of the structures A.21 are the same as A.11.

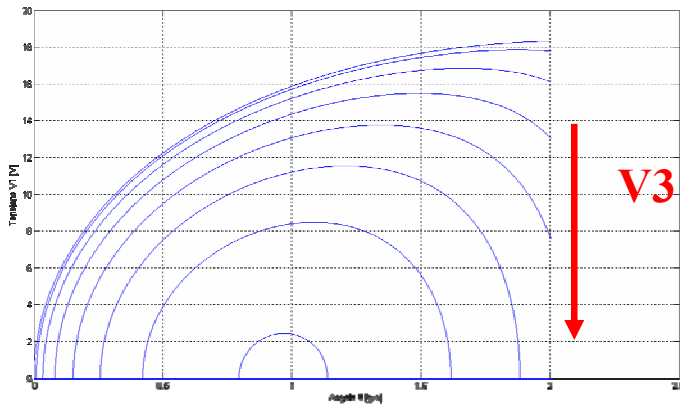


Figure 4.30: Voltage V_1 vs Angle if the thickness of the sacrificial layer is $0.4\ \mu\text{m}$.

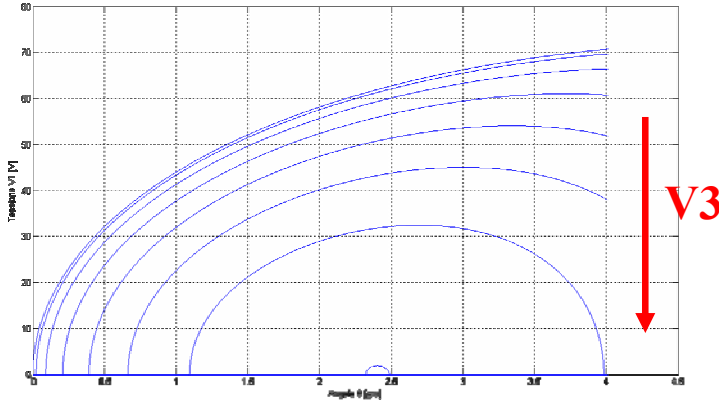


Figure 4.31: Voltage V1 vs Angle if the thickness of the sacrificial layer is $0.4 \mu\text{m}$

➤ **A.3x: array of micromirrors with two electrodes**

These arrays are constituted by 10 micromirrors $200 \times 20 \mu\text{m}$, each of them can be driven by 2 electrodes, one for side (Figure 4.32). The micromirrors are contacted by pad 2, while the electrodes are contacted by pads 1 and 3. These are the simplest structures and they have been designed in order to compare the performance of them with the other two variation (A.1x -A.2x)

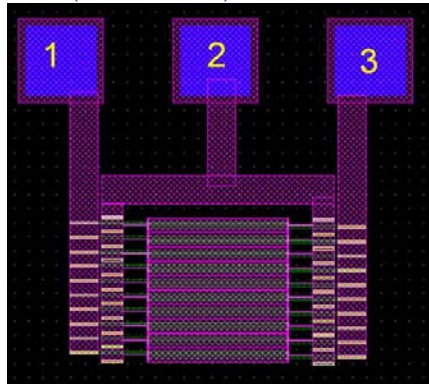


Figure 4.32: Layout of structures A.3x

We consider that the pad 2 is grounded and a voltage V is applied on the pad 1 (or on the pad 3). In Figure 4.33 and Figure 4.34 the expected angle-voltage characteristic for the structure A.31 is plotted. The mechanical resonance frequencies of the structures A.31 are the same as A.11.

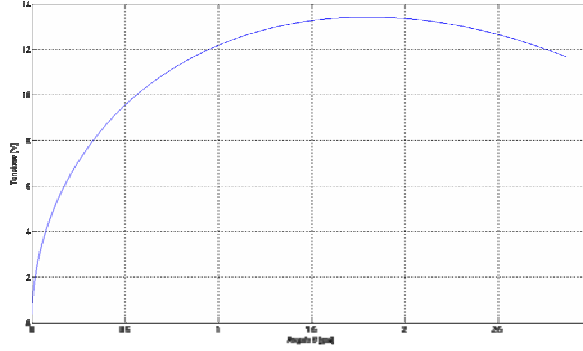


Figure 4.33: Angle-Voltage characteristic if the thickness of the sacrificial layer is $0.4 \mu\text{m}$

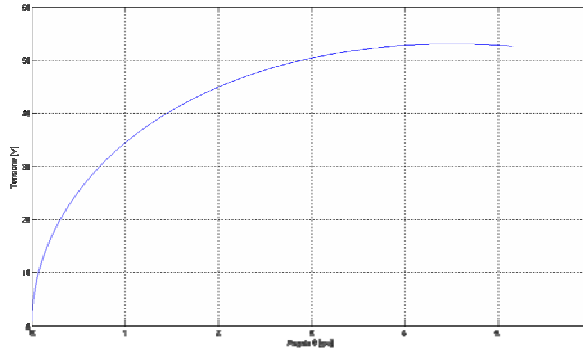


Figure 4.34: Angle-Voltage characteristic if the thickness of the sacrificial layer is $1 \mu\text{m}$

4.10.2 Structures B

The structures B are schematized as a 7×4 matrix of single micromirrors. All the mirrors we will analyze have the structure described in Figure 4.35. The dimension of the mirrors are $2L \times 2L \times t$, the hinges are $l_h \times w \times t$.

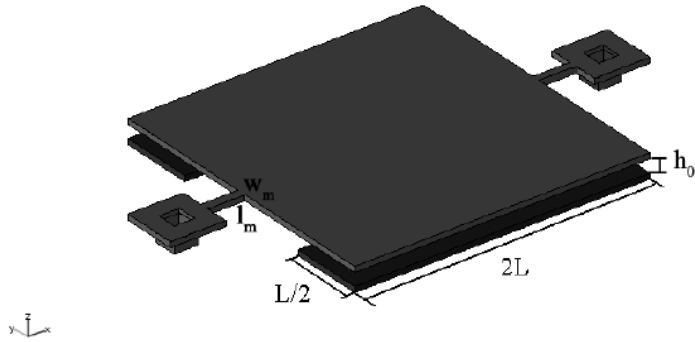


Figure 4.35: Scheme of a micromirrors for DLP.

Some of the mirrors had been designed with serpentine springs, but during a revision of the layout, some mistakes were found so the structures with serpentine springs cannot be measured. The micromirrors of the first three rows have $L=20\ \mu\text{m}$, those of the rows 3-6 have $L=16\ \mu\text{m}$. For all of them different size of hinges were designed (Figure 4.36).

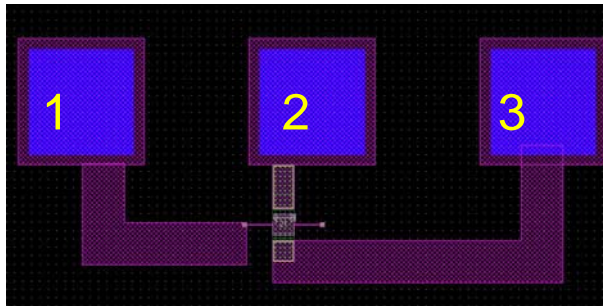


Figure 4.36: Layout of the structures B.xy.

In Figure 4.37 the expected angle-voltage characteristic for the structure B.14 is plotted.

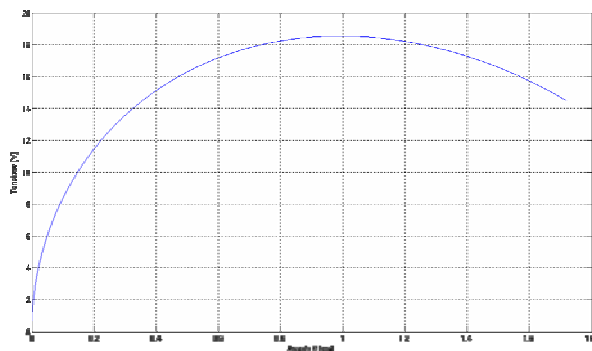


Figure 4.37: Angle-Voltage characteristic if the thickness of the sacrificial layer is $0.4 \mu\text{m}$

In the Table 4.4 we report the mechanical resonance frequencies of the micromirrors of the structure B.14. The mode shapes associated to this frequencies are reported in Figure 4.38. All the others are reported in the design_mirror.xls.

Table 4.4: First six modes frequencies of structure B.14

Resonance frequencies	KHz
1st mode	236
2nd mode	377
3rd mode	666
4th mode	1420
5th mode	5430
6th mode	5690

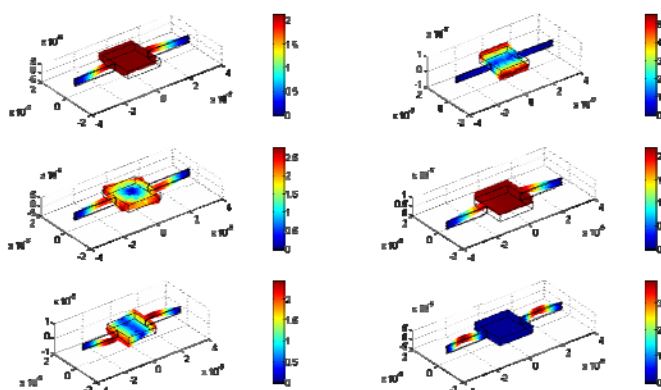


Figure 4.38: First six mode shape of the structure B.14.

4.10.3 Structures C

The green box A (Figure 4.24) contains three kinds of structures which can be divided by rows: C.1x, C.2x, C.3x. These structures are characterized by the substitution of a single micromirror with an array of smaller phased micromirrors, a structure resembling a Venetian blind.

➤ **C.1x: array of micromirrors with electrodes divided in three parts**

These micromirrors are similar to the A.1x.

➤ **C.2x: array of micromirrors with four electrodes**

These micromirrors are similar to the A.2x.

➤ **C.3x: array of micromirrors with two electrodes**

These micromirrors are similar to the A.1x.

Chapter 5

MEMS Flexure Design

5.1 Introduction

Among the most important steps in the development of a new MEMS device is the design of each element of the involved mechanical structures through tools that allow rapid prototyping and optimization of the relevant design parameters (e. g. stiffness, occupation of area, forces, capacitances, etc.). To this purpose, the value for the designer of analytical expressions for the physical features of the structures, which allow optimization of the parameters before simulation, should not be underestimated.

Springs are among the most important elements in MEMS devices. Several different kinds of springs were presented in the literature [76], any of them with advantages and drawbacks for a particular application. An interesting case is constituted by serpentine springs, getting their name from the meandering snake-like pattern of the spring segment[76]. They are used in several applications: accelerometers, resonators, etc. Although they are more commonly used to perform in-plane displacements, they can also be used for out-of-plane displacements, and angular deflections (i. e. as torsional springs) as well [6, 40, 50, 77-79], where they allow small spring constants with a reasonable occupation of area.

The main feature of several surface MEMS processes (see Chapter 3), is the presence of a thick structural polysilicon layer; for this kind of processes the classic torsional spring, made as a simple

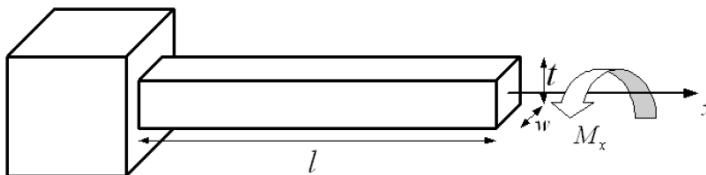


Figure 5.1: Torsion Bar.

straight bar and shown in Figure 5.1, does not allow for low torsional spring constants, because of the thickness of the structural layer. A possible solution is the use of serpentine springs.

This kind of springs, apart from reducing the occupied area for the same spring constant, has the advantage of solving the problem of the buckling produced by the residual stress [76]. It was also shown that using serpentine torsional springs the resonance frequencies are completely independent of the residual stress value, while there is a large dependence for simple straight torsional rods with similar torsional spring constants [79].

The shape of this kind of spring is shown in Figure 5.2.a. The reduction of the torsional stiffness is mainly due to the elements orthogonal to the torsional axis, which are subject to a bending stress. Unfortunately, as the thickness of the structural layer increases, the bending stiffness of the orthogonal elements, which is proportional to

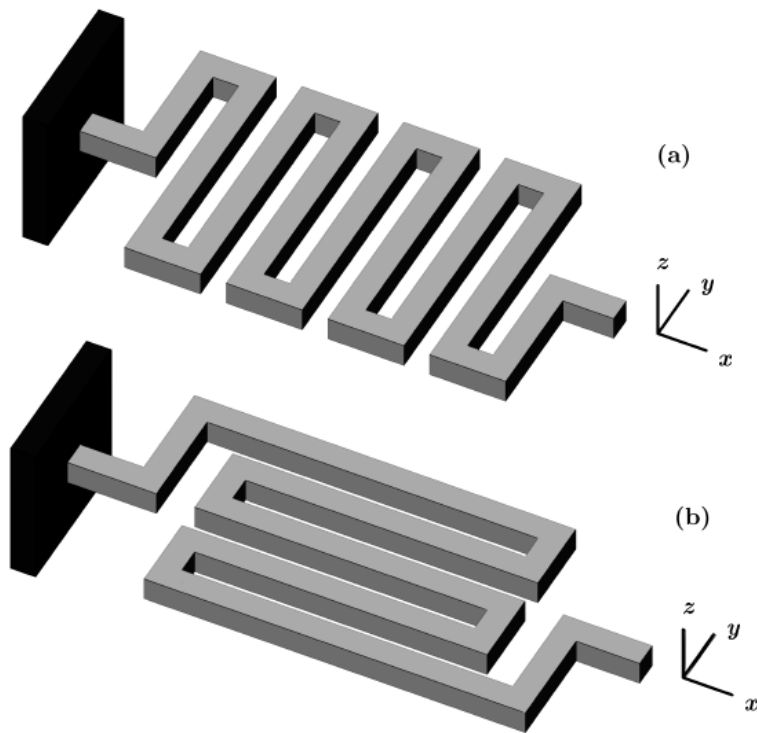


Figure 5.2: Classic serpentine spring (a); rotated serpentine spring (b).

the third power of the thickness [61], rapidly becomes so high that the advantage of this type of design is almost lost.

This problem can be overcome by a 90 degree rotation of the spring elements around the vertical axis, obtaining the rotated serpentine spring (Figure 5.2.b)[80]. With this design, the spring elements (which are now parallel to the torsional axis) are mainly subject to torsional stress, which is approximately linearly dependent on the value of the thickness.

In this chapter we will convert these qualitative considerations into a quantitative analysis. To this scope, we will deduce analytical expressions for several elements of the stiffness matrix (as defined in [81]) of both spring kinds by using the principle of virtual work with the unit-load method [61]. The analytical results will be compared with those obtained with a Finite Element Method (FEM) commercial software package for structural analysis.

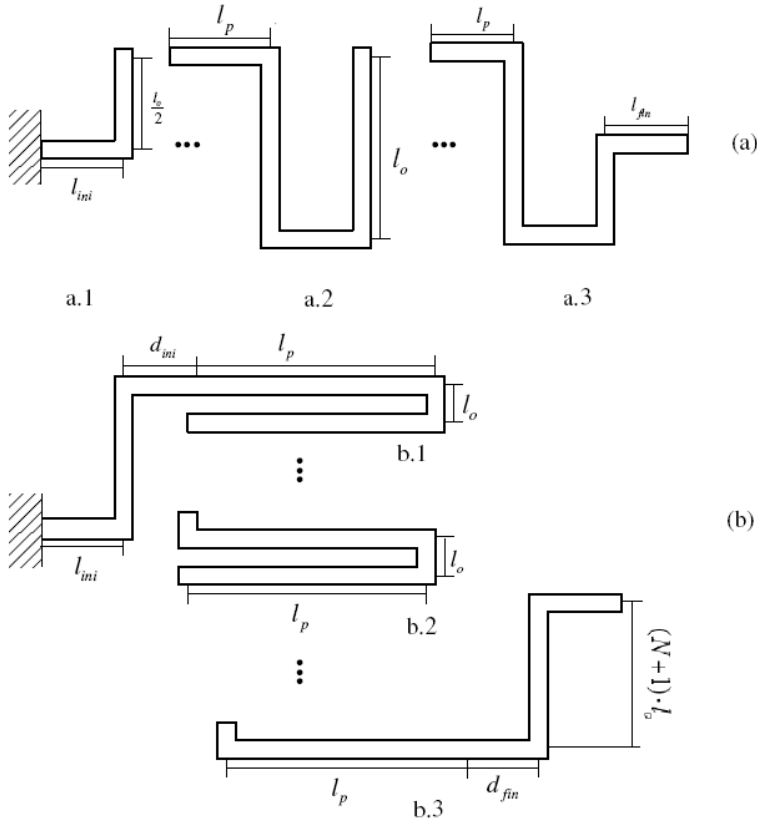


Figure 5.3: Design variables of serpentine springs. It is constituted by three parts: the initial (a.1 and b.1) and final parts (a.3 and b.3) used to connect it to the anchor and to the movable part (a.2 and b.2) which can be repeated.

5.2 Modeling and method of analysis

In order to characterize the springs we calculate the displacement Δ_i (or the rotation θ_i) resulting from a force F_j (or a torque M_j) applied in the appropriate direction, where $i, j \in \{x, y, z\}$. Only displacements from bending and torsion are considered in the analysis. Deformations from shear, compression and traction are neglected. Throughout the paper, the system of coordinates of Figure 5.2 will be used and the springs will be oriented so as to lie in the xy plane with the main axis parallel to x . The spring constant is defined as $K_{ij} = F_j / \delta_i$ (or $K_{\theta_i \theta_j} = M_j / \theta_i$). To simplify notation, if the two subscripts are identical, the second will be dropped. The resulting constants can be arranged in a 6×6 spring matrix:

$$K = \begin{pmatrix} K_x & K_{xy} & K_{xz} & K_{x\theta_x} & K_{x\theta_y} & K_{x\theta_z} \\ K_{yx} & K_y & K_{yz} & K_{y\theta_x} & K_{y\theta_y} & K_{y\theta_z} \\ K_{zx} & K_{zy} & K_z & K_{z\theta_x} & K_{z\theta_y} & K_{z\theta_z} \\ K_{\theta_x x} & K_{\theta_x y} & K_{\theta_x z} & K_{\theta_x \theta_x} & K_{\theta_x \theta_y} & K_{\theta_x \theta_z} \\ K_{\theta_y x} & K_{\theta_y y} & K_{\theta_y z} & K_{\theta_y \theta_x} & K_{\theta_y \theta_y} & K_{\theta_y \theta_z} \\ K_{\theta_z x} & K_{\theta_z y} & K_{\theta_z z} & K_{\theta_z \theta_x} & K_{\theta_z \theta_y} & K_{\theta_z \theta_z} \end{pmatrix}$$

This matrix is symmetric, that is has only 21 independent terms. The number of independent non-zero terms reduces to 12 assuming there are no variation in geometry along the z direction and therefore, no coupling between in-plane and out-of-plane directions [81]. The expressions for some of the elements of this matrix for serpentine springs were already presented [76, 81], but the problem of the torsional spring constant K_{θ_x} has not been completely analyzed. The elements of the spring constants matrix are calculated by using the principle of virtual work with the unit-load method, as detailed in Appendix 5.A. The two types of springs (serpentine and rotated serpentine) are parameterized as shown in Figure 5.3. The classic serpentine springs are divided into three parts (Figure 5.3).

Table 5.1: Nomenclature

Symbol	Definition
A	Beam or Spring cross-section [m^2]
E	Young's modulus [Pa]
F_i	F_i Force parallel to the i -axis [N]
G	Shear Modulus equal to $E/(2 \cdot (1 + \nu))$ [N]
I_{yo}	Moment of inertia with respect to the y -axis of the section of the element of the spring orthogonal to the x and z -axes [m^4]
I_{yp}	Moment of inertia with respect to the y -axis of the section of the element of the spring parallel to the x -axis [m^4]
I_{zo}	Moment of inertia with respect to the z -axis of the section of the spring element orthogonal to the x and z -axes [m^4]
I_{zp}	Moment of inertia with respect to the z -axis of the section of the spring element parallel to the x -axis [m^4]
$K_{\delta y}^C, K_{\delta y}^R$	Spring constant $F_y/\delta y$ with guided-end, for a classic and for a rotated serpentine spring, respectively [$N\ m^{-1}$]
$K_{\delta z}^C, K_{\delta z}^R$	Same as above for spring constant $F_z/\delta z$ with guided-end [$N\ m^{-1}$]
K_i	Spring constant $F_i/\delta i$ [$N\ m^{-1}$]
K_{ij}	Spring constant $F_j/\delta i$ [$N\ m^{-1}$]
$K_{i\theta j}$	Spring constant $M_j/\delta i$ [N]
$K_{\theta i}$	Spring constant $M_i/\theta i$ [N m]
$K_{\theta j i}$	Spring constant $F_j/\theta i$ [N]
$K_{\theta i\theta j}$	Spring constant $M_j/\theta i$ [N m]
K_x^C, K_x^R	Spring constant $F_x/\delta x$, for a classic and for a rotated serpentine spring, respectively [$N\ m^{-1}$]
K_y^C, K_y^R	Same as above for spring constant $F_y/\delta y$ [$N\ m^{-1}$]
K_z^C, K_z^R	Same as above for spring constant $F_z/\delta z$ [$N\ m^{-1}$]
$K_{z\theta y}^C, K_{z\theta y}^R$	Same as above for spring constant $M_y/\delta z$ [Nm]
$K_{\theta x}^C, K_{\theta x}^R$	Same as above for spring constant $M_x/\theta y$ [Nm]
$K_{\theta y}^C, K_{\theta y}^R$	Same as above for spring constant $M_y/\theta y$ [Nm]
$K_{\theta z y}^C, K_{\theta z y}^R$	Same as above for spring constant $F_y/\theta z$ [N]
$K_{\theta z}^C, K_{\theta z}^R$	Same as above for spring constant $M_z/\theta z$ [N m]
J_o	Cross-sectional torsion factor the spring element orthogonal to the x and z -axes [m^4]
J_p	Cross-sectional torsion factor of the spring element parallel to the x -axis [m^4]
l_o	Length of the spring element orthogonal to the x and z -axes [m]
l_p	Length of the spring element parallel to the x -axis [m]
M_i	Torsion moment or torque around i -axis [N m]
N	Number of foldings [-]
t	Thickness of the structural layer [m]
w_o	Width of the spring element orthogonal to the x and z -axes [m]
w_p	Width of the spring elements parallel to the x -axis [m]
ν	Poisson's ratio [-]

The first (a.1) and the third (a.3) are used to connect the spring to the anchor and to the movable mass and to make the architecture symmetric. The second part is constituted by N repeated elements of the type (a.2). The rotated serpentine springs are divided in a similar way (Errore. L'origine riferimento non è stata trovata.). In order to

simplify the calculation we suppose $l_{ini} = l_{fin} = l_p$ and $d_{ini} = d_{fin} = d_p$ in all our analyses.

We analyze the behaviour of the springs in the case of arbitrary N . Every spring is analyzed as the connection of several elementary beams, each one withstanding torsion and bending deformation. The length of each beam is measured along the central axis of the beam, between the centers of two consecutive corners (see Figure 5.3). We also suppose the joints are ideal, i.e. they transfer the forces and torques without significant deformation. This is an approximation that has to be taken into account when the results of the theoretical analysis are compared with the FEM simulations of the solid model.

5.3 Analytical expressions for the spring constants

Following the approach sketched in the preceding section, we computed analytical expressions for the most interesting spring constants of both classic and rotated serpentine, and in particular for those of interest in applications where a torsional spring is required. To allow a more straightforward analysis of the final expressions, the lengthy calculations required to derive such formulas were moved to Appendix 5.B. For all the following calculations the nomenclature listed in Table 5.1 is used. The spring constant of interest for use in torsional applications (as, for example, the ones in [40, 78]) is clearly $K_{\theta x} = Mx/\theta x$, i.e. the constant for a torsion along the axis of the spring. The expressions for $K_{\theta x}^C$ (for classic springs) and $K_{\theta x}^R$ (for rotated springs) are calculated in B.1 and are given as the first rows of Table 5.2 and Table 5.3, respectively. By analyzing the expression for $K_{\theta x}^C$ it is easy to recognize that the first term is contributed by the bending stiffness of the spring elements (of length l_o) orthogonal to the x axis, while the second term is contributed by the torsional stiffness of the elements (of length l_p) parallel to the same axis. A reasonable design approach to lower $K_{\theta x}^C$ with a given occupied area is to make l_p much smaller than l_o , so that the second term becomes negligible. With this hypothesis, the formula simplifies to a more manageable expression, also given in Table 5.2. A similar analysis can be carried out for $K_{\theta x}^R$. With rotated springs, the orthogonal elements are again subject to bending, and the parallel ones again withstand a torsion. The expression is complicated somewhat by the presence of the connecting elements (of length d_p , l_{ini} and l_{fin}) at the beginning and end of the spring. Nevertheless, the expression can be simplified, this

time by making the assumption that l_p is much bigger than l_o and than the lengths of the aforementioned connecting elements, obtaining a formula which is useful for a rough estimate of spring behaviour. Substituting the expressions of I_{y_o} and J_p given in (5.6) and (5.7), we can compare the different dependence on the thickness value of the two springs

Table 5.2: Calculated spring constants of a classic serpentine spring

Classic Serpentine Spring Constants	
$K_{\theta_x}^C = \left[\frac{2(N+1)}{EI_{y_o}} l_o + \frac{2(N+2)}{GJ_p} l_p \right]^{-1}$	
$K_{\theta_x}^C \approx \frac{EI_{y_o}}{2(N+1)l_o} \quad (\text{if } l_o \gg l_p)$	
$K_x^C = \left[\frac{(N+1)}{6EI_{z_o}} l_o^3 + \frac{(N+2)}{2EI_{z_p}} l_p^2 l_o \right]^{-1}$	
$K_x^C \approx \frac{6EI_{z_o}}{(N+1)l_o^3} \quad (\text{if } l_o \gg l_p)$	
$K_{\delta_y}^C = \frac{K_{y\theta_z}^C K_{\theta_z y}^C K_y^C}{K_{y\theta_z}^C K_{\theta_z y}^C - K_y^C K_{\theta_z}^C}$	
$K_{\delta_y}^C \approx \frac{3EI_{z_o} (N+1)}{(12N^4 + 64N^3 + 130N^2 + 116N + 38) l_p^2 l_o} \quad (\text{if } l_o \gg l_p)$	
$K_{\delta_z}^C = \frac{K_{z\theta_y}^C K_{\theta_y z}^C K_z^C}{K_{z\theta_y}^C K_{\theta_y z}^C - K_z^C K_{\theta_y}^C}$	
$K_{\delta_z}^C \approx \frac{6EI_{y_o} GJ_o}{(N+1)GJ_o l_o^3 + (16N^3 + 36N^2 + 43N + 3) EI_{y_o} l_p^2 l_o} \quad (\text{if } l_o \gg l_p)$	

Table 5.3: Calculated spring constants of a rotated serpentine spring

Rotated Serpentine Spring Constants	
$K_{\theta_x}^R = \left[\frac{4(N+1)}{EI_{y_o}} l_o + \frac{(2N+3)l_p + 2d_p + l_{ini} + l_{fin}}{GJ_p} \right]^{-1}$	
$K_{\theta_x}^R \approx \frac{GJ_p}{(2N+3)l_p} \quad (\text{if } l_p \gg l_o, l_{ini}, l_{fin}, d_p)$	
$K_x^R = \left[\frac{(4(N+1)l_o^3)^3}{3EI_{z_o}} + \frac{(2N^3 + 9N^2 + 13N + 6)l_p + 6(N+1)d_p}{3EI_{z_p}} l_o^2 \right]^{-1}$	
$K_x^R \approx \frac{3EI_{z_p}}{(2N^3 + 9N^2 + 13N + 6)l_p^2 l_o} \quad (\text{if } l_p \gg l_o, l_{ini}, l_{fin}, d_p)$	
$K_{\delta_y}^R = \frac{K_{y\theta_z}^R K_{\theta_z y}^R K_y^R}{K_{y\theta_z}^R K_{\theta_z y}^R - K_y^R K_{\theta_z}^R}$	
$K_{\delta_y}^R \approx \frac{12EI_{y_p}}{(2N+3)l_p^3} \quad (\text{if } l_p \gg l_o, l_{ini}, l_{fin}, d_p)$	
$K_{\delta_z}^R = \frac{K_{z\theta_y}^R K_{\theta_y z}^R K_z^R}{K_{z\theta_y}^R K_{\theta_y z}^R - K_z^R K_{\theta_y}^R}$	

constants. For the classic serpentine springs $K_{\theta_x}^C$ simply expands to

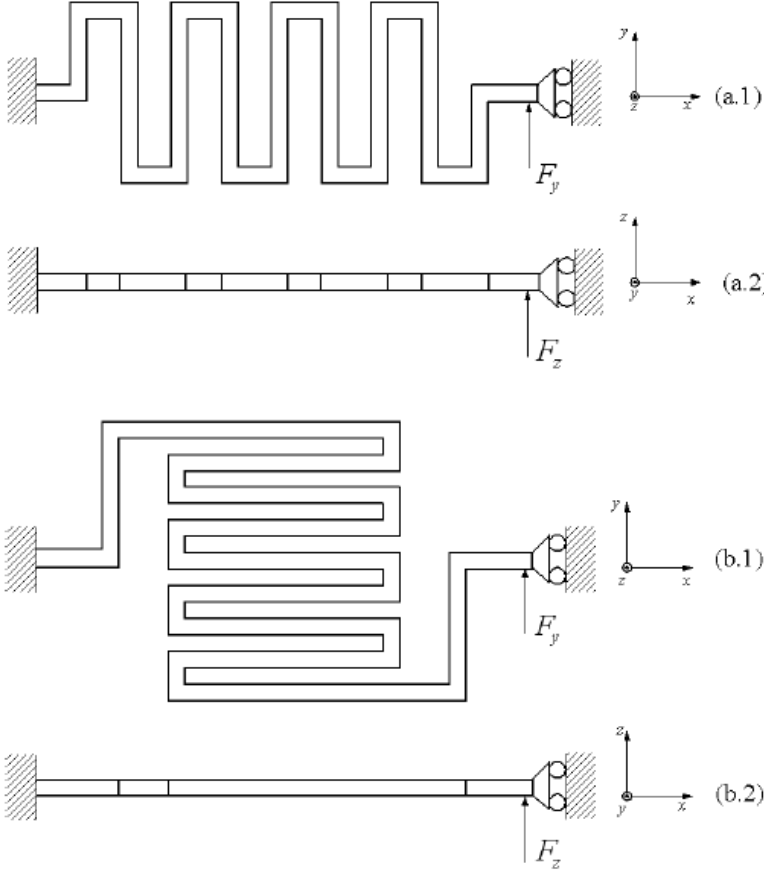


Figure 5.4: Classic serpentine spring with guided end along y-axis (a.1) and along z-axis (a.2). Rotated serpentine spring with guided end along y-axis (b.1) and along the z-axis (b.2).

$$K_{\theta_x}^C \approx \frac{Ew_0t^3}{24(N+1)l_o} \quad (5.1)$$

which depends on the third power of the thickness. For the rotated spring, by making the (admittedly oversimplifying) hypothesis of $t \gg w$, i.e. high thickness, neglecting and thus neglecting the series in (5.7) we obtain

$$K_{\theta_x}^R \approx \frac{Gtw_p^2}{3(2N+3)l_p} \quad (5.2)$$

which only depends on the first power of t . This advantage is progressively reduced for smaller and smaller thicknesses, but nonetheless confirms the qualitative considerations on the advantages of the use of rotated serpentine springs for torsional applications when a thick structural layer is available.

Apart from torsion, a very common use of these springs is as elastic elements in a linear actuator [49] or linear accelerometer [75]. A constant of interest for this case is then $Kx = Fx/\Delta x$. The expressions for K_x^C and K_x^R were thus calculated as well (5.B.2 - Table 5.2 and 5.3, second row). For this spring constant, substitution of the analytical expression of I_{zo} and I_{zp} results in expressions that exhibit the same (linear) dependence on the thickness.

Table 5.4: List of dimensions of the simulated springs

	classic serpentine	rotated serpentine
T(mm)	5-10-15	5-10-15
N	0-3-5	0-3-5
Lp (mm)	5	20-40...200
Wp (mm)	2	2
Lo (mm)	20-40...200	5
Wo (mm)	2	2
Lini (mm)	5	5
Lfin (mm)	5	5
Dp (mm)	5	5

For linear deflection along the other two axes (y and z), the most common cases in applications are such that the end of the spring is bound to move in the zy plane without rotation, i.e. the case of guided end [75]. We thus define $K_{\delta y}$ as the ratio $F_y/\Delta y$ when the spring end is bound to move along the y axis without rotation (Figure 5.4.a.2 b.2), and $K_{\delta z}$ as the ratio $F_z/\Delta z$ when the end is bound to move along the z axis without rotation (Figure 5.4.a.1 b.1). The full and approximated expressions for both kinds of spring are again derived in Appendix 5.B.3, 5.B.4, 5.B.5 and 5.B.6 and given in Tables 5.2 and 5.3, third and fourth row. Again, an analysis of the dependence of $K_{\delta y}$ and $K_{\delta z}$ on the design variables can be carried out. An interesting point is that, for classic springs, they depend inversely on the fourth and third power of N , respectively, while for the rotated springs they show a linear dependence on N .

Hence with the former it would be difficult to design low torsional stiffnesses (by making N high), and to maintain at the same time high stiffnesses for the other modes. This implies that keeping the resonance frequency of parasitic vibrational modes higher than that of the torsional mode is easier for rotated springs. Thus, once again, rotated springs are more suitable than classic springs for torsional applications. This last consideration shows that, regardless of the particular application, all of these constants are needed for proper design of the spring, because the target value for one of the constants (say $K_{\theta x}$ for torsional applications) should be designed by maintaining at the same time high values for the other constants, to avoid

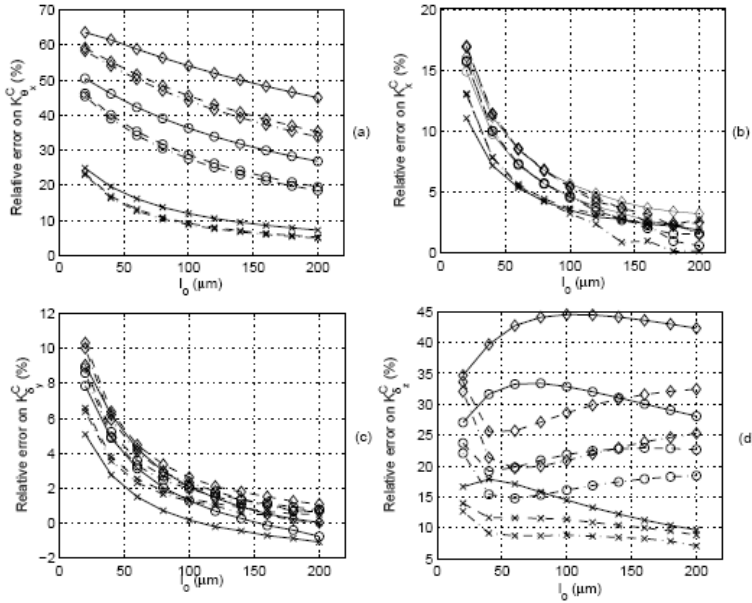


Figure 5.5: Relative error on the spring constants of the classical serpentine springs: $K_{\theta x}^C$ (a); K_x^C (b); $K_{\delta y}^C$ (c); $K_{\delta z}^C$ (d). $\text{---}\circ$ $t=10\ \mu\text{m}$, $N=0$; $\text{----}\circ$ $t=10\ \mu\text{m}$, $N=3$; $\text{--}\cdot\text{--}\circ$ $t=10\ \mu\text{m}$, $N=5$; $\text{---}\diamond$ $t=15\ \mu\text{m}$, $N=0$; $\text{----}\diamond$ $t=15\ \mu\text{m}$, $N=3$; $\text{--}\cdot\text{--}\diamond$ $t=15\ \mu\text{m}$, $N=5$; $\text{---}\times$ $t=5\ \mu\text{m}$, $N=0$; $\text{----}\times$ $t=5\ \mu\text{m}$, $N=3$; $\text{--}\cdot\text{--}\times$ $t=5\ \mu\text{m}$, $N=5$.

undesired deflections of the suspended structures, as well as parasitic resonant modes at low frequencies along the same degrees of freedom.

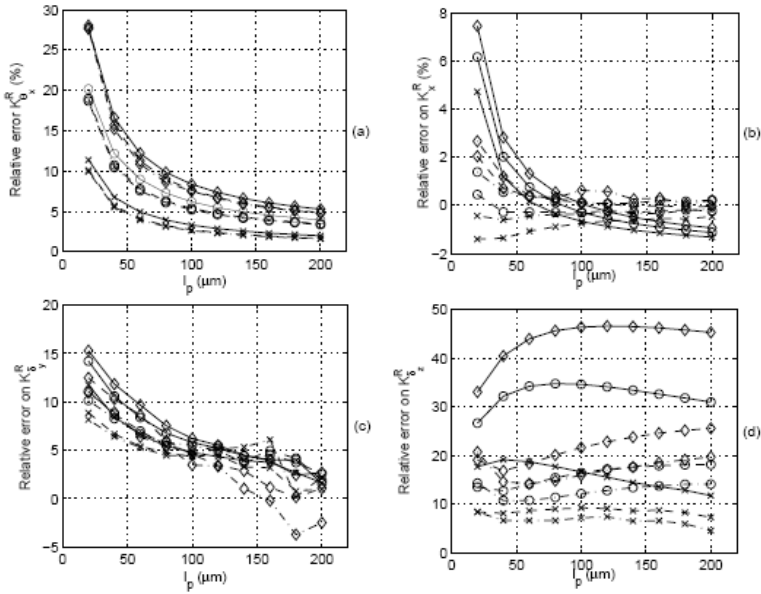


Figure 5.6: Relative error on the spring constants of the rotated serpentine springs: $K_{\theta x}^R$ (a); K_x^R (b); $K_{\delta y}^R$ (c); $K_{\delta z}^R$ (d). $\text{---}\circ$ $t=10\ \mu\text{m}$, $N=0$; $\text{----}\circ$ $t=10\ \mu\text{m}$, $N=3$; $\text{--}\cdot\text{--}\circ$ $t=10\ \mu\text{m}$, $N=5$; $\text{---}\diamond$ $t=15\ \mu\text{m}$, $N=0$; $\text{----}\diamond$ $t=15\ \mu\text{m}$, $N=3$; $\text{--}\cdot\text{--}\diamond$ $t=15\ \mu\text{m}$, $N=5$; $\text{---}\times$ $t=5\ \mu\text{m}$, $N=0$; $\text{----}\times$ $t=5\ \mu\text{m}$, $N=3$; $\text{--}\cdot\text{--}\times$ $t=5\ \mu\text{m}$, $N=5$.

5.4 FEM simulations

5.3.1 Description

In order to verify the analytical relationships found for the elastic spring constants we used a finite-element simulation program, ANSYS, and we implemented two kinds of simulations. The first one used the element BEAM4 to model the spring as a set of linked beams. BEAM4 is a uniaxial element with tension, compression, torsion, and bending capabilities. The element has six degrees of freedom at each node: displacements in the nodal x , y , and z directions and rotations about the nodal x , y , and z axes.

In the second kind of simulation, a three-dimensional meshing of the structures with the element SOLID45 was performed. SOLID45 is a brick element defined by eight nodes having three degrees of freedom (displacements) at each node. The geometrical parameters used in simulations for classic and rotated springs are listed in Table 5.4.

5.5 Results

The results of the simulations when the beam model was used are in perfect agreement with the analytic expressions, a result that was

expected as the BEAM4 is based on the elementary beam theory, used to deduce the analytical formulas as well. The very good fitting confirms the analytical relationships we found.

The results of the simulations with the solid model deviate from analytical results. In order to compare the FEM simulations with the analytical relations we define K_{sim} and K_{cal} the spring constant obtained respectively from the simulations and from the analytical formulas. Hence we calculate the relative error $\varepsilon = (K_{sim} - K_{cal}) / K_{sim}$ for both springs versus the most relevant dimension (l_o for the classic serpentine shape and l_p for the rotated serpentine shape), using the number of the repeated elements N and the thickness t as parameters.

In Figure 5.5 the relative errors on the spring constants for the classic serpentine springs are plotted. For high thickness ($15\mu m$) a considerable error (about 50%) is found for $K_{\theta x}^C$. This is due to the fact that, for high thickness, the slender beam approximation for each element of the spring is not valid, so that the evaluation of the bending is not exact. A large error is also found for the elastic constants $K_{\delta z}^C$, in which the term of the bending along z is significative, so that there is an high dependence on the thickness value. In other cases we found that the error is always under 20%.

In Figure 5.6 the relative errors on the spring constants for the rotated serpentine springs are plotted. A large error (50%) is found for $K_R dz$, again because of the high value of thickness ($15\mu m$). For K_x^R and $K_{\delta y}^P$ the error is less than 20% and 15%, respectively.

For $K_{\theta x}^R$, the relative error is less than 20% except for low value of l_o and thickness equal to $15\mu m$ when the error is more than 30%.

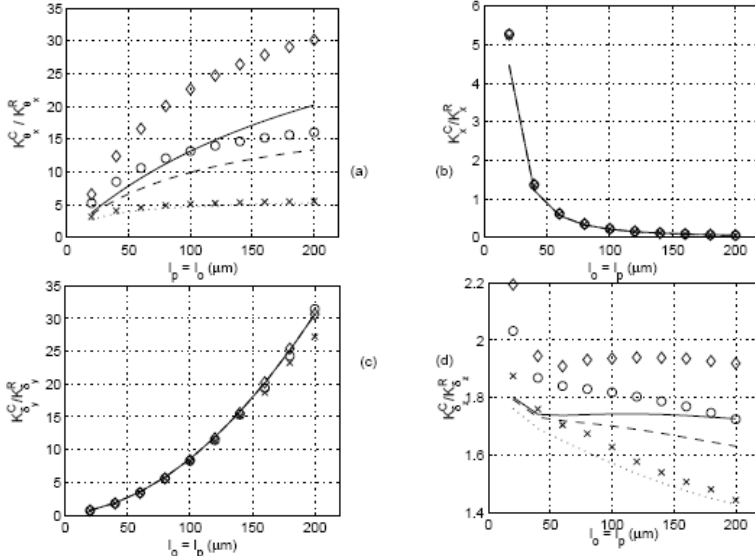


Figure 5.7: Ratio between the corresponding spring constants of the two structures (N=3). From simulations: $\diamond t = 15 \mu\text{m}$; $\circ t = 10 \mu\text{m}$; $\times t = 5 \mu\text{m}$. From analytical formulae: _____ $t = 15 \mu\text{m}$; ----- $t = 10 \mu\text{m}$; $t = 5 \mu\text{m}$.

The differences between the calculated and simulated value could also be caused by the fact that, in the described model, the length of the beams which constitutes the spring is supposed equal to the distance between the centers of two consecutive corners. This is clearly an approximation, especially when the dimensions of the corners are comparable with the length of the beam. It is also supposed that the joints between the beams are ideal, but this assumption becomes less and less valid as the section of the beam (and of the joints) becomes larger, i.e. for high thickness. For all the spring constants we verified a reduction of the error for high value of the parameters l_o and l_p , which validates the consideration that part of the error is due to deviation from the ideal slender beam geometry.

In order to compare the relative advantages of the two types of springs, in Figure 5.7 the calculated and simulated ratios between the corresponding spring constants are shown. To allow this comparison, the longer elements of the two springs (l_o for classic, l_p for rotated springs) were made equal. The ratios for K_x and $K_{\delta y}$ are almost coincident, while for the other two constants a significant deviation is observed for high thickness.

Nonetheless, the behavior as a function of the length is similar. This means that, at least for small thicknesses, the analytical formulas can

be used to compare the springs performance and they are an effective help to the designer in the choice of the best structure.

With the help of the data in Figure 5.7 a comparison of the two designs in torsional applications can be carried out as well. In particular, the torsional spring constant for rotated springs is much

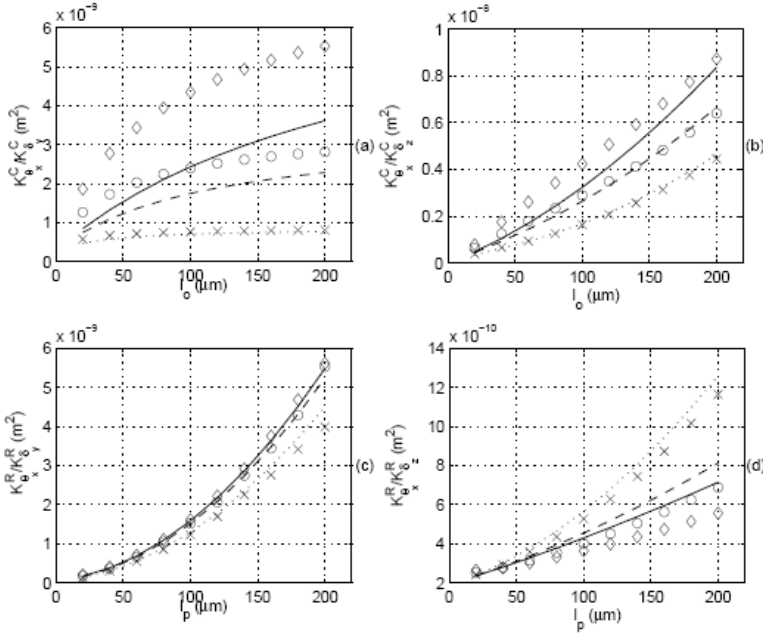


Figure 5.8: Ratio between the corresponding spring constants of the two structures ($N=3$). From simulations: $\diamond t=15 \mu\text{m}$; $\circ t=10 \mu\text{m}$; $\times t=5 \mu\text{m}$. From analytical formulae: _____ $t=15 \mu\text{m}$; ----- $t=10 \mu\text{m}$; $t=5 \mu\text{m}$.

smaller than for classic springs, especially for high thickness, as expected. Another measure of the suitability of rotated springs for torsional applications is given by the ratios between K_θ and the other constants, ratios which should be as small as possible to reduce the impact of parasitic resonant modes (i.e. to keep these modes at high frequency). Sample ratios for classic and rotated springs are shown in Figure 5.8. The ratios with respect to K_δ are of the same order of magnitude for the two designs, while for K_δ the rotated spring behaves much better than the other (by two orders of magnitude), confirming quantitatively the advantages of the latter design for torsional springs.

An important information which is contained in the Figure 5.7 is that the classic serpentine springs are much better when they are used as elastic element in x -direction because they have a K_x much smaller.

This is also an expected result which confirms that they are the best choice as elastic element in a linear actuator and linear accelerometer

5.6 Conclusions

In this chapter we showed an analytical approach to evaluate the spring constants of serpentine springs, useful in microstructures design. Two kind of serpentine springs were analyzed: one with classic shape and another with rotated serpentine shape. FEM simulations were used to check the analytical formulas and it was shown that the results are in accordance with the theory in the range of validity of the beam approximation. It was found that the analytical formulas are useful to compare the performances of the two kinds of springs. It was also verified that the rotated serpentine springs are more suitable for torsional applications, especially for high thickness of the structural layer.

5.A: Unit-load method

The spring constants are deduced from a set of linear equations obtained by using the principle of virtual work with the unit-load method. The principle of virtual work states that if a deformable structure in equilibrium under the action of a system of loads is given a small virtual deformation, then the virtual work done by the external forces (or loads) equals the virtual work done by the internal forces (or stress resultants)[61]. Two loading systems must be considered when using the unit-load method to find the displacement of a structure. The first system consists of the actual loads, while the second consists of a unit load acting alone on the structure. The unit-load is a dummy load that is introduced for the purpose of calculating the displacement Δ of the structure due to the actual loads. The unit load must correspond to the desired displacement Δ . A load that corresponds to a displacement is a load that acts on the structure at the point where the displacement is to be determined and has its positive direction in the same direction as a positive displacement.

After the application of the unit-load and the use of the principle of virtual work the following equation is obtained [61]:

$$\left. \begin{matrix} 1 \cdot \Delta \\ 1 \cdot \phi \end{matrix} \right\} = \int \frac{N_u N_L}{EA} dx + \int \frac{M_u M_L}{EI} dx + \int \frac{T_u T_L}{EJ} dx \quad (5.3)$$

N_L , M_L and T_L are the axial force, bending moment and twisting couple caused by the actual loads, respectively, while N_U , M_U and T_U are produced by the unit-load, and have the dimensions of force or moments per unit of the applied unit-load; E is the Young's modulus and G the Shear Modulus, which is equal to $E/(2(1 + \nu))$, where ν is the Poisson's ratio; A is the section of the beam, I is the moment of inertia of the section and J is the cross-sectional torsion factor. This equation can be used to find the displacement at any point of a structure when the material is linearly elastic.

5.B: Calculation of the spring constants

5.B.1. Torsional spring constant K_{θ}

To measure the torsional spring constant we apply a torsion moment M_x and we calculate the rotation by using the unit-load method. For the classical serpentine springs, the following relation is obtained:

$$1 \cdot \theta_x = \sum_{beams} \left(\int_0^{l_{beam}} \frac{T_L T_U}{GJ} dx + \int_0^{l_{beam}} \frac{M_L M_U}{EI} dx \right) \quad (5.4)$$

The torques and the moments caused by the loads (actual and dummy) are derived and substituted in (5.4). In order to make their evaluation easier, for each beam a local system of reference having its x-axis along central axis is defined. Hence, after the derivation of a free-body diagram, for the classical serpentine spring the following relation is obtained:

$$\begin{aligned} \theta_x = & \int_0^{l_p} \frac{M_x}{GJ_p} dx + \int_0^{\frac{l_o}{2}} \frac{M_x}{EI_{y_o}} dx + \int_0^{l_p} \frac{M_x}{GJ_p} dx + \int_0^{l_o} \frac{M_x}{EI_{y_o}} dx + \\ & + \int_0^{l_o} \frac{M_x}{GJ_p} dx + \sum \left[\int_0^{l_o} \frac{M_x}{EI_{y_o}} dx + \int_0^{l_p} \frac{M_x}{GJ_p} dx + \int_0^{l_o} \frac{M_x}{EI_{y_o}} dx + \right. \\ & \left. + \int_0^{l_p} \frac{M_x}{GJ_p} dx \right] + \int_0^{\frac{l_o}{2}} \frac{M_x}{EI_{y_o}} dx + \int_0^{l_p} \frac{M_x}{GJ_p} dx \end{aligned} \quad (5.5)$$

The moment of inertia I_{y_o} and the torsion factor J_p for a beam with rectangular section are [10]

$$I_{y_o} = \frac{w_o t^3}{12} \quad (5.6)$$

$$J_p = \frac{tw_p^3}{3} \left(1 - \frac{192w_p}{\pi^3 I_{y_o}} \sum_{i=1,3,5,\dots} \frac{i}{i^5} \tanh \left(\frac{i\pi t}{2w_p} \right) \right) \quad (5.7)$$

Simplifying (5.5), the following equation is obtained:

$$\theta_x = M_x \left[\frac{2(N+1)}{EI_{y_o}} l_o + \frac{2(N+2)}{GJ_p} l_p \right] \quad (5.8)$$

From (5.8) we calculate $K_{\theta_x}^C = M_x / \theta_x$, the torsional spring constant of the classic serpentine spring. Not surprisingly, the result is equal to the series of the spring constant of each element of which the spring is constituted:

$$K_{\theta_x}^C = \left[\frac{2(N+1)}{EI_{y_o}} l_o + \frac{2(N+2)}{GJ_p} l_p \right]^{-1} \quad (5.9)$$

In most applications, $l_o \gg l_p$ and/or $w_p \gg w_o$ are verified, which is equivalent to neglect the term relative to the parallel elements because they are much shorter and/or wider than the others, and thus can be considered undeformed. In this case, (5.9) reduces to:

$$K_{\theta_x}^R \approx \frac{EI_{y_o}}{2(N+1)l_o} \quad (5.10)$$

We consider the spring with the rotated serpentine and we apply the same method obtaining the following relation:

$$\theta_x = M_x \left[\frac{4(N+1)}{EI_{y_o}} l_o + \frac{(2N+3)l_p + 2d_p + l_{ini} + l_{fin}}{GJ_p} \right] \quad (5.11)$$

Again we notice that the overall spring constant equals that of the series of each element:

$$K_{\theta_x}^R = \left[\frac{4(N+1)}{EI_{y_o}} l_o + \frac{(2N+3)l_p + 2d_p + l_{ini} + l_{fin}}{GJ_p} \right]^{-1} \quad (5.12)$$

When $l_p \gg l_o$, l_{ini} , l_{fin} , d_p or $w_o \gg w_p$ the equation reduces to:

$$K_{\theta_x}^R \approx \frac{GJ_p}{(2N+3)l_p} \quad (5.13)$$

5.B.2. Spring constant K_x

We use the principle of virtual work by applying an exploring load along the x axis. We obtain for the classic serpentine springs:

$$K_x^C = \left[\frac{(N+1)l_o^3}{6EI_{y_o}} + \frac{(N+1)l_o^2 l_p}{2EI_{z_p}} \right]^{-1} \quad (5.14)$$

Again, if $l_o \gg l_p$:

$$K_x^C \simeq \frac{6EI_{z_o}}{(N+1)l_o^3} \quad (5.15)$$

For the rotated serpentine spring the following spring constant is calculated:

$$K_x^R = \left[\frac{(4(N+1)l_o)^3}{3EI_{z_o}} + \frac{(2N^3 + 9N^2 + 13N + 6)l_p + 6(N+1)d_p l_o^2}{3EI_{z_p}} \right]^{-1} \quad (5.16)$$

5.B.3. Spring constant K_{δ} for the classic serpentine springs with guided end

This is a classical iperstatic problem which can be addressed by selecting one of the constraints and solving two cases: one with the same load system without the constraint(case (1)), and one where only the unknown reaction due to the excluded constraint, and not the applied loads, is considered (case (2)). The additional unknown, represented by the reaction, is computed by imposing a condition of congruence between the displacement (or rotation) in the direction of the excluded constraints. It is then possible to study a system with the same number of equations and unknowns.

Hence the problem is divided in two parts: in case (1) the relation between θ_{z1} and F_y is calculated:

$$\theta_{z1} = (K_{\theta_{zy}}^C)^{-1} F_y \quad (5.17)$$

In the case (2) the relation between θ_{z1} and M_{Rz} is:

$$\theta_{z2} = (K_{\theta_z}^C)^{-1} M_{Rz} \quad (5.18)$$

The condition of congruence imposes that the sum of the rotation caused by the loads and by the moment of reaction is zero:

$$\theta_{z1} + \theta_{z2} = 0 \quad (5.19)$$

Substituting (5.17) and (5.18) in (5.19), the moment of the reaction is derived:

$$M_{Rz} = -\frac{K_{\theta_z}^C}{K_{\theta_{zy}}^C} F_y \quad (5.20)$$

After these passages the problem is reduced to the calculation of the displacement δ_y when a load F_y and a moment M_{Rx} are applied to a free end of the spring.

$$\delta_y = \left(K_y^C\right)^{-1} F_y + \left(K_{y\theta_z}^C\right)^{-1} M_{Rx} = \frac{K_{y\theta_z}^C K_{\theta_z y}^C - K_y^C K_{\theta_z}^C}{K_{y\theta_z}^C K_{\theta_z y}^C K_y^C} F_y \quad (5.21)$$

Then the spring constant $K_{\delta_y}^C$ is:

$$K_{\delta_y}^C = \frac{K_{y\theta_z}^C K_{\theta_z y}^C - K_y^C K_{\theta_z}^C}{K_{y\theta_z}^C K_{\theta_z y}^C K_y^C} \quad (5.22)$$

K_y^C , $K_{y\theta_z}^C$, $K_{\theta_z y}^C$ and $K_{\theta_z}^C$ are calculated with the unit-load method:

$$K_y^C = \left[\frac{(2(N+2)l_p)^3}{3EI_{z_p}} + \frac{(8N^3 + 36N^2 + 55N + 27)l_p^2 l_o}{3EI_{z_o}} \right]^{-1} \quad (5.23)$$

$$K_{y\theta_z}^C = K_{\theta_z y}^C = \left[\frac{2(N^2 + 3N + 4)l_p l_o}{EI_{z_o}} + \frac{2(N+2)^2 l_p^2}{EI_{z_p}} \right]^{-1} \quad (5.24)$$

$$K_{\theta_z}^C = \left[\frac{2(N+2)l_p}{EI_{z_p}} + \frac{2(N+1)l_o}{EI_{z_o}} \right] \quad (5.25)$$

And, if $l_o \gg l_p$:

$$K_y^C \simeq \frac{3EI_{y_o}}{(8N^3 + 36N^2 + 55N + 27)l_p^2 l_o} \quad (5.26)$$

$$K_{y\theta_z}^C = K_{\theta_z y}^C \simeq \frac{EI_{z_o}}{2(N^2 + 3N + 2)l_p l_o} \quad (5.27)$$

$$K_{\theta_z}^C \simeq \frac{EI_{z_o}}{2(N+1)l_o} \quad (5.28)$$

Substituting (5.26), (5.27) and (5.28) in (5.22), the approximate equation valid for $l_o \gg l_p$ is deduced:

$$K_{\delta_y}^C \simeq \frac{3EI_{z_o}(N+1)}{(12N^4 + 64N^3 + 130N^2 + 116N + 38)l_p^2 l_o} \quad (5.29)$$

5.B.4. Spring constant $K_{\delta_y}^C$ for the classic serpentine spring

Similarly to $K_{\delta_y}^C$ in Appendix 5.B.3, the spring constant $K_{\delta_x}^C$ is calculated with the following expression:

$$K_{\delta_z}^C = \frac{K_{z\theta_y}^C K_{\theta_y z}^C - K_z^C K_{\theta_y}^C}{K_{z\theta_y}^C K_{\theta_y z}^C K_z^C} \quad (5.30)$$

K_z^C , $K_{z\theta_y}^C$, $K_{\theta_y z}^C$ and $K_{\theta_y \theta_z}^C$ are calculated with the unit-load method:

$$K_z^C = \left[\frac{(2(N+2)l_p)^3}{3EI_{y_p}} + \frac{(N+1)l_o^3}{6EI_{y_o}} + \frac{(N+1)l_o^2 l_p}{GJ_p} + \frac{(8N^3 + 36N^2 + 55N + 27)l_p^2 l_o}{3GJ_o} \right]^{-1} \quad (5.31)$$

$$K_{\theta_y z}^C = K_{z\theta_y}^C = \left[\frac{2(N^2 + 3N + 2)l_p l_o}{GJ_o} + \frac{2(N+2)^2 l_p^2}{EI_{y_p}} \right]^{-1} \quad (5.32)$$

$$K_{\theta_y}^C = \left[\frac{2(N+2)l_p}{EI_{y_p}} + \frac{2(N+1)l_o}{GJ_o} \right]^{-1} \quad (5.33)$$

For $l_o \gg l_p$ it is possible to approximate (5.32) and (5.33):

$$K_{\theta_y z}^C \approx \frac{GJ_o}{2(N^2 + 3N + 2)l_p l_o} \quad (5.34)$$

$$K_{\theta_y}^C \approx \frac{GJ_o}{2(N+1)l_o} \quad (5.35)$$

Supposing $l_o \gg l_p$ and high N , (5.31) is simplified in:

$$K_z^C \approx \left[\frac{(N+1)l_o^3}{6EI_{y_o}} + \frac{(8N^3 + 36N^2 + 55N + 27)l_p^2 l_o}{3GJ_o} \right]^{-1} \quad (5.36)$$

Substituting the approximate expression (B.34), (B.35) and (B.36) in (B.30):

$$K_{\delta_z}^C \approx \frac{6EI_{y_o} GJ_o}{(N+1)l_o^3 GJ_o + (16N^3 + 36N^2 + 43N + 3)l_p^2 l_o EI_{y_o}} \quad (5.37)$$

5.B.5. Spring constant K_{δ_y} for the rotated serpentine spring

Applying the method described in Appendix 5.B.3, K_{δ_y} , the ratio between F_y and δ_y in the condition of guided-end along the y axis Figure 5.4, is calculated:

$$K_{\delta_y}^R = \frac{K_{y\theta_z}^R K_{\theta_z y}^R - K_y^R K_{\theta_z}^R}{K_{y\theta_z}^R K_{\theta_z y}^R K_y^R} \quad (5.38)$$

K_y^R , $K_{y\theta_z}^R$, $K_{\theta_z y}^R$ and $K_{y\theta_z}^R$ are calculated with the unit-load method:

$$K_y^R = \left[\frac{(N+1)l_o \left(l_{fin}^2 + (l_{fin} + d_p)^2 + (l_{fin} + l_p + d_p)^2 + (l_{fin} + 2d_p + l_p)^2 \right)}{EI_{z_o}} + \frac{\left(2(N+1) \left((l_{fin} + d_p + l_p)^3 - (l_{fin} + d_p)^3 \right) \right)}{3EI_{z_p}} + \frac{(l_{ini} + l_{fin} + l_p + 2d_p)^3}{3EI_{z_p}} \right]^{-1} \quad (5.39)$$

$$K_{\theta_z}^R = K_{y\theta_z}^R = \left[\frac{2(N+1)l_p (lp + 2l_{fin} + 2d_p) + (l_{ini} + l_{fin} + l_p + 2d_p)^2}{EI_{z_p}} + \frac{(N+1)l_o (4l_{fin} + 4d_p + 2l_p)}{EI_{z_o}} \right]^{-1} \quad (5.40)$$

$$K_{\theta_z}^R = \left[\frac{(2N+3)l_p + 2d_p + l_{ini} + l_{fin}}{EI_{z_p}} + \frac{4(N+1)l_o}{EI_{z_o}} \right]^{-1} \quad (5.41)$$

For $lp \gg l_o, l_{ini}, l_{fin}, d_p$:

$$K_y^R \simeq \frac{3EI_{z_p}}{(2N+3)l_p^3} \quad (5.42)$$

$$K_{\theta_z}^R \simeq \frac{2EI_{z_p}}{(2N+3)l_p^2} \quad (5.43)$$

$$K_{\theta_z}^R \simeq \frac{EI_{z_p}}{(2N+3)l_p} \quad (5.44)$$

Substituting the approximate expressions of (5.42), (5.43) and (5.44) into (5.38):

$$K_{\delta_y}^R \simeq \frac{12EI_{z_p}}{(2N+3)l_p^3} \quad (5.45)$$

5.B.6. Spring constant $K_{\&}$ for the rotated serpentine spring

We define $K_{\&}^R$ as the ratio between F_z and δ_z in the condition of guided-end along z axis (Figure 5.4). With the method in Appendix B.3, the following expression is deduced:

$$K_{\delta_z}^R = \frac{K_{z\theta_y}^R K_{\theta_y z}^R - K_z^R K_{\theta_y}^R}{K_{z\theta_y}^R K_{\theta_y z}^R K_z^R} \quad (5.46)$$

K_z^R , $K_{z\theta_y}^R$, $K_{\theta_y z}^R$ and $K_{\theta_y}^R$ are calculated with the unit-load method:

$$K_z^R = \left[\frac{\left((2N^3 + 9N^2 + 13N + 6)l_p + 6d_p (N+1)^2 \right) l_o^2}{3GJ_p} + \frac{4((N+1)l_o)^3}{3EI_{y_o}} + \frac{2(N+1)\left((l_{fin} + l_p + d_p)^3 - (l_{fin} + d_p)^3 \right) + (l_{ini} + l_{fin} + l_p + 2d_p)^3}{3EI_{y_p}} + \frac{(N+1)\left((l_{fin} + l_p + d_p)^2 + (l_{fin} + d_p)^2 + (l_{fin} + 2d_p + l_p)^2 + l_{fin}^2 \right) l_o}{GJ_o} \right]^{-1} \quad (5.47)$$

$$K_{\theta_y z}^R = K_{z\theta_y}^R = \left[\frac{(l_{ini} + l_{fin} + l_p + 2d_p)^2}{2EI_{y_p}} + \frac{(2N+2)\left((l_{fin} + l_p + d_p)^2 - (l_{fin} + d_p)^2 \right)}{3EI_{y_p}} + \frac{(N+1)(4l_{fin} + 4d_p + 2l_p)l_o}{GJ_o} \right]^{-1} \quad (5.48)$$

$$K_{\theta_y}^R = \left[\frac{(2N+3)l_p + 2d_p + l_{ini} + l_{fin}}{EI_{y_p}} + \frac{4(N+1)l_o}{GJ_o} \right]^{-1} \quad (5.49)$$

For $l_p \gg l_o$, l_{ini} , l_{fin} , d_p :

$$K_{\theta_y z}^R \simeq \frac{2EI_{y_p}}{(2N+3)l_p^2} \quad (5.50)$$

$$K_{\theta_y}^R \simeq \frac{EI_{y_p}}{(2N+3)l_p} \quad (5.51)$$

For $l_p > l_o$, l_{ini} , l_{fin} , d_p and high N :

$$K_z^R = \left[\frac{(2N+3)l_p^3}{3EI_{y_p}} + \frac{(2N^3+9N^2+13N+6)l_p l_o^2}{3GJ_p} \right]^{-1} \quad (5.52)$$

Substituting (5.50), (5.51) and (5.52) into (5.46), the following expression for $K_{\delta_z}^R$ is obtained:

$$K_{\delta_z}^R \simeq \frac{12EI_{y_p} GJ_p}{(2N+3)l_p^3 GJ_p + 4(2N^3+9N^2+13N+6)l_p l_o^2 EI_{y_p}} \quad (5.53)$$

If l_p is high and N is small, the following simplified relation is obtained:

$$K_{\delta_z}^R \simeq \frac{12EI_{y_p}}{(2N+3)l_p^3} \quad (5.54)$$

This relation appears to be useful in spring design, and is empirically deduced in [ref]; however, our analysis shows that (5.54) is a good approximation of (5.46) only for high values of the length l_p and very low l_o and N .

Chapter 6

Electrostatic Levitational Actuators

6.1 Introduction

The working principle of the laterally driven electrostatic comb-finger actuator is well known (see chapter 2): it is based on the lateral motion of engaging and disengaging interdigitated comb finger structures. Because of its geometry, the generated electrostatic force is weakly dependent on the position of the moving finger. Nevertheless, comb-drive actuators also show an out-of-plane component of the force. If they are designed as lateral actuators, efforts are made to keep this parasitic force to a minimum [82-83]. For example, this effect is known to cause sensitivity variations and cross sensitivity increments in MEMS gyroscopes [84-85].

However, this parasitic levitation effect can be exploited to design vertical actuators, with the advantages of obtaining out-of-plane displacements even when only one structural layer is available, and of eliminating electrostatic (pull-in) instability [86]. Levitational actuators are readily implemented in any planar technology which provides comb finger structures for lateral actuation.

There are different applications for these actuators. They can be used to realize microbalances (oscillator based mass sensors) because of the high ratio between surface and mass, they will have high sensitivity allowing to detect mass changes of nanograms [87]. An other application is in Phase Shifting Diffraction Interferometry because the required force is low and controlled displacements in the nanometers scale are possible [86].

An in-depth study of the capabilities and the limitations of these actuators is not present in literature. This chapter presents an analysis of the electrostatic levitational actuators, together with FEM simulations and measurements on torsional devices. Moreover, the dependence of the levitational force on the most important geometric parameters is also investigated by using FEM simulations.[88]

6.2 Fabricated Devices

To evaluate the performances of this kind of electrostatic actuation, we designed and fabricated two types of levitated mechanical resonators (vertical and torsional). The technology used was STMicroelectronics THELMA, a thick layer technology designed for inertial sensors. Two sample SEM images of a vertical (left) and a torsional (right) resonator are given in Figure 6.1 SEM micrograph of the vertical resonator (left) and of the torsional-resonator (right).. The schematic structure of our devices is given in Figure 6.2: Schematic structure of the vertical resonator (left) and of the torsional-resonator (right), where both vertical (left) and torsional (right) devices are shown. Their structure is that of a classical two-port MEMS resonator. The driving electrodes are symmetric to compensate for the in-plane force of the comb-fingers.

Because of the thickness of the structural layer, classic beam springs or serpentine springs had shown several limitations [89]. For this reason, specifically designed suspension springs (rotated serpentes), with better performance for high thickness, were used. The reader is referred to the results developed by some of the authors in [89], where a full analysis of this kind of spring is exposed.

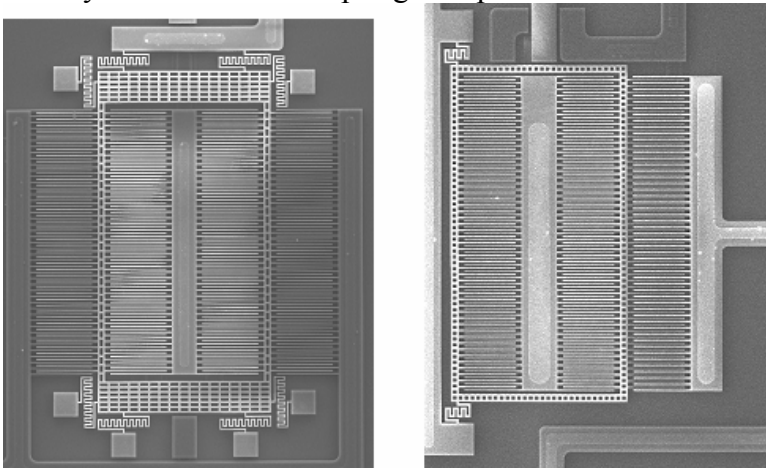


Figure 6.1 SEM micrograph of the vertical resonator (left) and of the torsional-resonator (right).

6.3 Theoretical Analysis

The electrostatic levitation is caused by the presence of more than two conductors in the system, and its modelling usually requires going

beyond the parallel-plate approximation for the capacitance. Specifically, the levitation effect can be observed for three-electrode structures like the one shown in Figure 6.3, where a ground plane under the fingers is present. When an electrical potential is applied to the stationary electrodes, the presence of the ground plane causes an unbalanced electrostatic field distribution, which results in vertical force induced in the movable finger.

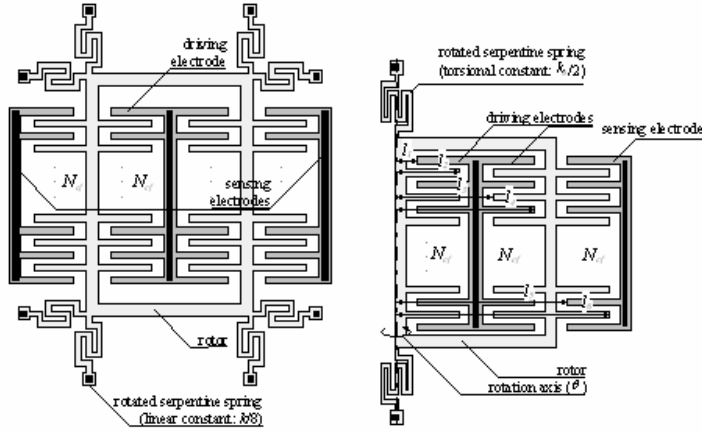


Figure 6.2: Schematic structure of the vertical resonator (left) and of the torsional-resonator (right)

Our devices of Figure 6.1 can be described by the section in Figure 6.3 along any vertical plane perpendicular to the fingers axis.

To design these structures, information on the actual values of the electrostatic forces acting on the movable fingers are required. The stationary electrode, the movable electrode and the ground plane can be considered as a system with three capacitances, as described in Figure 6.4. The levitation force for unit of length (N/m) in the z -direction can be evaluated by using the following relation.

$$f_z = \frac{1}{2} \left(\frac{dc_{sm}}{dz} + \frac{dc_{sg}}{dz} \right) V^2 = \frac{1}{2} \frac{dc_s}{dz} V^2 \quad (6.1)$$

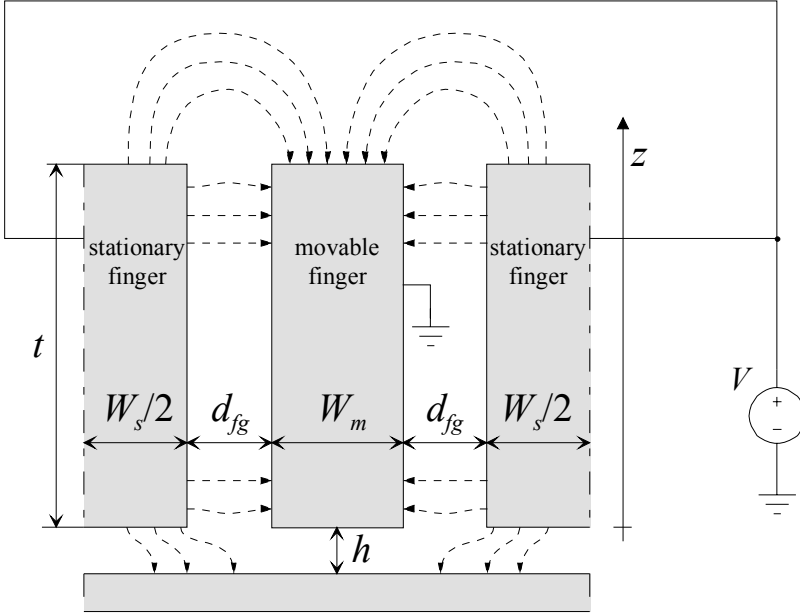


Figure 6.3: Cross section of a comb finger under the levitation force induced by a potential V on the two stationary fingers. Dashed lines are electric field lines

Tang et al. [83] observed that the levitation force linearly decreases with the vertical displacement of the movable finger till it equals zero at a displacement z_0 . This means that z_0 is an upper limit for the use of this actuation under quasi-static conditions. This relationship can be described as follows [83]:

$$f_z = -\alpha(z - z_0)V^2. \quad (6.2)$$

where f_z is the force for unit length. Unfortunately, the parameters α and z_0 cannot be easily determined by theoretical analysis of the electrostatic problem. For example, Schwarz-Christoffel conformal mapping, a common technique used for this class of problems [90-91], does not allow for an easy solution when z is different from 0. Hence FEM electrostatic simulations (with the FEMLAB[®] software package), were used to predict the structure behavior.

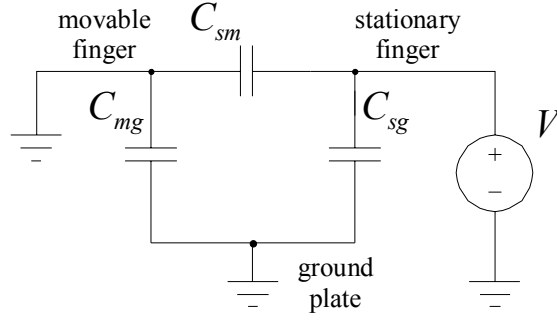


Figure 6.4: Electrical equivalent of a comb finger

By using the software the total capacitance $c_s(z)$ in the range $z \in [0 \mu\text{m}, 2 \mu\text{m}]$ for the two-dimensional cross-section of Figure 6.1 was calculated. The expression (6.2) was subsequently used to fit the simulated results with a parabolic function (Figure 6.5):

$$c_s(z) = c_0 - \alpha (z - z_0)^2 \quad (6.3)$$

and the fitting parameters c_0 , α and z_0 were obtained. In the vertical device (Figure 6.1, left) the total levitation force acting on a comb finger of length L is readily obtained by multiplying the value of f_z obtained from the simulation by the length of the finger. This 2D approximation is justified by the fact that the contribute of the fringe field in the direction perpendicular to the simulated section (Figure 6.3) is negligible because $L=100 \mu\text{m}$. For torsional devices, which are the main focus of the paper, the torque applied to a comb finger is computed with the following expression:

$$M_{el} = \int_{l_a}^{l_b} x f_z dx \quad (6.4)$$

where l_a and l_b are the distances of the two extremes of the comb finger from the rotational axis.

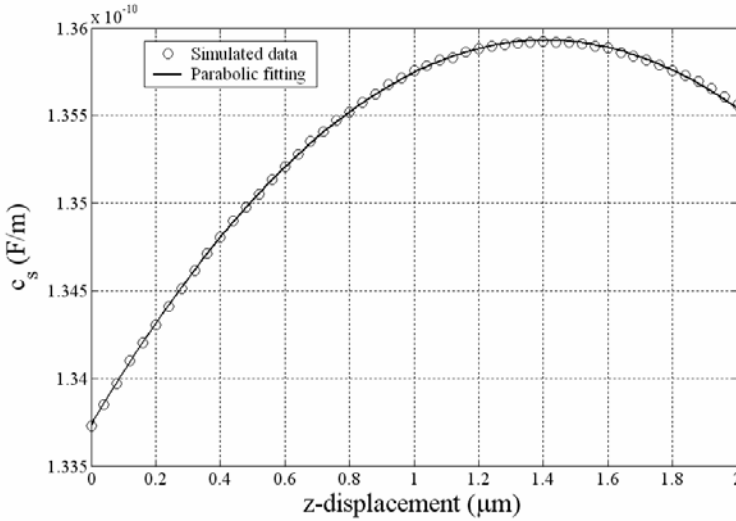


Figure 6.5: Results of the simulation of the cross section of the comb finger of the test structures and parabolic fitting of these data

6.4 Measurements methods

In this section some problems related to the measurements method of this kind of resonators are exposed. All the calculations are done by considering a lateral/vertical resonator. Successively the obtained results will also be applied to a torsional resonator.

6.4.1 The problem of the parasitic capacitance

Like for the classic lateral comb finger microresonators, the levitational resonators can be actuated by applying between the rotor and stator a sinusoidal signal of frequency closet o the mechanical resonance frequency of the system.

The oscillation of the movable plate is only limited by dissipative factors while as the input signal A typical circuit to characterize the resonator is represented in figure:

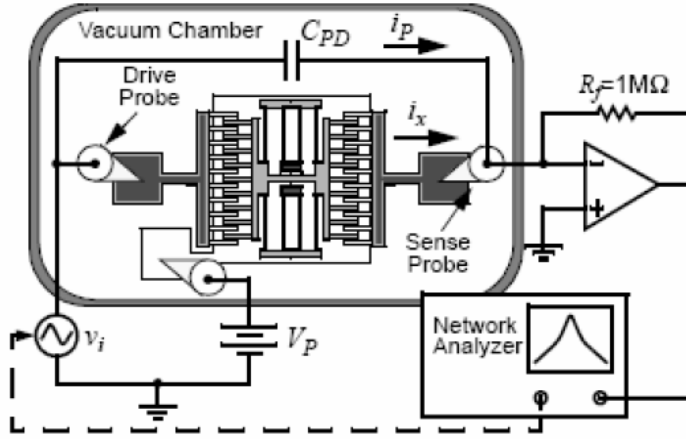


Figure 6.6: Measurement circuit for micro resonator.

A DC voltage is applied to the rotor and produces a static displacement. The output signal is measured on the stator and is caused by capacitance variation between stator and rotor.

A network analyzer is used to deduce the frequency spectrum of the output signal. The system is a vacuum chamber in order to reduce the effect of air damping.

By considering a system with vertical actuation, the sense current will be deduced from the following equation:

$$i_s(t) = \frac{d}{dt} (C_s(z(t)) V_0) \quad (6.5)$$

where C_s is the total capacitance, which can be substituted by a linear approximation:

$$C_s(z) = C_s(0) + \left. \frac{\partial C_s}{\partial z} \right|_{z=0} z \quad (6.6)$$

while V_0 is DC voltage. By considering the dependence on the displacements of the capacitance:

$$i_s(t) = \left. \frac{\partial C_s}{\partial z} \right|_{z=0} \frac{dz}{dt} V_0 \quad (6.7)$$

Between the rotor and the driving electrode the following voltage is applied:

$$V_D = V_0 + v_i \sin(\omega t) \quad (6.8)$$

The total force acting on the movable plate is the sum of the force on the two electrodes:

$$f_{tot} = f_D + f_S = \frac{1}{2} \frac{\partial C_D}{\partial z} \bigg|_{z=0} (V_0 + v_i \sin(\omega t))^2 + \frac{1}{2} \frac{\partial C_S}{\partial z} \bigg|_{z=0} V_0^2 \quad (6.9)$$

Hence the electrostatic force is:

$$f_{tot} = \left(\frac{1}{2} \frac{\partial C_D}{\partial z} \bigg|_{z=0} \left(V_0^2 + \frac{v_i^2}{2} \right) + \frac{1}{2} \frac{\partial C_S}{\partial z} \bigg|_{z=0} V_0^2 \right) + \frac{\partial C_D}{\partial z} \bigg|_{z=0} V_0 v_i \sin(\omega t) - \frac{1}{4} \frac{\partial C_D}{\partial z} v_i^2 \cos(2\omega t) \quad (6.10)$$

The first term causes is the static displacement, the second term is the driving oscillations. The third term can be neglected because the amplitude is low and the displacement caused by this term is slow as the resonator will be driven at the resonance frequency.

Hence in the frequency domain:

$$F(\omega) = V_0 \frac{\partial C_D}{\partial z} \bigg|_{z=0} V_i \quad (6.11)$$

By considering the typical equation of motion of a second order system:

$$-M\omega^2 Z + j\omega bZ + k_{eq} = F(\omega) \quad (6.12)$$

From which the transfer function is deduced:

$$\frac{Z(\omega)}{F(\omega)} = \frac{k_{eq}^{-1}}{-\frac{M}{k_{eq}}\omega^2 + j\frac{b}{k_{eq}} + 1} \quad (6.13)$$

Substituting (6.11) in (6.13), the transfer function displacement versus voltage is obtained:

$$\frac{Z}{V_i} = \frac{Z}{F} \frac{F}{V_i} = \frac{k_{eq}^{-1} V_0 \left. \frac{\partial C_D}{\partial z} \right|_{z=0}}{1 - \left(\frac{\omega}{\omega_r} \right) + j \frac{\omega}{Q\omega_r}} \quad (6.14)$$

Substituting eq. (6.14) in (6.7), a relation output current versus input voltage signal is deduced:

$$I_s = \frac{j\omega k_{eq}^{-1} V_o^2 \left(\left. \frac{\partial C_s}{\partial z} \right|_{z=0} \right) \left(\left. \frac{\partial C_D}{\partial z} \right|_{z=0} \right)}{1 - \left(\frac{\omega}{\omega_r} \right)^2 + j \frac{\omega}{Q\omega_r}} V_i \quad (6.15)$$

This is the current which can be measured with a transresistive amplifier.

Unfortunately in this application it is not possible to use this approach as a parasitic capacitance is present between the driving and sensing electrodes. As this parasitic capacitance C_{SD} is quite large, the current at the same frequency of the driving signal caused by its presence is quite large, hence the output signal caused by the movable plate cannot be resolved. Alternative methods are then necessary.

6.4.1.1 EAM modulation

With this method, the current which must be measured is separated by the parasitic current in the frequency domain. An amplitude modulation is reached with this method, so it is called EAM (Electromechanical Amplitude Modulation).

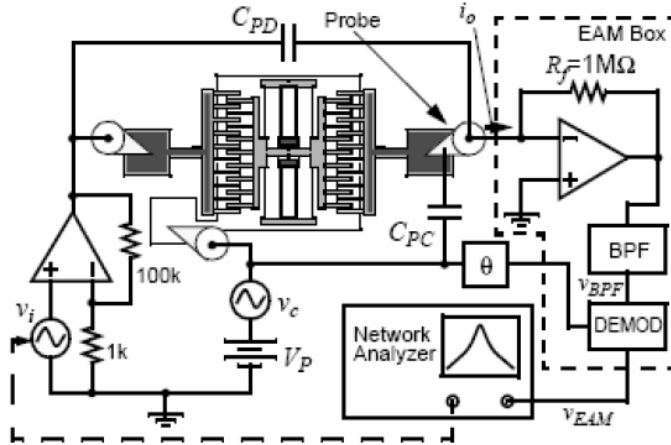


Figure 6.7: Scheme of the EAM circuit.

The resonator is polarized with a Dc voltage V_p on the stator, then an input signal $v_i = V_i \cos(\omega t)$ is present on the driving electrode. A signal is added to the polarization $v_c = V_c \cos(\omega_c t)$. The output current is deduced:

$$i_o = C_{PD} \frac{dv_i}{dt} + C_{PC} \frac{dv_c}{dt} + C(t) \frac{dv_c}{dt} + (V_0 + v_c) \frac{dC}{dt} \quad (6.16)$$

Where C_{PD} and C_{PC} are the parasitic capacitance while $C(t)$ is the capacitance we want to detect. $C(t)$ can be divided into a static part C_0 and a dynamic C_m .

At the resonance frequency:

$$i_o = i_p - \omega_0 V_0 \cos(\omega_0 t) - \frac{1}{2}(\omega_c - \omega_0) V_c C_m \cos((\omega_c - \omega_0)t) \\ + \frac{1}{2}(\omega_c + \omega_0) V_c C_m \cos((\omega_c + \omega_0)t)$$

In this formula we find the parasitic component of the current i_p at the frequency f_c and at the resonance frequency f_0 , a current at frequency f_0 compaiono and two motional current at f_0-f_c and f_0+f_c (Figure 6.8).

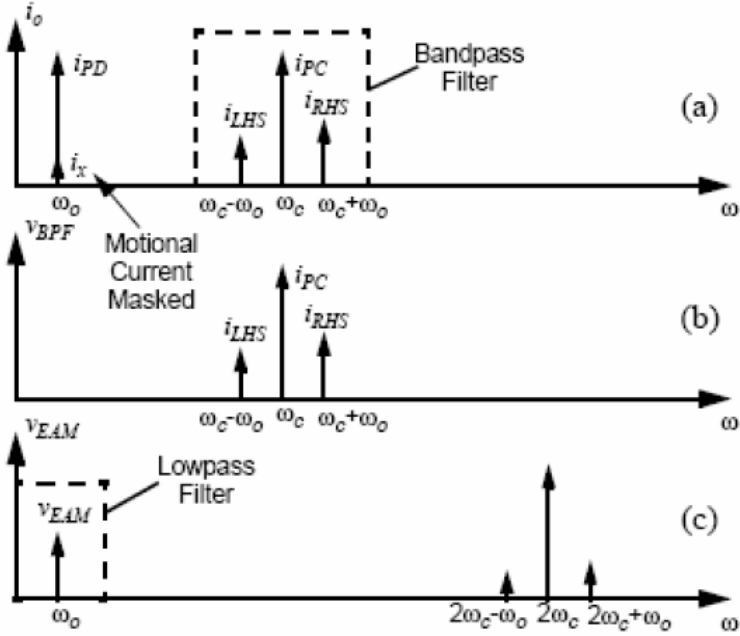


Figure 6.8: Spectral density graphs which summarize EAM modulation.

By using a band pass filter centered around f_c , we eliminate the parasitic component (Figure 6.8 a). The last step is the demodulation of the two motional current with a balanced Gilbert cell (Figure 6.9).

The expression of the output voltage which is sent to the network analyzer can be deduced multiplying i_o by the demodulation signal:

$$r_{dm} = R_{dm} v_m \cos(\omega_c t + \varphi) \quad (6.18)$$

Where $R_{dm} = R_f K_{mult}$, with R_f feedback resistance di feedback of the' transresistive amplifier and K_{mul} , is the gain of the Gilbert cell

$$v_{EAM} = i_0 r_{dm} = V_{EAM} e^{\angle V_{EAM}} \quad (6.19)$$

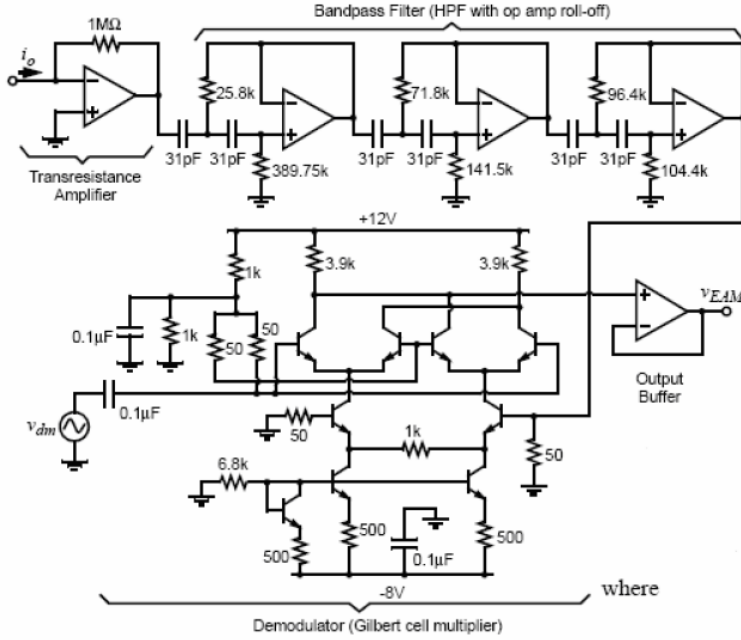


Figure 6.9: Schematic of the EAM box.

$$V_{EAM} = \frac{1}{2} C_m V_C R_{dm} v_{dm} \sqrt{\omega_0^2 \cos^2 \varphi + \omega_c^2 \sin^2 \varphi} \quad (6.20)$$

$$\angle V_{EAM} = \tan^{-1} \left(-\frac{\omega_c \sin \varphi}{\omega_0 \cos \varphi} \right) \quad (6.21)$$

The scheme of the output circuit (EAM Box) is in represented in Figure 6.9: the phase-shifter in Figure 6.7 aggiunge uno sfasamento in ritardo di 90° alla sinusoide di demodulazione per massimizzare l'uscita alla risonanza. Infatti nell'ipotesi che si abbia $\omega \gg \omega_r$, per la tensione di uscita si ottiene:

6.4.2 The second harmonic method

In this work the second harmonic method is used second. Our measurement method, already presented elsewhere [10], is based on the quadratic relationship between force and voltage. By calling *driving stator* the fixed electrode where a sinusoidal signal of amplitude V_s at frequency f is applied, *rotor* the (grounded) moving electrode of the actuator and *sensing stator* a second fixed electrode,

biased with a constant voltage E , it can be shown that the current flowing from this electrode contains a component at frequency $2f$ whose amplitude is proportional to the rotor deflection, and to the square of the input voltage amplitude. An advantage of this method is to eliminate the contribution of the parasitic current between the two stators (as this is at the frequency f of the driving signal) by using the voltage non-linearity implied in equation (6.2) to perform a frequency doubling of the useful signal. In questo lavoro si utilizza il metodo elettrico della seconda armonica. The scheme of the sensing and driving circuit using this method is represented in Figure 6.10.

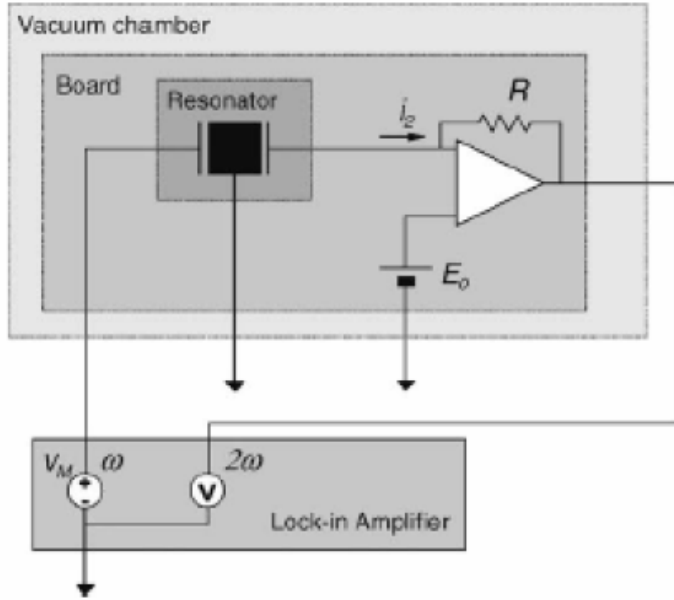


Figure 6.10: Second harmonic method circuit

An input voltage $v_D = v_i \cos(\omega t)$ is imposed between one of the two stator and the rotor while on the output stator there is a DC voltage V_0 . By assuming that the parasitic capacitance between input and output does not depend on the rotor position, the parasitic current is a sinusoidal signal at frequency ω . As seen before we consider the linear approximation of C_D e C_S :

$$\begin{aligned} C_D &= C_{D_0} + \left. \frac{\partial C_D}{\partial z} \right|_{z=0} z = C_{D_0} + c'_D z \\ C_S &= C_{S_0} + \left. \frac{\partial C_D}{\partial z} \right|_{z=0} z = C_{S_0} + c'_D z \end{aligned} \quad (6.22)$$

The total force acting on the movable is then deduced:-

$$f(t) = \frac{1}{2} \left(\frac{\partial (C_D v_D^2 + C_S v_S^2)}{\partial z} \right) = f_0 - f_1 \cos(2\omega t) \quad (6.23)$$

where:

$$f_0 = \frac{1}{2} \left(c'_s V_0^2 + c'_D \frac{v_i^2}{2} \right) \quad (6.24)$$

$$f_1 = \frac{1}{2} c'_D \frac{v_i^2}{2} \quad (6.25)$$

where f_0 and f_1 are the mean value of the force and the amplitude of the sinusoidal part respectively. The frequency of the signal which driver the structure is the double of the input voltage signal frequency. The position is then determined

$$z(t) = \frac{f_0}{k_{eq}} - |H(2\omega)| f_1 \cos[2\omega t + \angle(H(2\omega))] \quad (6.26)$$

where $H(\omega)$ is frequency response already seen.

$$H(\omega) = \frac{Z(\omega)}{F(\omega)} = \frac{k_{eq}^{-1}}{1 - \left(\frac{\omega}{\omega_r} \right)^2 + j \frac{\omega}{Q\omega_r}} \quad (6.27)$$

By substituting (6.27) in the expresion of the output current:

$$i_s = - \frac{\partial (C_S v_S)}{\partial t} = V_0 c'_s \frac{c'_D v_i^2}{2} \omega |H(2\omega)| \cos[2\omega t + \angle(jH(2\omega))] \quad (6.28)$$

This current is proportional to the velocità of the movable mass. The measured current are very low except for an input frequency equal to an half of the resonance frequency of the electromechanical system where the high quality factor of this kind of resonator produce current of measurable amplitude. The output signal in this condition is equal to:

$$V_{out} = R_c V_0 \frac{v_i^2}{2} \left(\left. \frac{\partial C_D}{\partial z} \right|_{z=0} \right) \left(\left. \frac{\partial C_S}{\partial z} \right|_{z=0} \right) 2\pi f_r \left(\frac{Q}{k_{eq}} \right) \quad (6.29)$$

where R_c is resistance of the transresistive amplifier..

By comparing this method with EAM, it allows the use of a very simple electronic circuit and a signal band lower.

On the other side its limits consist in the fact that the second order effect and nonlinearities reduce the range of applications. In fact for this technique it is necessari a wave generator which produce sinusoid without distorsion which can be confused with the measured signal.

6.5 Measurements

The torsional resonator is described by the following equation of motion:

$$I\ddot{\theta} + b\dot{\theta} + k_\theta\theta = M_{el} = M_{el_dc} + M_{el_ac} \quad (6.30)$$

where I is the moment of inertia of the structure with respect to the central axis of the springs, b is the damping factor, k_θ is twice the torsional spring constant of each serpentine spring (see Fig. 2, bottom) and M_{el} is the electrostatic torque due to the voltage applied to drive and measure the resonator (M_{el_dc} and M_{el_ac} are the torques due to the constant and the sinusoidal respectively). Our measurement method, already presented elsewhere [92], is based on the quadratic relationship between force and voltage. By calling *driving stator* the fixed electrode where a sinusoidal signal of amplitude V_s at frequency f is applied, *rotor* the (grounded) moving electrode of the actuator and *sensing stator* a second fixed electrode, biased with a constant voltage E , it can be shown that the current flowing from this electrode contains a component at frequency $2f$ whose amplitude is proportional to the rotor deflection, and to the square of the input voltage amplitude. As already seen, an advantage of this method is to eliminate the contribution of the parasitic current between the two stators (as this is at the frequency f of the driving signal) by using the voltage non-linearity implied in equation (6.2) to perform a frequency doubling of the useful signal. Interestingly, a similar advantage could be obtained by exploiting parametric resonance of the device, as suggested in [93].

After several algebraic passages and by passing in the frequency domain, the mechanical response $H(f)$ of the resonator is deduced:

$$H(f) = \frac{\theta(f)}{M_{el_ac}(f)} = \frac{k_{eff}^{-1}}{1 - \left(\frac{f}{f_r}\right)^2 + j\frac{f}{f_r Q}} \quad (6.31)$$

were the following parameters are used:

- the effective torsional elastic constant, which includes the effect of electrostatic stiffening [2]:

$$k_{eff} = k_\theta + mE^2, \text{ with } m = \frac{\alpha N_{cf}}{3} (l_6^3 - l_5^3) \quad (6.32);$$

- the resonance frequency:

$$f_r = \frac{1}{2\pi} \sqrt{\frac{k_\theta + mE^2}{I}} \quad (6.33);$$

- the quality factor:

$$Q = \frac{\sqrt{k_{eff} I}}{b} \quad (6.34);$$

- the number N_{cf} of fingers of the sensing electrode (half of the number of the driving electrode).

The applied torque in the frequency domain, $M_{el_ac}(f)$, caused by the aforementioned driving configuration, equals

$\frac{2\alpha z_0 N_{cf}}{4} (l_4^2 + l_2^2 - l_1^2 - l_3^2) |V_s(f)|^2$, as can be deduced by applying equation (6.4) to the specific geometry shown in Figure 6.2 (left).

We measure the current in the sensing electrode by using a three-stage transresistive amplifier. The following relation for the output voltage can be found [92]:

$$V_{out} = R_c E \left(\frac{dC_{driv}}{d\theta} \bigg|_{\theta=0} \right) \left(\frac{dC_{sens}}{d\theta} \bigg|_{\theta=0} \right) \frac{V_s^2}{2} 2\pi f |H(4\pi f)| \sin[4\pi f t + \arg(H(4\pi f))] \quad (6.35)$$

where C_{driv} and C_{sens} are the total capacitance of the sensing and the driving electrodes, respectively and R_c is the total transresistance of the amplifier. We note that the output is proportional to the voltage E applied to the sensing stator, as well as to the square of the input voltage V_s .

With this method, several frequency response curves were extracted at different vacuum levels and applied voltages on the sensing electrode. As an example, two such curves are shown in Figure 6.11. Also,

because of the electrostatic stiffening effect, a shift in the resonance frequency is expected. In Figure 6.12 the measured resonance frequency f_r is plotted against the applied voltage E , along with a fitting curve of the form (6.33). From this fitting, the resonance frequency with $E = 0$ V (which cannot be measured directly) can be deduced:

$$f_0 = f_r|_{E=0} = \frac{1}{2\pi} \sqrt{\frac{k_\theta}{I}} \quad (6.36)$$

The obtained resonance frequency $f_0 = 5910$ Hz is in reasonable agreement with a lumped parameters analytical model of the mechanical structure, based on the spring formulas given in [85], which predicted $f_0 = 5686$ Hz. From the same fitting, and by exploiting equation (7), a value for α can be deduced as well. The error between the obtained value ($\alpha = 1.012 \text{ Fm}^{-3}$) and the simulated value ($\alpha = 1.1 \text{ Fm}^{-3}$) is less than 10%.

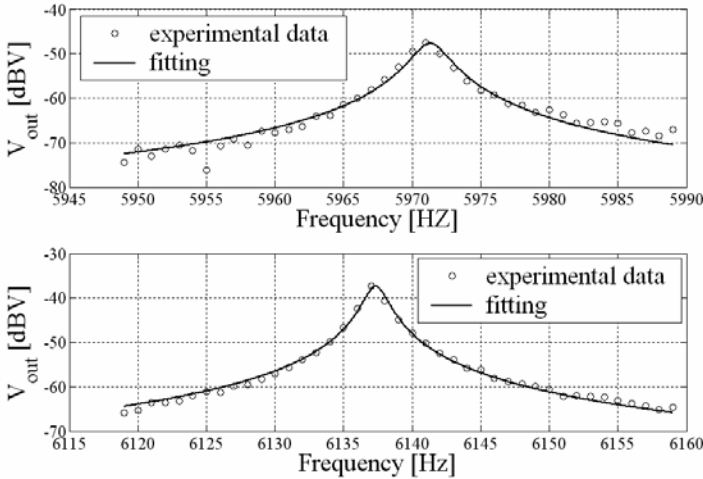


Figure 6.11: Amplitude of the voltage output V_{out} with two different values of the sensing stator DC voltage E and of the pressure P : a) $P = 30$ Pa, $E = 2$ V, resonance frequency $f_r = 5971$ Hz, quality factor $Q = 2338$; b) $P = 20$ Pa, $E = 4$ V, resonance frequency $f_r = 6137$ Hz, quality factor $Q = 3784$.

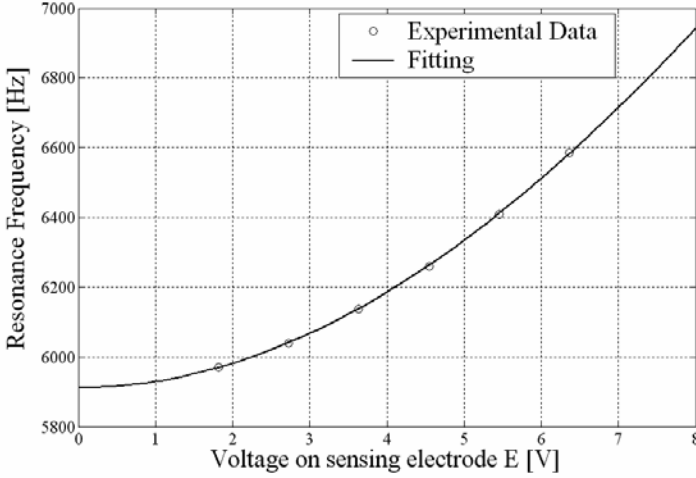


Figure 6.12:Dependence of the resonance frequency on applied voltage E on sensing electrode

6.6 FEM simulations

The good agreement between measurements and theoretical analysis have induced the authors to investigate the dependence of the actuator performance on the design parameters. Hence, the aforementioned electrostatic simulations used to compute the capacitance $c_s(z)$ in the range $z \in [0 \mu\text{m}, 2 \mu\text{m}]$ were extended by changing other relevant geometrical parameters (defined in Fig. 3): the distance between the movable finger and the stationary electrode (d_{fg}), the distance between the finger and the ground plane (h), the width (w) and the thickness (t) of the fingers. All the obtained results were fitted with the expression (6.3), showing an excellent agreement between $c_s(z)$ and a parabolic profile.

In Fig. 8, the derivative of the capacitance dc_s/dz (which, recalling equation (6.1), is proportional to the actuation force) at different d_{fg} is shown. We notice that, increasing the gap between the movable finger and the stationary electrode, the value of z_0 increases, thus implying a larger travel range for the actuator. At the same time, α decreases with d_{fg} . This is more clearly shown by Fig. 9 and Fig. 10, where z_0 and α are given as a function of d_{fg} . This means that an increase in d_{fg} gives a larger travel range as long as a reduction of the driving force (proportional to α) is accepted.

The gap between the suspended structures and the ground plate h is a relevant design parameter as well. because z_0 decreases with h while α is weakly dependent on it (Fig. 9 and 10). Hence, by decreasing h it would be possible to increase the travel range without significant reduction of the force. The practical importance of this parameter is, however, less relevant than that of d_{fg} , because the sacrificial layer thickness is infrequently a variable that can be freely changed by the designer. However, this information is significant when a specific technology has to be tailored to enhance (or, in the case of lateral devices, to limit) the effect of levitational forces.

In all our simulations and analyses the potential upward (or downward) bending of movable fingers caused by released stress gradients in the structural layer was considered to be zero. This is justified by the fact that typical stress values for similar technologies (see, for an example [12]) are in the range of 1 MPa/ μm or less. Such stresses, once released, would result in a deflection of the finger tip around 40 nm for a finger length of 100 μm , and thus can be safely neglected.

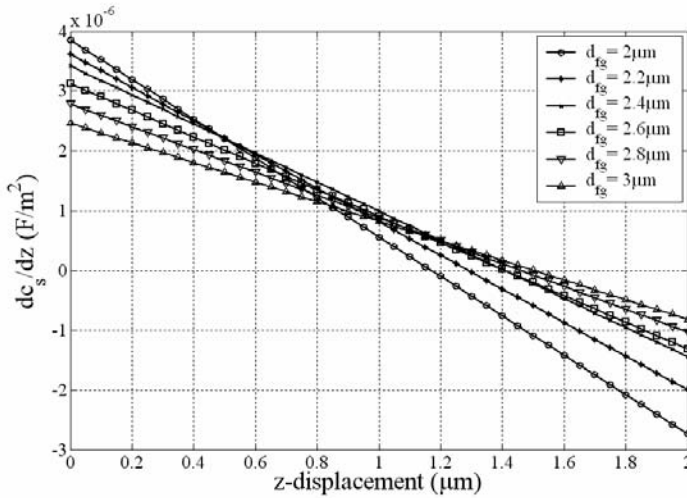


Figure 6.13: Graphs of dc_s/dz for different values of the distance between the stationary and the movable fingers.

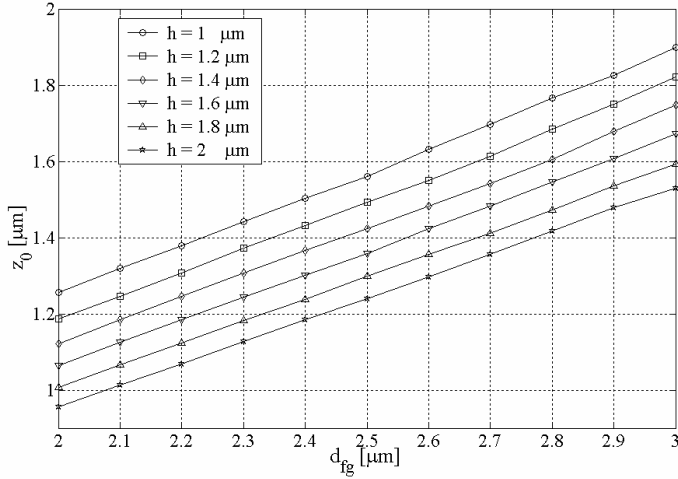


Figure 6.14: Graphs of z_0 as a function of the distance between the stationary and the movable fingers (d_{fg}) for different values of the distance between the movable fingers and the ground plane (h)

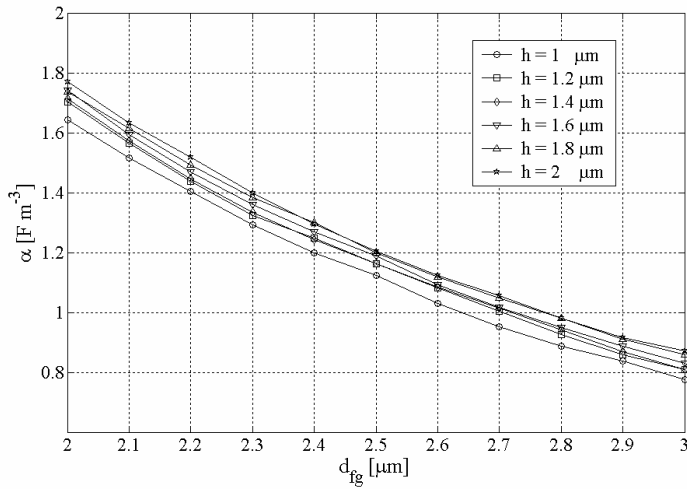


Figure 6.15: Graphs of α as a function of the distance between the stationary and the movable fingers (d_{fg}) for different values of the distance between the movable fingers and the ground plane (h) .

Chapter 7

Conclusions

In this thesis we presented analysis, designed and measurements of different electrostatic actuators.

We have demonstrated the feasibility of a micromirrors based optical switch using a commercial surface micromachining process (THELMA by *STMicroelectronics*). This device is constituted by polysilicon micromirrors arrays which are moved using torsional electrostatic actuators. An in depth study of this actuator has been carried out and a new method for the fast prediction of the static characteristic of an electrostatically actuated torsional micromirror, taking into account the bending caused by the electrostatic force, was presented. The method was validated against FEM simulations and experimental measurements, which showed a very good agreement with the model.

The possibility of using another competitive surface micromachining technology (developed at IMEC) which uses poly silicon germanium as structural layer to realize the micromirrors has been investigated. Poly-SiGe has been promoted as a material suitable as structural layer for MEMS applications on the top of CMOS. This can be attributed to the fact that good electrical and mechanical properties can be obtained at much lower temperatures (down to 400°C) as compared to poly-silicon (above 800°C). The development of optimized (low stressed) layer of poly silicon germanium has been addressed and some test micromirrors using this technology have been designed.

This thesis has also demonstrated the feasibility and outlined some of the design issues for the electrostatic levitation comb drive. Mechanical resonators which use this actuation have been designed, realized and measured. The obtained results were in agreement with predictions and FEM simulations.

The elastic elements of the presented resonators are particular serpentine spring. In this thesis we showed an analytical approach to evaluate the spring constants of serpentine springs, useful in

microstructures design. Two kind of serpentine springs were analyzed: one with classic shape and another with rotated serpentine shape. FEM simulations were used to check the analytical formulas and it was shown that the results are in accordance with the theory in the range of validity of the beam approximation. It was found that the analytical formulas are useful to compare the performances of the two kinds of springs. It was also verified that the rotated serpentine springs are more suitable for torsional applications, especially for high thickness of the structural layer.

Hence a set of FEM electrostatic simulations was carried out to verify the dependence of force intensity on the geometrical parameters of the actuators. An important information obtained is that the maximum height which can be reached using levitational actuators can be increased by increasing the distance between the movable and the static fingers. In this thesis mechanical resonators have been presented but the information obtained from FEM simulations should allow the design of MEMS using electrostatic levitation with wide applications.

Bibliography

- [1] Fujita, H., 1996, 'Future of actuators and microsystems', *Sensors and Actuators A: Physical* 56:105–111.
- [2] Fujita, H., 1998, 'Microactuators and micromachines', *Proceedings of the IEEE* 86(8): 1721–1732.
- [3] Bustillo, J.M., Howe, R.T., Muller, R.S., 1998, 'Surface micromachining for microelectromechanical systems', *Proceedings of the IEEE* 86(8): 1552–1574.
- [4] Kovacs, G.T.A., Maluf, N.I., Petersen, K.E., 1998, 'Bulk micromachining of silicon', *Proceedings of the IEEE* 86(8): 1536–1551.
- [5] Guckel, H., 1998, 'High-aspect-ratio micromachining via deep X-ray lithography', *Proceedings of the IEEE* 86(8): 1586–1593.
- [6] Ikuta, K., Hirowatari, K., 1993, 'Real three dimensional microfabrication using stereo lithography and metal molding', in *Proceedings of IEEE MEMS '93*, IEEE, Washington, DC: 42–47.
- [7] Takagi, T., Nakajima, N., 1993, 'Photoforming applied to fine machining', in *Proceedings of IEEE MEMS '93*, IEEE, Washington, DC: 173–178.
- [8] Taylor, C.S., Cherkas, P., Hampton, H., Frantzen, J.J., Shah, B.O., Tiffany, W.B., Nanis, L., Booker, P., Salahieh, A., Hansen, R., 1994, 'A spatial forming – a three dimensional printing process', in *Proceedings of IEEE MEMS '94*, IEEE, Washington, DC: 203–208.
- [9] Thornell, G., Johansson, S., 1998, 'Microprocessing at the fingertips', *Journal of Micromechanics and Microengineering* 8: 251–262.
- [10] Varadan, V.K., Varadan, V.V., 1997, 'Microsensors, actuators, MEMS, and electronics for smart structures', in Rai-Choudhury, P. (ed.), *Handbook of Microlithography, Micromachining, and Microfabrication, Volume 2: Micromachining and Microfabrication*, SPIE Optical Engineering Press: 617–688.
- [11] Xia, Y., Whitesides, G.M., 1998, 'Soft lithography', *Angew. Chem. International Ed.* 37: 550–575.

- [12] Bryzek, Peterson, K., McCulley, W., 1994, 'Micromachines on the march', IEEE Spectrum (May) 20–31.
- [13] Fan, L.-S., Tai, Y.-C., Muller, R.S., 1987, 'Pin joints, gears, springs, cranks and other novel micromechanical structures', in Tech Digest of 4th International Conference Solid State Sensors and Actuators A: Physical, June, Tokyo: 849–852.
- [14] Middelhoek, S., Audet, S.A., 1989, Silicon Sensors, Academic Press, London.
- [15] Petersen, K.E., 1982, 'Silicon as a mechanical material', Proceedings of IEEE 70: 420–457.
- [16] Varadan, V.K., Jiang, X., Varadan, V.V., 2001, Microstereolithography and other fabrication techniques for 3D MEMS, John Wiley, Chichester.
- [17] Aeidel, H., 1994, 'The mechanism of anisotropic silicon etching process for microelectromechanical structures', Sensors and Actuators, A, 40, pp. 63–70.
- [18] Shaw, K.W., Zhang, Z.L., MacDonald, N.C., 1994, 'SCREAM: a single mask, single-crystal silicon, reactive ion etching process for microelectromechanical structures', Sensors and Actuators A: Physical 40: 63–70.
- [19] Madou, M., 1997, Fundamentals of Microfabrication, CRC Press, Boca Raton, FL.
- [20] A.Witvrouw, M. Gromova, A.Mehta, S. Sedky, P. De Moor, K. Baert, C. Van Hoof, Poly-SiGe, a superb material for MEMS, Proceedings of the MRS Fall Meeting, Boston, MA, USA, 1–5 December 2003.
- [21] Stix, G., 1992, 'Trends in micromechanics: micron machinations', Scientific American, (November): 12–80.
- [22] Larson, L.E., 1999, 'Microwave MEMS technology for next-generation wireless communications –invited paper', in IEEE MTT-S International Symposium Digest, IEEE, Washington, DC: 1073–1076.
- [23] J. Mohr et al., 1991, 'Herstellung von beweglichen mikrostrukturen mit dem LIGA-verfahren', KfK-Nachrichten, Jahrgang 23, Forschungszentrum Karlsruhe 2–3: 110–117.
- [24] Bertsch, A., Lorenz, H., Renaud, P., 1998, 'Combining microstereolithography and thick resist UV lithography for 3D microfabrication', in Proceedings of IEEE MEMS '98 , IEEE, Washington, DC: 18–23.

- [25] Takagi, T., Nakajima, N., 1994, 'Architecture combination by micro photoforming process', in *Proceedings of IEEE MEMS '94*, IEEE, Washington, DC: 211–216.
- [26] Johnson, R.A., 1983, *Mechanical Filters in Electronics*, Wiley Interscience, New York.
- [27] Tilmans, H.A.C., 1996, 'Equivalent circuit representation of electromechanical transducers: I. Lumped parameter systems', *Journal of Micromechanics and Microengineering* 6: 157–176.
- [28] W.C. Tang, T.C.H. Nguyen and R.T. Howe, 1989, 'Laterally driven polysilicon resonant microstructures', *Sensors and Actuators* 20: 25–32.
- [29] Hom, C.L., Pilgrim, S.M., Shankar, N., Bridger, K., Massuda, M., Winzer, S.R., 1994, 'Calculation of quasi-static electromechanical coupling coefficients for electrostrictive ceramic materials', *IEEE Transactions on Ultrasonics, Ferroelectrics, and Frequency control* 41: 542–551.
- [30] Huang, Q.A., Lee, N.K.S., 1999, 'Analysis and design of polysilicon thermal flexure actuator', *Journal of Micromechanics and Microengineering* 9: 64–70.
- [31] Fatikow, S., Rembold, U., 1997, *Microsystem technology and microrobots*, Springer, Berlin. Frank, T., 1998, 'Two-axis electrodynamic micropositioning devices', *Journal of Micromechanics and Microengineering* 8: 114–118.
- [32] Rai-Choudhury, P., 1997, *Handbook of Microlithography, Micromachining and Microfabrication*, Vol. 2: *Micromachining and Microfabrication*, SPIE Optical Engineering Press.
- [33] Harada, K., Ikeda, K., Kuwayama, H., Murayama, H., 1999, 'Various applications of resonant pressure sensor chip based on 3-D micromachining', *Sensors and Actuators A: Physical* 73: 261–266.
- [34] Campbell, C., 1998, *Surface Acoustic Wave Devices and their Signal Processing Applications*, Academic Press, London.
- [35] V. P. Jaecklin, C. Lindner, J. Brugger, J.-M. Moret, R. Vuilleumier, and N. F. de Rooij. Mechanical and optical properties of surface micromachined torsional mirrors in silicon, polysilicon, and aluminum. In *Proc. Transducers*, Yokohama, Japan 1993, pages pp.958–1, 1993.
- [36] P. F. Van Kessel, L. J. Hornbeck, R. E. Meier, and M. R. Douglass. A mems-based projection display. In *Proc. IEEE*, volume 86, pages pp.1687–1704, 1998.

- [37] U. Dauderstädt, P. Dürr, and W. Doleschal. A spatial light modulator (slm) for advanced lithography, 1000.
- [38] G.-D. J. Su, H. Toshiyoshi, and M. C. Wu. Surface micromachined 2-d optical scanners with high performance single crystalline silicon micromirrors. *IEEE Photon. Technol. Lett.*, 13:pp. 606–608, 2001.
- [39] A. Tuantranont, V. M. Bright, L.-A. Liew, W. Zhang, and Y. C. Lee. Smart phase-only micromirror array fabricated by standard cmos process. In *Proc. MEMS*, pages pp.455–60, 2000.
- [40] J.E. Ford, V.A. Aksyuk, and D.J. Bishop and J.A. Walker. Wavelength adddrop switching using tilting micromirrors. *J. of Lightwave Tech.*, 5, 1999.
- [41] V. A. Aksyuk, F. Pardo, and D. J. Bishop. Stress-induced curvature engineering in surface-micromachined devices. In *Proc. SPIE*, volume 3680, pages pp.984–989, 1999.
- [42] H. Martinsson, T. Sandstrom, A.Bleeker and J. D. Hintersteiner Current status of optical maskless lithography, *Journal of Microlithography, Microfabrication, and Microsystems* January - March 2005, Volume 4, Issue 1
- [43] C. R. Giles, D. Bishop, and V. Aksyuk, “MEMS for light-wave networks,” *MRS Bull.*, Special Issue on Microelectromechanical Systems: Technology and Applications, vol. 26, no. 4, pp. 328–329, Apr. 2001.
- [44] D. J. Bishop, C. R. Giles, and S. R. Das, “The Rise of Optical Switching,” *Sci. Amer.*, pp. 88–94, Jan. 2001.
- [45] A. Neukermans, “MEMS devices for all optical networks,” in *Proc. SPIE*, vol. 4561, *MOEMS and Miniaturized Systems II*, 2001, pp. 1–10.
- [46] L. Lin, E. Goldstein, and R. Tkach, “Free; space micromachined optical switches with submillisecond switching time for large-scale optical crossconnects,” *IEEE Photon. Technol. Lett.*, vol. 10, pp. 525–527, Apr. 1998.
- [47] P. Hagelin, U. Krishnamoorthy, J. Heritage, and O. Solgaard, “Scalable optical cross-connect switch using micromachined mirrors,” *IEEE Photon. Technol. Lett.*, vol. 12, pp. 882–884, July 2000.
- [48] M. R. Dokmeci, A. Pareek, S. Bakshi, M. Waelti, C. D. Fung, K. H. Heng, and C. H. Mastrangelo, Two-Axis Single-Crystal Silicon Micromirror Arrays *Journal Of Microelectromechanical Systems*, Vol. 13, No. 6, December 2004, 1006-1017

- [49] A. Molfese, A. Mehta and A. Witvrouw ,“Determination of stress profile and optimization of stress gradient in PECVD poly-SiGe films”, , Sensors and Actuators A: Physical, Volume 118, Issue 2, 28 February 2005, Pages 313-321
- [50] D. Galayko, A. Kaiser, L. Buchailot, B. Legrand, D. Collard, and C. Combi; “Design, realization and testing of micro-mechanical resonators in thick-film silicon technology with postprocess electrode-to-resonator gap reduction”, J. Micromech. Microeng., 13, pp. 134–140, 2003.
- [51] T.J. King, R.T. Howe, S. Sedky, G. Liu, B.C.Y. Lin, M. Wasilik, C. Duenn, Recent progress in modularly integrated MEMS technologies, IEDM Proceedings’02, San Francisco, CA, USA, 8–12 December 2002, pp. 199–202.
- [52] A. Francke, J. Heck, T.J. King, R.T. Howe, Polycrystalline silicon germanium films for integrated microsystems, J. Microelectromech. Syst. 12 (2) (2003) 160–171.
- [53] A. Mehta, M. Gromova, C. Rusu, K. Baert, C. Van Hoof, A.Witvrouw, Novel high growth rate processes for depositing poly-SiGe structural layers at CMOS compatible temperatures, Proceedings of the MEMS, Maastricht, Netherlands, 15–29 January 2004, pp. 721–724.
- [54] M. Gromova, K. Baert, C. Van Hoof, A. Mehta, A. Witvrouw, The novel use of low temperature hydrogenated microcrystalline silicon germanium ($\mu\text{cSiGe:H}$) for MEMS Applications, accepted for publication in Proc. MAM 2004 (to be published in special issue of Microelectronic Engineering).
- [55] S. Sedky, A. Witvrouw, K. Baert, Poly SiGe, a promising material for MEMS monolithic integration with the driving electronics, Sens. Actuators A 97–98 (2002) 503–511.
- [56] S. Sedky, A. Witvrouw, M. Caymax, A. Saerens, P. Van Houtte, Characterization of reduced-pressure chemical vapour deposition polycrystalline silicon germanium deposited at temperature $\leq 550^\circ\text{C}$, J. Mater. Res. 17 (7) (2002) 1580–1586.
- [57] C. Rusu, S. Sedky, B. Parmentier, A. Verbist, O. Richard, B. Brijs, L. Geenen, A. Witvrouw, F. Larmer, F. Fischer, S. Kronmuller, V. Leca, B. Otter, New low stress PECVD poly-SiGe layers for MEMS, J. Microelectromech. Syst. 12 (6) (2003) 815–825.
- [58] P. Krulevitch, R.T. Howe, G.C. Johnson, J. Huang, Stress in undoped LPCVD Polycrystalline Silicon, Proceedings of the Transducers’91, San Francisco, CA, USA, 1991, pp. 949–952.

- [59] E.H. Yang, S.S. Yang, The quantitative determination of the residual stress profile in oxidized p+ films, *Sens. Actuators A* 54 (1996) 684–689.
- [60] T. van der Donck, J. Proost, C. Rusu, K. Baert, C. Van Hoof, J.-P. Celis, A. Witvrouw, Effect of deposition parameters on the stress gradient of CVD and PECVD poly-SiGe for MEMS applications, *Proceedings of the SPIE Conference 5342*, San Jose, CA, USA, January 28–29, 2004, pp. 8–18.
- [61] M.W. Furtusch, Mechanical properties of thick polycrystalline silicon films suitable for surface micromachining, Ph.D. thesis, Gerhard- Mercator-Universität, Gesamthochschule Duisburg, 1998.
- [62] M. Gere, S.P. Timoshenko, *Mechanics of Materials*, fourth ed., PWS Publishing Company, Boston, 1997, pp. 310–315, 509–607.
- [63] E. Kasper, *Properties of Strained and Relaxed Silicon Germanium*, INSPEC, London, 1995.
- [64] A. Witvrouw, B. Du Bois, P. De Moor, A. Verbist, C. Van Hoof, H. Bender, K. Baert, A comparison between wet HF etching and vapour HF etching for sacrificial oxide removal, *SPIE Proc.* 4174 (2000) 130–141.
- [65] Hao Z, Wingfield B, Whitley M, Brooks J and Hammer J A 2003 A design methodology for a bulkmicromachined two-dimensional electrostatic micromirror *J of Microelectromechanical Systems* vol. 12 no. 5 october 2003 p 692-701
- [66] H. Toshiyoshi, and H. Fujitsa; “Electrostatic micro torsion mirrors for an optical switch matrix”, *J. Microelectromech. Syst.*, vol. 5 iss. 4 , pp. 231–237, 1996.
- [67] V.A. Aksyuk, F. Pardo, D. Carr, D. Greywall et al; “Beam-steering micromirrors for large optical cross-connects”, *J. Lightwave Technol.*, vol. 21 iss. 3, pp 634–642, 2003
- [68] V.A. Aksyuk, M.E. Simon, F. Pardo, and S. Arney, “Optical MEMS design for telecommunications applications”, *Solid-state sensor, actuator and Microsystems workshop*, Hilton Head Island, South Carolina, June 2002, pp.1-6
- [69] X.M. Zhang, F.S. Chau, C. Quan, Y.L. Lama, and A.Q. Liu, “A study of the static characteristics of a torsional micromirror, *Sensors and Actuators A*, vol. 90, pp. 73-81, 2001.
- [70] J.-M. Huang, A.Q. Liu, Z.L. Deng, Q.X. Zhang, J. Ahn; and A. Asundi; “An approach to the coupling effect between torsion

- and bending for electrostatic torsional micromirrors”, *Sensors and Actuators A*, vol. 115, pp. 159–167, 2004.
- [71] O. Degani, E. Socher, A. Lipson, T. Leitner, D. J. Setter; S. Kaldor, and Y. Nemirovsky, “Pull-in study of an electrostatic torsion microactuator”, *J. Microelectromech. Syst.*, vol. 7 iss. 4, pp. 373-379, 1998.
 - [72] A. Molfese, A. Nannini and F. Pieri, “Reduced-Order Modelling of the Bending of an Array of Torsional Micromirrors”, , accepted for the publication on *Analog Integrated Circuits & Signal Processing*
 - [73] S. P. Timoshenko, and J. N Goodier, *Theory of Elasticity*, Third Edition, McGraw Hill Company, 1970.
 - [74] S. Merlo, V. Annovazzi-Lodi, M. Benedetti, F. Carli, and M. Norgia, Testing of “Venetian-Blind” Silicon Microstructures With Optical Methods, *Journal Of Microelectromechanical Systems*, Vol. 15, No. 3, June 2006, pp 588-596
 - [75] M. Perolio, *Microspecchi A Veneziana Con Doppio Elettrodo Di Attuazione*, Tesi Di Laurea Università degli Studi di Pavia, 2006
 - [76] Fedder G 1994 *Simulations of Microelectromechanical Systems* PhD thesis UC Berkeley p 85-86
 - [77] Tang W C 1990 *Electrostatic comb drive for resonant sensor and actuator applications* PhD thesis, Dept of Electrical Engineering and Computer Science, University of California at Berkeley
 - [78] Brennen R, Pisano A and Tang 1990 *Multiple Mode Micromechanical Resonators* Proc. IEEE Micro Electro Mechanical Systems Workshop
 - [79] Aksyuk V A, Simon M E, Pardo F, Arney S, Lopez D and Villanueva A 2002 *Optical MEMS Design for Telecommunications Applications* Solid-State Sensor, Actuator and Microsystems Workshop Hilton Head Island, South Carolina, June 2-6, 2002
 - [80] G. Barillaro, A. Molfese, F. Pieri and A. Nannini, “Analysis, simulation and relative performances of two kinds of serpentine springs”, *Journal of Micromechanics and Microengineering*, vol. 15, pp 736–746, 2005.
 - [81] Xiao Z, Peng W and Farmer K R 2003 *Analytical behavior of rectangular electrostatic torsion actuators with nonlinear spring*

- bending J. of Microelectromechanical Systems vol 12 no. 6 p. 929/ 936X
- [82] Iyer S, Zhou Y and Mukherjee T 1999 Technical Proceedings of the 1999 International Conference on Modeling and Simulation of Microsystems Analytical Modeling of Cross-axis Coupling in Micromechanical Springs p 632-635
 - [83] W. C. Tang, T.-C. H. Nguyen, M. W. Judy, and R. T. Howe, "Electrostatic-comb drive of lateral polysilicon resonators," Sensors and Actuators A, vol. 21–23, pp. 328–331, 1990.
 - [84] W.C. Tang, M.G. Lim and R.T. Howe, "Electrostatic comb drive levitation and control method", Journal of Microelectromechanical Systems, vol. 4, pp. 170-178, 1992.
 - [85] C. Painter and A. Shkel, "Effect of levitation Forces on the Performance of Surface Micromachined MEMS Gyroscopes", Proceedings of Sensors 2004, IEEE, Vienna, Austria, 2004, pp.508-511.
 - [86] C. Painter and A. M. Shkel, "Structural and thermal modeling of a z-axis rate integrating gyroscope", J. of Micromechanics and Microengineering, vol. 13, pp. 229-237, 2003.
 - [87] A.P. Lee, C.F. McConaghy and P.Krulevitch, "Vertical-Actuated Electrostatic Comb Drive With In Situ Capacitive Position Correction for Application in Phase Shifting Diffraction Interferometry", Journal of Microelectromechanical Systems, vol. 12, pp. 960-971, 2003.
 - [88] K.L. Turner and W. Zhang, "Design and analysis of a dynamic MEM chemical sensor", in Proceedings of the 2001 American Control Conference, Arlington, VA, USA, 25-27 June 2001, pp. 1214-1218.
 - [89] A. Molfese, A. Nannini, G. Pennelli and F. Pieri "Analysis, Testing and Optimization of Electrostatic Comb-Drive Levitational Actuators", , Analog Integrated Circuits & Signal Processing, 2006, Vol. 48, pp. 33-40
 - [90] P. Bruschi, A. Nannini, F. Pieri, G. Raffa, B. Vigna and S. Zerbini, "Electrostatic analysis of a comb-finger actuator with Schwarz–Christoffel conformal mapping", Sensors and Actuators A: Physical, Volume 113, Issue 1, pp 106-117, 2004.
 - [91] J.-L. Andrew Yeh, Chung-Yuen Hui, and Norman C. Tien, "Electrostatic Model for an Asymmetric Combdribe", Journal of Microelectromechanical Systems, vol. 9, n. 1, pp. 126-135, 2000.

- [92] P. Bruschi, A. Nannini and F. Pieri, “Electrical measurements of the quality factor of microresonators and its dependence on the pressure”, *Sensors and Actuators A*, vol. 114, 1, pp 21-29, 2004.
- [93] K. L. Turner, S. A. Miller, P. G. Hartwell, N. C. MacDonald, S. H. Strogatz, S. G. Adams, “Five parametric resonances in a microelectromechanical system”, *Nature*, vol. 396, pp. 149-152, 1998.